Quantum walks and relativistic quantum simulations with trapped ions

Thesis submitted to the
Faculty of Mathematics, Computer Science and Physics
of the Leopold-Franzens University of Innsbruck
in partial fulfillment
of the requirements of the degree of

Doctor rerum naturalium

by

Florian Zähringer

Innsbruck, June 2012

Abstract

In the last 15 years, quantum information processing has developed into a major field of research in physics. During this period various quantum systems were investigated as possible systems for quantum computation or quantum simulation and experimental control over these systems advanced significantly. Among them, trapped ions are very promising candidates for the realization of quantum algorithms, and a vast pool of experimental techniques has already been demonstrated with this type of quantum system.

This thesis reports on the implementation of such tools in three applications: precision spectroscopy, the demonstration of a quantum walk and the quantum simulation of the Klein paradox.

A new spectroscopic method of repetitive laser pulses is employed to measure the branching ratio of the $4s^2P_{3/2}$ level of $^{40}Ca^+$ with high precision. The branching fractions into the $4s^2S_{1/2}$, $3d^2D_{5/2}$ and $3d^2D_{3/2}$ levels are found to be 0.9347(3), 0.0587(2) and 0.00661(4), respectively. For the branching ratio $A(P_{3/2}-S_{1/2})/\sum_J A(P_{3/2}-D_J) = 14.31(5)$, a precision of better than 1% is achieved. The method is also applicable to other ion species that share a similar level structure.

A quantum walk on a line in phase space is experimentally demonstrated. The walk is performed to up to 23 steps, where each step subjects an ion to a state-dependent displacement operation interleaved with quantum coin-tossing operations. The ion's motional state is analyzed after each step with a technique that maps the probability distribution onto the internal state of the ion. The measured properties of the final state after the quantum walk clearly show a difference from the classical random walk. In addition, both the reversibility of the quantum walk and an extension with two ions are demonstrated.

The same measurement procedure is used in a quantum simulation of the Klein paradox. The position and momentum of a relativistic Dirac particle are mapped to the respective quadratures of the harmonic oscillator of the trap. While the spinor of the Dirac particle is mapped to one ion, a second ion is used to realize a linear and a quadratic potential. For both potentials, the reconstruction of the wave function in phase space is used to visualize the tunneling of the particle into regions that are classically forbidden.

In addition to these experiments, a new trap setup is presented. With a slightly modified trap design and improved vacuum conditions this new setup offers new experimental options.

Zusammenfassung

Die Quanteninformationsverarbeitung hat sich in den letzten 15 Jahren zu einem großen und aktiven Forschungsgebiet innerhalb der Physik entwickelt. Auf der Suche nach geeigneten Quantensystemen für eine Implementierung in einem Quantencomputer oder Quantensimulator werden verschiedenste Systeme erforscht. Gespeicherte Ionen gehören hier zu den vielversprechenden Kandidaten und inzwischen existiert eine Fülle an experimentellen Techniken, die eine hohe Kontrolle über diese Systeme erlaubt.

In dieser Arbeit werden einige dieser Techniken in einer Spektroskopiemessung, für die Implementierung einer diskreten Quantenbewegung und in einer Quantensimulation des Klein-Paradoxons zur Anwendung gebracht.

Mittels wiederholter Laserpulse wird das Zerfallsverhältnis des $4s^2P_{3/2}$ Energieniveaus von $^{40}Ca^+$ gemessen. Die Zerfallsanteile in die Energieniveaus $4s^2S_{1/2}$, $3d^2D_{5/2}$ und $3d^2D_{3/2}$ wurden mit 0,9347(3), 0,0587(2), respektive 0,00661(4) bestimmt. Diese Messmethode erreicht für das Zerfallsverhältnis $A(P_{3/2}-S_{1/2})/\sum_J A(P_{3/2}-D_J) = 14.31(5)$ eine Präzision von unter 1% und kann bei anderen Ionenarten mit ähnlichem Energieschema Anwendung finden.

Eine eindimensionale, diskrete Quantenbewegung im Phasenraum wird experiementell demonstriert. Bis zu 23 Schritte werden ausgeführt, wobei bei jedem Schritt ein zustandsabhängiger Verschiebungsoperator und ein Quantenmünzwurfoperator auf das Ion angewendet werden. Der Bewegungszustand des Ions wird anschließend mit einer Messmethode analysiert, bei der die Aufenthaltswahrscheinlichkeit auf den elektronischen Zustand des Ions abgebildet wird. Verschiedene Messungen zeigen deutliche Unterschiede zur klassischen Zufallsbewegung. Des weiteren wird die Quantenbewegung auf zwei Ionen erweitert.

Dieselbe Abbildungsmethode wird in einer Quantensimulation des Klein-Paradoxons verwendet. Für diese Simulation werden Impuls und Ort des relativistischen Dirac-Teilchens auf den Phasenraum des harmonischen Oszillators der Ionenfalle abgebildet und der Spinor wird im elektronischen Zustand eines Ions kodiert. Ein weiteres Ion wird verwendet, um ein lineares und ein quadratisches Potential zu realisieren. In beiden Fällen zeigt die rekonstruierte Wellenfunktion, wie das Teilchen in klassisch verbotene Regionen tunnelt.

Zusätzlich zu den beschriebenen Experimenten wird ein neuer Fallenaufbau vorgestellt. Durch Modifikation der Falle und Verbesserungen der Vakuumqualität eröffnet dieser Aufbau neue experimentelle Optionen.

Contents

1 Introduction

The idea of quantum simulation was introduced by Richard Feynman [1] and others in the early 80's of the previous century. The aim is to use a quantum system that is controllable in the laboratory to simulate the model of a system that, e.g., can not be controlled to the extent needed or not measured due to technical limitations.

Very significant for this approach is the potential to simulate quantum mechanical systems that are intractable for classical computers. The limitations to perform simulations of quantum systems with classical computers are caused by the exponential growth of computational space needed to store the parameters and the differential equations that describe such systems. Hence, these limitations can not be overcome easily by simple technological improvements.

To realise such a quantum simulator, certain requirements need to be met. Naturally, the laboratory system must be suited to the problem by having observables and interactions that can be mapped to the simulated system. During such an *analogue quantum simulation* the interactions are switched on as required, and the observables of the quantum simulator evolve continuously. However, control over the laboratory system with a sufficiently high degree was not available at that time [1].

In the 1990's, research in this direction gained new momentum with the introduction of *quantum computation*. Here, the peculiar effects of quantum mechanics are used to process abstract information. The smallest information piece is not a "bit" that can only have the value 0 or 1 but a two-level system that can be described by quantum mechanics. This information piece is called a quantum bit or *qubit*. These qubits are grouped in registers then manipulated and made to interact with one another using *quantum gate operations*.

In 1994, Peter Shor presented a factorisation algorithm [2] that would render public key encryption useless. Two years later, Lov K. Grover found a quantum algorithm that could search an unsorted database much faster than its classical counterpart [3].

During the same time, Barenco et al. [4] and DiVincenzo [5] proved that an arbitrary quantum algorithm can be constructed out of single and two-qubit gates. In 1996, Seth Lloyd showed that a quantum computer with such a *universal set of gates* could

perform arbitrary quantum simulations [6]. This type of quantum simulation differs from Feynman's original idea in that quantum computation, i.e., application of discrete quantum gates acting on a register of qubits, is used to calculate the solution of the quantum mechanical problem. Therefore this approach is usually referred to as *digital quantum simulation*.

Quantum computation and quantum simulation are both aspects of the concept of *quantum information processing* (QIP), which aims at using quantum mechanical systems to encode, process and read out information. A suitable quantum mechanical system has to meet certain criteria [7], and several quantum systems are currently beeing investigated as candidates for QIP [8]. The list of candidate systems today includes nuclear spins [9], superconducting Josephson junctions [10, 11], photons [12, 13], quantum dots [14, 15], neutral atoms [16–18] and trapped ions [19, 20].

Development of ion traps started in the 50's of the previous century, when Wolfgang Paul developed the first radio frequency traps for charged particles. Over the following decades these devices had a considerable impact on mass spectrometry, spectroscopy and atomic physics. These so-called Paul traps offer advantages for the charged particles such as isolation from the environment, localization and the possibility to probe them with light. It is especially the latter, which with the advent of the laser, became important. The laser allowed for laser cooling, which was theoretically predicted in 1975 [21] and experimentally demonstrated with ions three years later [22]. In 1980 Neuhauser *et al.* trapped a single ion for the first time [23]. Advanced control over the internal state of the ion followed, such as initialization [24], readout [25–27] and long coherence times of the internal state [28].

With this level of experimental control available, trapped ions already fulfilled several of the criteria for QIP when experimental reasearch started in the mid-1990s. In the last fifteen years, several building blocks of the quantum computer have been demonstrated using trapped ions. As early as 1995, Cirac and Zoller proposed a CNOT gate [29], and in the same year, an experimental two-qubit gate with a single ion was demonstrated [30]. The Cirac-Zoller gate with two ions was realized experimentally in 2003 [31]. At around the same time, an implementation of the Deutsch-Josza algorithm [32] and quantum teleportation [33, 34] were demonstrated.

In recent years, combinations of the building blocks for a two-qubit ion trap quantum processor have been demonstrated [35, 36]. Also a two-ion gate operation with an infidelity of $< 10^{-2}$ was experimentally realized [37]. In theory, this already satisfies the requirement for fault-tolerant quantum computing, given a sufficient number of auxiliary qubits. The same quantum gate operation was successfully used to entangle

fourteen ions [38] and for the implementation of a repetitive quantum error-correction algorithm [39].

However, improvements have not yet reached a stage where a large-scale quantum computer can be realized, as this is ongoing research. Not only has scaling up to a large number of qubits proven to be challenging, but also the infidelity of the operations performed on the qubits limit the complexity of current experiments. Both aspects need significant improvement to allow for the implementation of arbitrary quantum algorithms.

For analogue quantum simulations, on the other hand, requirements on the systems and the fidelity of the performed operations are not as demanding and even systems with a relatively small number of qubits—on the order of 40 to 50—can simulate non-trivial systems that are not solvable with current classical computers [40]. In special cases the number reduces further if the quantum simulator also includes higher-dimensional quantum systems than qubits, e.g., a quantum harmonic oscillator. In the case of digital quantum simulation the number of qubits needed depends on the complexity of the simulated system. In certain cases a digital quantum simulator can compute the solution for a quantum mechanical system with fewer qubits than the simulated system contains [41].

To date, ions have been successfully used to simulate a quantum magnet [42], a frustrated spin system with three [43], a phase transition with up to nine spins [44], a relativistic Dirac particle [45] and an open quantum system [46].

More recently, a simulation of up to six spins has been demonstrated [47] using the Trotter approximation [48]. For this technique, quantum gate operations developed for quantum computation are implemented in rapid succession to approximate the desired time evolution of the simulated system.

This thesis presents several experiments which draw on or contribute to QIP with trapped ions. The thesis is structured as follows: Chapter 2 reviews some aspects of quantum mechanics and introduces the corresponding notation. The level structure and atomic properties of the ion species used, $^{40}Ca^{+}$, is covered in chapter 3. Chapter 4 gives a theoretical description of the ion-laser interaction, as lasers are the main tool to control and manipulate the ion's state. The experimental setup is presented in chapter 5. In addition to the trap and vacuum vessel, the laser systems used are explained. Chapter 6 introduces experimental techniques that are commonly used for the experiments described in the following chapters.

In chapter 7, a precision measurement of the branching ratio of the decay of the excited $4p^2P_{3/2}$ level to the lower lying levels is presented. This spectroscopic measurement was carried out using techniques that are commonly employed in QIP with ions. A one-

dimensional quantum walk in phase space is presented in chapter 8 and the resulting probability distributions are visualized. The quantum walk is of interest for search algorithms in quantum computation, and, e.g., it is investigated in the context of energy transport in molecules involved in photosynthesis in plants [49]. The same wave function reconstruction method was used to visualize the relativistic scattering of a Dirac particle in a quantum simulation presented in chapter 9. If performed with only one additional ion as a second Dirac particle, the resulting problem is in general unsolvable for a classical computer [50].

Finally, chapter 10 gives a summary and an outlook for future experiments. In parallel to the experiments presented in this thesis, a new ion trap was set up. This new setup will open up new possibilities for future experiments and is briefly presented in appendix A.

2 Quantum-mechanical description of cold trapped ions

The following chapter will summarize the mathematical description of a two-level quantum system as well as the quantum-mechanical oscillator. The combination of both systems is sufficient to describe most of the experiments performed in our setup. In addition, certain aspects of the measurement process and quantum computation will be introduced.

2.1 Quantum bits and composite quantum systems

This section briefly summarizes the mathematical notation for a two-level system and for composite quantum systems. It also introduces some basics of quantum computation, such as quantum gates. A more detailed description on this topic can be found in introductory textbooks [48, 51]. In particular, the sections about composite quantum systems were greatly inspired by Ref. [51].

2.1.1 Single quantum bit

In classical computing, the smallest building block is represented by a bit that holds either 0 or 1 as values. This bit is usually implemented as a voltage or a magnetization of an electronic device storing and processing that information. Analogously, the quantum bit—or *qubit*—is defined by selecting two states of a quantum-mechanical system. These states will be represented by the quantum states $|\downarrow\rangle$ and $|\uparrow\rangle$. As a consequence, the state of the qubit is not limited to either $|\downarrow\rangle$ or $|\uparrow\rangle$. Rather any superposition is allowed as stated by quantum mechanics

$$|\psi_{\mathrm{qb}}\rangle = \alpha|\downarrow\rangle + \beta|\uparrow\rangle. \tag{2.1}$$

The coefficients α and β are complex numbers where their absolute value squared represents the probability to measure the qubit in the corresponding state. As each measurement has to have an outcome, they also have to fulfill the normalization condition $|\alpha|^2 + |\beta|^2 = 1$.

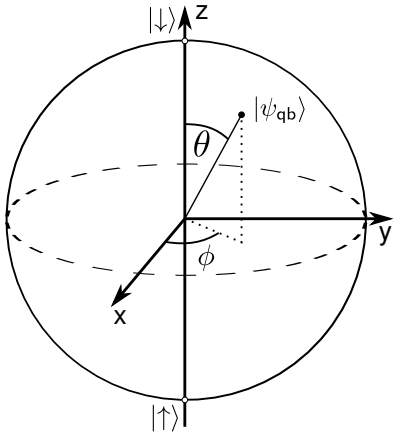

Fig. 2.1: Bloch-sphere representation of a pure qubit state $|\psi_{\mathrm{qb}}\rangle$.

By rewriting Eq. (2.1) as

$$|\psi_{\mathrm{qb}}\rangle = \cos\left(\frac{\theta}{2}\right)|\downarrow\rangle + \sin\left(\frac{\theta}{2}\right)\mathrm{e}^{i\phi}|\uparrow\rangle \tag{2.2}$$

it can be seen that the qubit state can also be represented by the two real numbers θ and ϕ, where a global phase was dropped as it cannot be observed. Because of this, the qubit is also often represented by a vector on a unit radius sphere with rotation angles θ and ϕ. This so-called Bloch vector and the Bloch sphere are shown in Fig. 2.1.

For ions, a qubit can be realized using two long-lived electronic states corresponding to $|\downarrow\rangle$ and $|\uparrow\rangle$.

2.1.2 Product space

The qubit presented in the previous section is a very simple quantum system with only a two-dimensional Hilbert space. More complex systems can be obtained by combining multiple quantum systems which represents an essential step for any quantum computation or quantum simulation.

Let us consider two quantum systems S^A and S^B that do not need to have the same dimensions. Mathematically these systems can be combined using the tensor product

$$\mathcal{H}^{A,B} = \mathcal{H}^A \otimes \mathcal{H}^B. \tag{2.3}$$

Let $|\psi^A\rangle \in \mathcal{H}^A$ and $|\psi^B\rangle \in \mathcal{H}^B$ be the state vectors of their respective systems. Then the product state of the two systems can be expressed as

$$|\psi^A\rangle \otimes |\psi^B\rangle =: |\psi^A, \psi^B\rangle. \tag{2.4}$$

With the basis vectors $\{|n^A\rangle\}$ and $\{|i^B\rangle\}$ of $\mathcal{H}^A$ and $\mathcal{H}^B$, respectively, $\{|n^A\rangle \otimes |i^B\rangle\}$ forms a basis of $\mathcal{H}^{A,B}$. Any vector $|\psi^{A,B}\rangle$ can therefore be written as

$$|\psi^{A,B}\rangle = \sum_{n,i} \alpha_{ni} |n^A, i^B\rangle \tag{2.5}$$

where α_{ni} is the state amplitude satisfying the normalization condition $\sum_{n,i} |\alpha_{ni}|^2 = 1$. From the last expression, the general interest in quantum computation and quantum simulation can be directly motivated. As additional quantum systems are added, the number of state amplitudes α_{ni} grows exponentially as $\dim(\mathcal{H}^A) \cdot \dim(\mathcal{H}^B) \cdot \dim(\mathcal{H}^C) \cdot \ldots$. Even for fewer than one hundred low-dimensional quantum systems, this number becomes impossible to process for a classical computer. However, this does not pose a limit on a quantum computer or a quantum simulator, as they are built on the same physical principles.

It is evident that the formalism presented here is directly applicable to a system comprised of multiple qubits. Such a system is also referred to as a *quantum register* in analogy to the register in classical computers.

With a description for a general state vector in hand, let us now turn to operators that act on the product space. Linear operators that act on their respective Hilbert space can be written as

$$\left[C^A \otimes D^B\right] \sum_{n,i} \alpha_{ni} |n^A, i^B\rangle = \sum_{n,i} \alpha_{ni} |C^A n^A, D^B i^B\rangle \tag{2.6}$$

where C^A or D^B can also be the identity matrix $\mathbb{1}$ to form an operator that only acts on one Hilbert space. The trace of the product space follows as

$$\mathrm{tr}\left[C^A \otimes D^B\right] = \sum_{n,i} \langle n^A, i^B | C^A \otimes D^B | n^A, i^B\rangle = \mathrm{tr}_A\left[C^A\right] \mathrm{tr}_B\left[D^B\right]. \tag{2.7}$$

In quantum mechanics, one important operation is the *partial trace*, which is defined as

$$\mathrm{tr}_A\left[C^A \otimes D^B\right] = \sum_{n} \langle n^A | C^A \otimes D^B | n^A\rangle = \mathrm{tr}_A\left[C^A\right] D^B. \tag{2.8}$$

The resulting operator acts only on $\mathcal{H}^B$.

Entanglement

Entanglement is one of the most peculiar effects in quantum mechanics, as it cannot be explained by classical correlations [52]. Based on our previous discussion, we can define entanglement in the following way:

Any state vector $|\psi^{A,B}\rangle$ that cannot be written as a product state, i.e.

$$|\psi^{A,B}\rangle \neq |\psi^{A}\rangle \otimes |\psi^{B}\rangle \tag{2.9}$$

is called *entangled*.

All other states are called *separable* or *product states*. Entanglement can be generated by the application of suitable operators that act on both systems.

2.1.3 Density matrix representation

Up to this point, only pure quantum states have been considered. For each quantum state $|\psi\rangle$, we define the density operator

$$\varrho := |\psi\rangle\langle\psi|. \tag{2.10}$$

This operator is positive, that is, $\langle\psi|\varrho|\psi\rangle > 0$ and $\mathrm{tr}\left[\varrho\right] = \mathrm{tr}\left[\varrho^2\right] = 1$.

However, it is not always valid to assume a pure state. A given quantum state can be mixed (e.g. due to experimental imperfections) or not fully known. In this case, the density operator is composed out of several pure states ψ_i weighted by λ_i

$$\varrho = \sum_i \lambda_i |\psi_i\rangle\langle\psi_i| \tag{2.11}$$

where $\sum_i \lambda_i = 1$ has to be fulfilled.

For product spaces, the reduced density operator for one Hilbert space can be obtained by tracing over the other Hilbert space:

$$\varrho^A = \mathrm{tr}_B\left[\varrho^{AB}\right]. \tag{2.12}$$

2.1.4 Measurement

The measurement process is another important aspect of quantum mechanics and holds particular interest in the context of quantum computation or simulation. The chosen process determines which information and how much information is extracted from the quantum-mechanical system. A measurement does not necessarily happen only at the end as it affects the quantum state of the system. Various implementations and proposals also use measurements within an algorithm or simulation.

This mathematical description of the measurement process closely follows Ref. [51]. The measurement is described with a set of generalized measurement operators $\{M_m\}$.

For each measurement outcome m, there exists exactly one operator M_m. For pure states the probability of finding m is given by

$$p(m) = \langle\psi|M_m^\dagger M_m|\psi\rangle \tag{2.13}$$

while the quantum state after the measurement is given by

$$|\tilde{\psi_m}\rangle = \frac{M_m|\psi\rangle}{\sqrt{p(m)}}. \tag{2.14}$$

The operators M_m do not have to be Hermitian, as they are not observables $\left(M_m M_{m'} \neq \delta_{m,m'} M_m\right)$. The operator $M_m^\dagger M_m$ is positive, so $p(m) \geq 0$. In order to fulfill $\sum_m p(m) = 1$, the measurement operators have to be complete:

$$\sum_m M_m^\dagger M_m = \mathbb{1}. \tag{2.15}$$

Using the previously introduced density operator, $p(m)$ can be written as

$$p(m) = \mathrm{tr}\left[M_m^\dagger M_m \varrho\right] \tag{2.16}$$

and the quantum state after the measurement as

$$\tilde{\varrho} = \frac{1}{p(m)} M_m \varrho M_m^\dagger. \tag{2.17}$$

In the special case $M_m = P_m$, where the generalized measurement operators are orthogonal projection operators, the number of measurement operators equals the dimension of the Hilbert space. This case is know as *projective* or *von Neumann measurement*.

For a given observable O, the expectation value can be expressed simply using the density operator and the trace

$$\langle O\rangle = \mathrm{tr}\left[\varrho O\right]. \tag{2.18}$$

Analogously, the expectation value of a local observable of a product space is given by

$$\langle O^A\rangle = \mathrm{tr}\left[\varrho^{AB} O^A\right] = \mathrm{tr}_A\left[\varrho^A O^A\right]. \tag{2.19}$$

Measurement on a quantum system is often carried out in the basis of the energy states that is represented by the observable σ_z. Measurement of other observables usually requires the application of suitable unitary operations prior to the measurement.

Another important aspect of quantum measurement is that any generalized measurement on system S^A can be carried out by expanding it to include the ancilla system S^B, applying a unitary operation acting on $\mathcal{H}^{\mathcal{A}} \otimes \mathcal{H}^{\mathcal{B}}$ followed by projective measurement on S^B. This is especially useful in cases where S^A cannot be directly measured.

For the proof of this statement, let S^B have the same number of measurement operators as it has dimensions, while the number of dimensions of S^A is arbitrary. We choose a basis in S^B to be $\{|m^B\rangle\}$ and set it to a fixed state $|0^B\rangle$. Then we define the linear operator

$$U^{AB}|\psi^A, 0^B\rangle = \sum_m M_m^A|\psi^A\rangle \otimes |m^B\rangle \tag{2.20}$$

where $|\psi^A\rangle$ is the state to be measured. It can be shown that U^{AB} exists for the entire Hilbert space formed by $\mathcal{H}^A \otimes \mathcal{H}^B$ [51]. The projective measurement in $\mathcal{H}^B$ is carried out using

$$P_m^B := \mathbb{1}^A \otimes |m^B\rangle\langle m^B|. \tag{2.21}$$

As a consequence, the combined system is transformed to the state

$$C_{\text{norm}} \cdot P_m^B U^{AB}|\psi^A, 0^B\rangle = \frac{M_m^A|\psi^A\rangle|m^B\rangle}{\sqrt{\langle\psi^A|M_m^{A\dagger}M_m^A|\psi^A\rangle}} \tag{2.22}$$

with C_{norm} as a normalization constant. The probability of finding m is given by

$$p(m) = \langle\psi^A, 0^B|U^{AB}P_m^B U^{AB}|\psi^A, 0^B\rangle = \langle\psi^A|M_m^{A\dagger}M_m^A|\psi^A\rangle \tag{2.23}$$

where $P_m^B = P_m^{B\dagger}P_m^B$ was used in the last step. These last two equations can be directly compared to Eqs. (2.14) and (2.13). From this result we can conclude that given a suitable unitary transformation acting on the combined Hilbert space of both systems, those two systems become entangled. In consequence, a generalized measurement of S^A can be realized by means of a projective measurement on S^B.

2.1.5 Quantum gates operations

Controlled unitary operations on one or more qubits are called quantum gates. These quantum gates are analogous to logic gates in classical computers. Given a sufficient set of local and many-qubit operations, any arbitrary quantum algorithm can be realized [48].

Single qubit gates

For a single qubit, the identity and the three Pauli matrices form a complete set that can be used to describe any qubit operation. Their matrix representation is given by

$$\mathbb{1} = \begin{pmatrix} 1 & 0 \\ 0 & 1 \end{pmatrix},\ \sigma_x = \begin{pmatrix} 0 & 1 \\ 1 & 0 \end{pmatrix},\ \sigma_y = \begin{pmatrix} 0 & -i \\ i & 0 \end{pmatrix},\ \sigma_z = \begin{pmatrix} 1 & 0 \\ 0 & -1 \end{pmatrix}. \tag{2.24}$$

The two eigenstates of each Pauli matrix are usually denoted as $|\pm\rangle_j$, where j is either x, y or z.

On the Bloch sphere, the identity corresponds to no operation and each Pauli matrix to a rotation around its respective axis. The corresponding rotation matrices are given by

$$R_x(\theta) = \mathrm{e}^{-i\frac{\theta}{2}\sigma_x} = \begin{pmatrix} \cos\frac{\theta}{2} & -i\sin\frac{\theta}{2} \\ -i\sin\frac{\theta}{2} & \cos\frac{\theta}{2} \end{pmatrix} \tag{2.25}$$

$$R_y(\theta) = \mathrm{e}^{-i\frac{\theta}{2}\sigma_y} = \begin{pmatrix} \cos\frac{\theta}{2} & -\sin\frac{\theta}{2} \\ \sin\frac{\theta}{2} & \cos\frac{\theta}{2} \end{pmatrix} \tag{2.26}$$

$$R_z(\theta) = \mathrm{e}^{-i\frac{\theta}{2}\sigma_z} = \begin{pmatrix} \mathrm{e}^{-i\frac{\theta}{2}} & 0 \\ 0 & \mathrm{e}^{i\frac{\theta}{2}} \end{pmatrix} \tag{2.27}$$

where θ denotes the angle that is covered by the rotation.

Multiple qubit gates

Gates that simultaneously interact with more than one qubit are needed in order for qubits to be of computational use.

One example of a two-qubit interaction is the Mølmer-Sørensen gate [53, 54]. Its matrix representation is given by

$$U_{\mathrm{MS}} = \begin{pmatrix} 1 & 0 & 0 & i \\ 0 & 1 & -i & 0 \\ 0 & -i & 1 & 0 \\ i & 0 & 0 & 1 \end{pmatrix} \tag{2.28}$$

where the matrix is notated in the $\{|\downarrow\downarrow\rangle, |\downarrow\uparrow\rangle, |\uparrow\downarrow\rangle, |\uparrow\uparrow\rangle\}$ basis. The gate mechanism works very well for optical qubits, achieving fidelities above 99% [37]. The properties of the gate were thoroughly investigated in our experiment [55, 56]. Recently, this gate operation was used to demonstrate a digital quantum simulation using the Trotter approach [47].

2.2 Quantum harmonic oscillator

The quantum harmonic oscillator is the other quantum-mechanical system that describes trapped ions. As a matter of fact, trapped ions are often referred to as the toy model for the quantum-mechanical oscillator. This section first briefly revisits the notation for the quantum-mechanical oscillator, as it can be found in almost any introductory textbook

on quantum mechanics (e.g. Refs. [57–59]). This introduction is followed by a description of the driven quantum harmonic oscillator which was inspired by Refs. [19, 57, 60].

By replacing position and momentum in the classical equation of the harmonic oscillator with their respective operators $\hat{x}$ and $\hat{p}$, the Hamiltonian reads

$$H_{\text{h.o.}} = \frac{\hat{p}^2}{2m} + \frac{1}{2}m\omega^2\hat{x}^2 \tag{2.29}$$

where the operators obey the following commutation relation

$$[\hat{x}, \hat{p}] = i\hbar. \tag{2.30}$$

Introducing the operators

$$\hat{a} = \sqrt{\frac{m\omega}{2\hbar}}\hat{x} + \frac{i\hat{p}}{\sqrt{2m\omega\hbar}} \qquad \text{and} \qquad \hat{a}^\dagger = \sqrt{\frac{m\omega}{2\hbar}}\hat{x} - \frac{i\hat{p}}{\sqrt{2m\omega\hbar}} \tag{2.31}$$

we can express the position and momentum operator as

$$\hat{x} = \left(a + a^\dagger\right)\Delta \qquad \text{and} \qquad \hat{p} = i\frac{a^\dagger - a}{2}\frac{\hbar}{\Delta} \tag{2.32}$$

where the characteristic length $\Delta = \sqrt{\hbar/2m\omega}$ was used. This also allows us to rewrite Eq. (2.29) in the quantized form

$$H_{\text{h.o.}} = \hbar\omega\left(a^\dagger a + \frac{1}{2}\right). \tag{2.33}$$

The term $a^\dagger a$ is also referred to as the number operator as its eigenvalues are the numbers of quanta in the harmonic oscillator

$$a^\dagger a|n\rangle = n|n\rangle. \tag{2.34}$$

Hence the Hamiltonian in Eq. (2.33) shows an equidistant level spacing, with the ground state energy given by $E_0 = \hbar\omega/2$. Applying the operators a and $a^\dagger$ to the eigenstates of the oscillator yields the following relations

$$a^\dagger|n\rangle = \sqrt{n+1}|n+1\rangle, \tag{2.35}$$

$$a|n\rangle = \sqrt{n}|n-1\rangle. \tag{2.36}$$

As they increase or decrease the number of quanta in the wave function, the two operators are often referred to as *creation* and *annihilation operators*. It also follows from Eq. (2.35) that applying $a^\dagger$ n times results in the state

$$|n\rangle = \frac{1}{\sqrt{n!}}\left(a^\dagger\right)^n|0\rangle. \tag{2.37}$$

2.2.1 Coherent states

Now let the quantum-mechanical oscillator be driven by a classical oscillating force

$$F(t) = A\sin\left(\omega_{\text{drive}}t + \phi\right) = \frac{A}{2i}\left(\mathrm{e}^{i(\omega_{\text{drive}}t+\phi)} - \mathrm{e}^{-i(\omega_{\text{drive}}t+\phi)}\right). \tag{2.38}$$

The Hamiltonian for this force is given by

$$H_{\text{f}} = -\hat{x}\cdot F(t). \tag{2.39}$$

The time dependence suggests a transformation into the interaction picture, for which we choose $U = \mathrm{e}^{iH_{\text{h.o.}}t/\hbar}$ with $H_{\text{h.o.}}$ from Eq. (2.29). The transformation $H_{\text{int}} = U^\dagger H U$ then yields

$$H_{\text{f,int}} = -\Delta\left(a\mathrm{e}^{-i\omega t} + a^\dagger \mathrm{e}^{i\omega t}\right)\cdot\frac{A}{2i}\left(\mathrm{e}^{i(\omega_{\text{drive}}t+\phi)} - \mathrm{e}^{-i(\omega_{\text{drive}}t+\phi)}\right). \tag{2.40}$$

With the resonance condition $\omega = \omega_{\text{drive}}$, we can make a rotating wave approximation and neglect two of the four terms. The resulting Hamiltonian is given by

$$H_{\text{f,int}} = -\frac{A\Delta}{2i}\left(a\mathrm{e}^{-i\phi} + a^\dagger \mathrm{e}^{i\phi}\right). \tag{2.41}$$

Applying the force can therefore be written as the unitary operator

$$D(\alpha) = \mathrm{e}^{\alpha^* a - \alpha a^\dagger} \tag{2.42}$$

with $\alpha = -A\Delta t\mathrm{e}^{i\phi}/2\hbar$. This operator is called the displacement operator and its application on the ground state creates the *coherent state* $|\alpha\rangle$

$$D(\alpha)|0\rangle = |\alpha\rangle = \mathrm{e}^{-|\alpha^2|/2}\sum_n \frac{\alpha^n}{\sqrt{n!}}|n\rangle. \tag{2.43}$$

Coherent states play an important role in quantum optics and the remainder of this section will discuss some of their properties. As they exhibit certain analogies to classical states, they are also called *quasi-classical states*.

The eigenvalues of the creation and annihilation operators acting on $|\alpha\rangle$ are given by

$$a|\alpha\rangle = \alpha|\alpha\rangle \quad \text{and} \quad \langle\alpha|a^\dagger = \alpha^*\langle\alpha|. \tag{2.44}$$

With these it can be shown that the expectation values for $\hat{x}$ and $\hat{p}$ are given by

$$\begin{aligned}\langle\alpha|\hat{x}|\alpha\rangle &= 2\Delta\mathrm{Re}\{\alpha\} \quad \text{and}\\ \langle\alpha|\hat{p}|\alpha\rangle &= \frac{\hbar}{\Delta}\mathrm{Im}\{\alpha\}.\end{aligned}$$

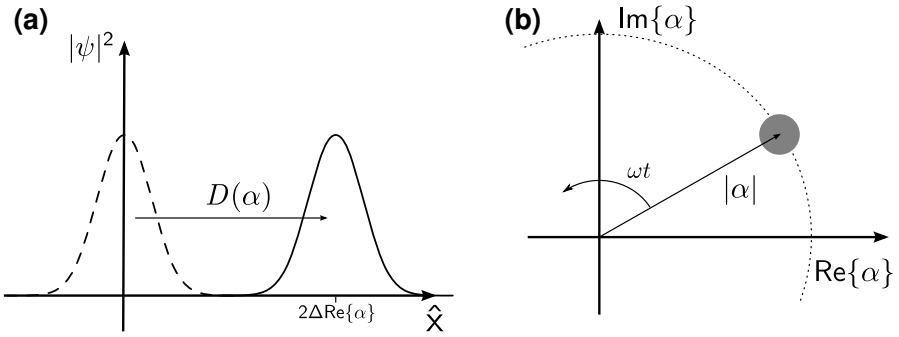

Fig. 2.2: **(a)** Application of the displacement operator $D(\alpha)$ on the ground state. The wave function is translated in phase space without distortion of its shape. **(b)** Phase space representation of the coherent state $|\alpha\rangle$. $\langle\alpha|\hat{x}|\alpha\rangle$ and $\langle\alpha|\hat{p}|\alpha\rangle$ are represented in units of 2Δ and $\hbar/\Delta$, respectively. The time evolution of the coherent state is indicated by the rotation arrow and the rotation frequency is given by the trap frequency ω.

As a result, the real part of the coherent state is associated with the position and the imaginary part with the momentum operator. It is therefore convenient to write $|\alpha\rangle = \langle\hat{x}\rangle + i\langle\hat{p}\rangle$, which can be visualized in the complex plane (see Fig. 2.2).

One important property of coherent states is that the expectation values for position, momentum and energy are equal at all times to those of a classical system. Another important property is that the wave packet shows no dispersion but a width that is constant in time as $|\alpha\rangle$ evolves in the harmonic oscillator. For the complete calculation, the reader is referred to Ref. [57]; only the results are stated here.

To find the dispersion of the wave packet the expression for the coherently displaced wave function $\psi_{\mathrm{coh}}(x)$ has to be evaluated in position space

$$\langle x|\alpha\rangle = \mathrm{e}^{\frac{\alpha^{*2}-\alpha^2}{4}} \mathrm{e}^{ix\langle\alpha|\hat{p}|\alpha\rangle/\hbar} \psi_0(x - \langle\alpha|\hat{x}|\alpha\rangle). \tag{2.45}$$

Here, ψ_0 is the wave function of the ground state which is displaced by $\langle\alpha|\hat{x}|\alpha\rangle$ from the origin. The phase factor is position-dependent, but the shape of the wave function is not. This result can also be obtained by looking at the standard deviation of the position and momentum operators of $|\alpha\rangle$

$$\delta\hat{x}_\alpha = \Delta \quad \text{and} \quad \delta\hat{p}_\alpha = \frac{\hbar}{2\Delta}, \tag{2.46}$$

which are constant in time.

The time-dependent behaviour of the wave packet is retrieved by using the time-independent Hamiltonian $H_{\mathrm{h.o.}}$ from Eq. (2.33) on a initial and coherent state

$|\psi(t=0)\rangle = |\alpha_0\rangle$

$$|\psi(t)\rangle = \mathrm{e}^{-iH_{\mathrm{h.o.}}t/\hbar}|\psi(0)\rangle. \tag{2.47}$$

Evaluating this expression yields

$$|\psi(t)\rangle = \mathrm{e}^{-i\omega t/2}|\alpha(t)\rangle \tag{2.48}$$

with

$$\alpha(t) = \alpha_0 \mathrm{e}^{i\omega t}. \tag{2.49}$$

This expression shows that $\alpha(t)$ remains a coherent state but oscillates in phase space around the origin with the trap frequency ω.

Chapter 4 will present how the displacement operator can be realized in an ion trap using a bichromatic light field. However, the oscillation in phase space cannot be observed in our experiments as the laser creating the displacement acts as a reference oscillator that rotates with the coherent state.

3 Atomic properties of $^{40}Ca^{+}$

All experiments described in this thesis were carried out using $^{40}Ca^{+}$. The two qubit levels are realized using the ground state and a higher lying state that is connected via a dipole-forbidden transition. This configuration results in lifetimes of the upper qubit state on the order of a second, which is several orders of magnitude longer than the typical length of the laser pulses used to manipulate or read out the qubit.

With one valence electron, $^{40}Ca^{+}$ has a level structure similar to that of neutral alkali atoms. Fig. 3.1 shows the three lowest orbitals available to the valence electron. The ground-state is a 4S orbital while the next higher level is a 3D orbital. As the transition from the 3D orbital to the 4S orbital is dipole-forbidden, the 3D orbital is a meta-stable state.

The next higher level is the 4P orbital, which is connected via dipole transitions to the ground state as well as to the 3D orbital. The decay from the P-orbitals is therefore a competing process between both possible decay channels.

The numeric value of the *branching ratio* of these decay channels can be estimated by looking at the spontaneous decay rate Γ_{sp}. For a simple two-level atom this is given by [58]

$$\Gamma_{\mathrm{sp}} = \frac{e^2\omega^3 D_{12}^2}{3\pi\epsilon_0\hbar c^3} = A_{12} \tag{3.1}$$

where D_{12} denotes the dipole moment of the atom and A_{12} is the Einstein coefficient associated with the spontaneous decay. With the reduced Planck constant $\hbar$, the speed of light c and the elementary charge e beeing constant most significant in the expression above is the cubic dependence on the transition frequency ω. With wavelengths of ≈ 400 nm for the P $\rightarrow$ S decay and ≈ 850 nm for the P $\rightarrow$ D decay, one expects a ratio of approximately 10:1, which is close to that of the measured data [61]. The branching fractions are also given in Fig. 3.1. For more advanced theoretical calculations on this topic, the reader is referred to the references given in chapter 7.

The 3D orbital and the 4P orbital consist of two-levels $D_{3/2}$, $D_{5/2}$ and $P_{1/2}$, $P_{3/2}$, respectively. In both cases the two-levels are well separated by a few nanometers. As there is no dipole transition between the $P_{1/2}$ and the $D_{5/2}$ level, the latter is well suited

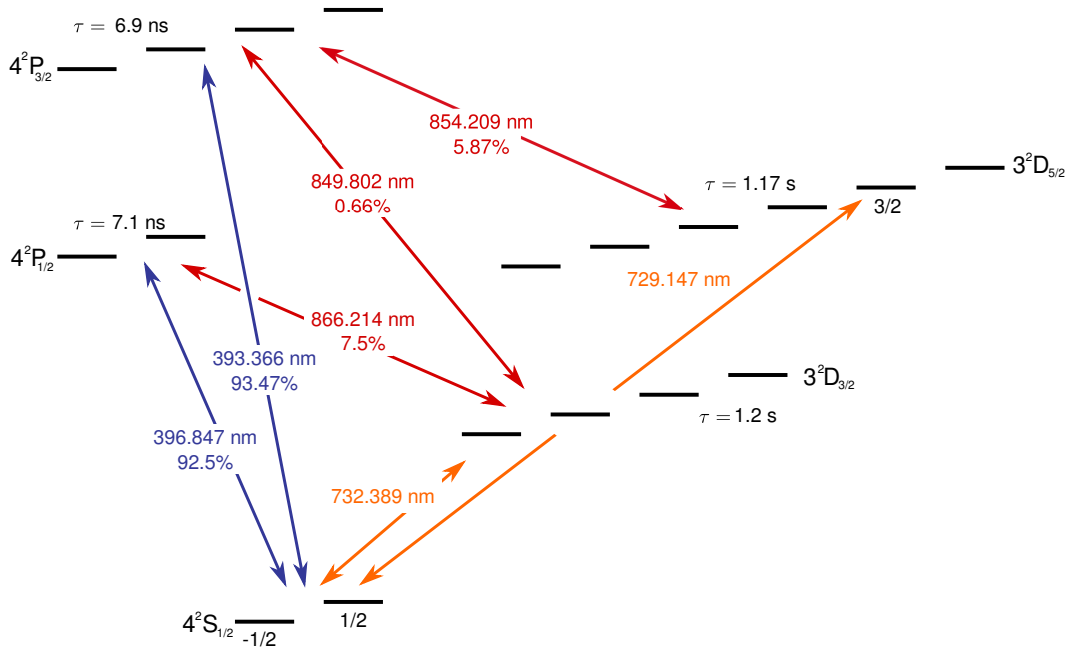

Fig. 3.1: Detailed level scheme of $^{40}Ca^{+}$ showing the lowest three orbitals of the valence electron. All possible transitions are indicated along with their wavelength in air, their natural lifetime and their branching fractions given in percent [61–64]. Our setup included lasers for all transitions shown except the one at 732 nm connecting the $S_{1/2}$ and the $D_{3/2}$ orbital.

as the upper qubit level. Both the missing dipole transition and the lifetime of this meta-stable state make it possible to use the $S_{1/2} \leftrightarrow P_{1/2}$ transition for state detection. Excitation on the $S_{1/2} \leftrightarrow P_{1/2}$ transition at 397 nm and the $D_{3/2} \leftrightarrow P_{1/2}$ transition at 866 nm will cause the ion to fluoresce, if it is in the $S_{1/2}$ or the $D_{3/2}$ level, but not if it is in $D_{5/2}$. This allows one to discriminate between the two qubit levels. The second light field at 866 nm is necessary to avoid unwanted trapping of population in the $D_{3/2}$ level.

In order to use the ground state and the $D_{5/2}$ level as a qubit the degeneracy of the levels has to be lifted. For this purpose, a magnetic field of a few Gauss is applied that splits all levels into sublevels by a few megahertz due to the Zeeman effect. At this field strength, the fine structure cannot be resolved for the 21 MHz-broad dipole transitions, but for the quadrupole transitions which have a linewidth of about 0.14 Hz.

The external magnetic field splits the $S_{1/2}$ manifold into two sublevels $m_j \pm 1/2$ and the $D_{5/2}$ level into six sublevels $m_j = \pm 1/2, \pm 3/2, \pm 5/2$. For most of our experiments the qubit was encoded in the $S_{1/2}, m_j = 1/2$ and $D_{5/2}, m_j = 3/2$ levels.

One important property of $^{40}Ca^{+}$ is that it has a nuclear spin of 0. This property

causes the levels to have a linear dependence on the magnetic field and makes them sensitive to magnetic field fluctuations. The shift in transition frequency for our qubit levels is given by

$$\Delta\omega_{S\to D} = \frac{\mu_B}{\hbar}\left(m_S g_{S_{1/2}} - m_D g_{D_{5/2}}\right) B \tag{3.2}$$

where μ_B is the Bohr magneton and g_i denotes the Landé-factor of the level i. The qubit using the $|\mathrm{D}_{5/2}, m = +3/2\rangle \leftrightarrow \mathrm{S}_{1/2}, m = +1/2\rangle$ transition does not show the lowest sensitivity to magnetic field fluctuations, which would be the case for $\Delta m = 0$ transitions with a sensitivity of 560 kHz/G. The sensitivity of the used qubit is two times higher but the coupling strength can be maximized by properly setting the polarization and direction of the light field with respect to the magnetic field. In turn, the coupling strength to other levels gets supressed yielding less off-resonant excitation of these levels for operations with the same laser intensity. As a consequence, higher laser intensities can be used that achieve the same fidelity, allowing us to shorten operation times.

4 Ion-laser interaction

This chapter covers the laser-ion interaction that is used in all our experiments for coherent state manipulation. The mathematical description of the interaction will be briefly presented and certain aspects that have to be considered for an experimental implementation will be discussed. The chapter also includes a presentation of the bichromatic light field used to realize the displacement operator $D(\alpha)$ as described in Sec. 2.2.1. The chapter is concluded by a description of how $D(\alpha)$ can be used to reconstruct the wave function of the ion's motional state. This method was used in the experiments presented in chapters 8 and 9.

4.1 Driving the quadrupole transition

The quadrupole transition between $S_{1/2}$ and $D_{5/2}$ can be driven with a strong coherent light field at 729 nm. For this interaction, the gradient of the electric field $E(t)$ couples to the electronic quadrupole moment. This coupling causes the occupation probability of the electron to oscillate between the two states. For the following description, it is convenient to assign a pseudo-spin to the coupled states. The lower(upper) energy level can then be identified with $|\downarrow\rangle(|\uparrow\rangle)$. The Hamiltonian of this interaction is given by

$$H_{\mathrm{I}} = \hbar\Omega \left(\sigma^{+} + \sigma^{-}\right) \left(\mathrm{e}^{i(kx-\nu_{\mathrm{I}}t+\phi)} + \mathrm{e}^{-i(kx-\nu_{\mathrm{I}}t+\phi)}\right) \tag{4.1}$$

where $\sigma^{+} = \frac{1}{2}(\sigma_x + i\sigma_y)$ and $\sigma^{-} = \frac{1}{2}(\sigma_x - i\sigma_y)$ are Pauli spin operators. The wave vector k, the frequency of the laser beam ν_l, and its phase ϕ are properties of the light field. The *Rabi frequency* Ω describes the strength of the coupling between the two atomic states. An expression for the Rabi frequency can be derived by comparing the interaction Hamiltonian in Eq. (4.1) with the expression for the induced quadrupole moment $\hat{Q}$ coupling of the gradient of the electric field $E(t)$

$$H_I = \hat{Q}\nabla E(t). \tag{4.2}$$

This equation takes the form of Eq. (4.1) if we define Ω as [64, 65]

$$\Omega = \left| \frac{eE_0}{2\hbar} \langle S, m| \left(\boldsymbol{\epsilon}\cdot\boldsymbol{r}\right) \left(\boldsymbol{k}\cdot\boldsymbol{r}\right) |D, m'\rangle \right|. \tag{4.3}$$

Here, E_0 is the amplitude of the electric field, $\boldsymbol{r}$ the position operator of the valence electron relative to the center of mass of the atom and $\boldsymbol{\epsilon}$ the polarisation vector. The gradient of the electric field in H_I shows up in this expression as it is proportional to $\boldsymbol{k}$. Selection rules for this type of transition allow for $\Delta m = 0, \pm 1, \pm 2$.

From Eq. (4.3) it can be seen that geometric factors such as polarisation as well as the angle between the quantization axis and the laser beam influence the coupling strength. This expression can be evaluated further to give the more convenient form [64]

$$\Omega = \frac{eE_0}{2\hbar}\sqrt{\frac{15}{c\alpha}\frac{\Gamma_{\mathrm{D5/2}}}{k^3}}\Lambda(m, m')g^{\Delta m}(\phi, \gamma) \tag{4.4}$$

with c as the speed of light and $\Gamma_{\mathrm{D}_{5/2}}$ the spontaneous decay rate of the $\mathrm{D}_{5/2}$ level. Λ represents the Clebsch-Gordon coefficient for the Zeeman sublevels m and m' of the $\mathrm{S}_{1/2}$ and the $\mathrm{D}_{5/2}$ manifold (see appendix C).

The function $g^{\Delta m}(\phi, \gamma)$ gives only the geometric dependence of Ω. The angle between the laser beam and the quantization axis is given by ϕ. The angle between a linear polarization and the magnetic field vector projected onto the plane of incidence is represented by γ. Explicit expressions for $g^{\Delta m}(\phi, \gamma)$ can be found in Ref. [66].

One can make use of the geometric dependency in order to maximize or minimize the coupling for certain transitions, depending on the given task that is carried out with the laser.

4.2 Ion-laser Hamiltonian

With the ion modeled as a qubit and confined in the harmonic potential of the trap, the system can be described by the following two Hamiltonians

$$H_{\mathrm{h.o.}} = \frac{p^2}{2m} + \frac{1}{2}m\omega^2 x^2 \tag{4.5}$$

$$H_{\mathrm{e}} = \frac{1}{2}\hbar\nu\sigma_z. \tag{4.6}$$

The first Hamiltonian represents the ion with mass m oscillating with frequency ω, while the second accounts for the ions internal or electronic state with its energy splitting of $\hbar\nu$. The interaction of the internal state with an external light field is given by Eq. (4.1). All three Hamiltonians combined are needed to describe the laser-ion interaction. We

will rewrite them using the creation and annihilation operators a and $a^\dagger$ as

$$H_0 = H_{\text{h.o.}} + H_{\text{e}} = \hbar\omega\left(a^\dagger a + \frac{1}{2}\right) + \frac{1}{2}\hbar\nu\sigma_z \tag{4.7}$$

$$H_{\text{l}} = \hbar\Omega\left(\sigma^+ + \sigma^-\right)\left(\mathrm{e}^{i\eta\left(a+a^\dagger\right)}\mathrm{e}^{-i(\nu_{\text{l}}t-\phi)} + \mathrm{e}^{-i\eta\left(a+a^\dagger\right)}\mathrm{e}^{i(\nu_{\text{l}}t-\phi)}\right) \tag{4.8}$$

where we have introduced the Lamb-Dicke parameter η, defined as

$$\eta = \boldsymbol{k}\boldsymbol{e}_z\sqrt{\frac{\hbar}{2m\omega_z}} \tag{4.9}$$

with $\boldsymbol{e}_z$ being the unit vector along the trap axis. The Lamb Dicke parameter indicates the ability of the light field to couple to the ion's motional state along the z-direction of the trap.

After combining $H_{\text{h.o.}}$ and H_e into H_0, we go into the interaction picture via the transformation $H_{\text{int}} = U^\dagger\left(H_0 + H_l\right)U$, where $U = \mathrm{e}^{iH_0t/\hbar}$. A rotating-wave approximation yields the Hamiltonian

$$H_{\text{int}}(t) = \hbar\Omega\left(\sigma^+\mathrm{e}^{i\eta\left(a\mathrm{e}^{-i\omega t}+a^\dagger\mathrm{e}^{i\omega t}\right)}\mathrm{e}^{-i((\nu_{\text{l}}-\nu)t-\phi)} + h.c.\right). \tag{4.10}$$

The detuning of the laser from the resonance frequency determines the coupling between the two qubit states and the motional state of the ion. If the detuning $\nu - \nu_l = s\cdot\omega$ for integer s, then the two states $|\downarrow, n\rangle$ and $|\uparrow, n+s\rangle$ are coupled, where n is the vibrational quantum number. The case $s = 0$ is called a carrier transition, while $s < 0$ or $s > 0$ are referred to as the $|s|$th red and blue sideband, respectively. The matrix element $\langle n+s|\mathrm{e}^{i\eta(a+a^\dagger)}|n\rangle$ is given by Ref. [67]

$$\langle n+s|\mathrm{e}^{i\eta(a+a^\dagger)}|n\rangle = \sqrt{\left(\frac{n_<!}{n_>!}\right)}\mathrm{e}^{-\frac{\eta^2}{2}}\eta^{|s|}L_n^{|s|}(\eta^2) \tag{4.11}$$

where $n_<$ is the smaller number of $\{n+s, n\}$ and $n_>$ the other. $L_n^\alpha(x)$ is the given by the Laguerre polynomial

$$L_n^\alpha(x) = \sum_{s=0}^{n}(-1)^m\left(\frac{n+\alpha}{s-n}\right)\frac{x^s}{s!}. \tag{4.12}$$

One important result of Eq. (4.11) is the dependence of the coupling strength on the number of quanta in the motional state. A plot of the coupling strength of the carrier transition and the first sideband transition as a function of the phonon number in the motional state is shown in Fig. 4.1. The sideband transitions are resolvable for $\Omega \ll \omega$, which is the case for typical parameters in our setup.

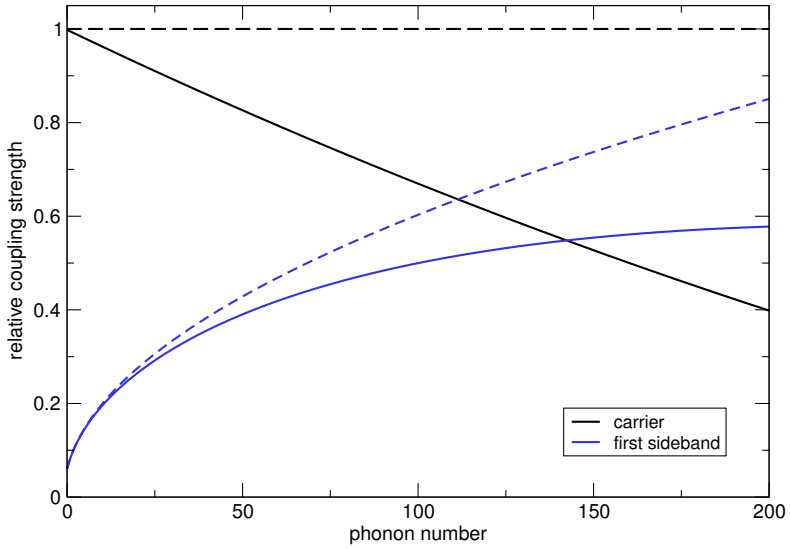

Fig. 4.1: Relative coupling strength of the carrier and first sideband as a function of the phonon number in the motional state for $\eta = 0.06$. The dashed lines are derived taking only first order effects into account. The deviation between the solid and dashed lines illustrates how higher order effects become more prominent with more phonons in the motional state.

4.3 The Lamb-Dicke regime

For low values of n the spatial extent of the ion's wave function is much smaller than the wavelength of the incident light. When the inequality $\eta(2n+1) \ll 1$ is fulfilled Eq. (4.10) can be rewritten by using a Taylor expansion on the $\mathrm{e}^{i\eta(a\mathrm{e}^{-i\omega t}+a^\dagger \mathrm{e}^{-i\omega t})}$ part and neglecting higher-order terms $\mathcal{O}(\eta^2)$. This simplification yields the Hamiltonian

$$H_{\mathrm{int}}(t) = \hbar\Omega\sigma^+ \left(1 + i\eta\left(a\mathrm{e}^{-i\omega t} + a^\dagger \mathrm{e}^{i\omega t}\right)\right) \mathrm{e}^{-i((\nu_l-\nu)t-\phi)} + h.c. \tag{4.13}$$

which has three spectral components. These are considered in turn below.

Carrier transition For $\nu_l = \nu$, the motional quantum number stays the same and only the electronic state is changed. The Hamiltonian further simplifies to

$$H_{\mathrm{car}}(t) = \hbar\Omega\left(\sigma^+ e^{i\phi} + \sigma^- e^{-i\phi}\right). \tag{4.14}$$

This interaction couples the states $|\downarrow, n\rangle \leftrightarrow |\uparrow, n\rangle$.

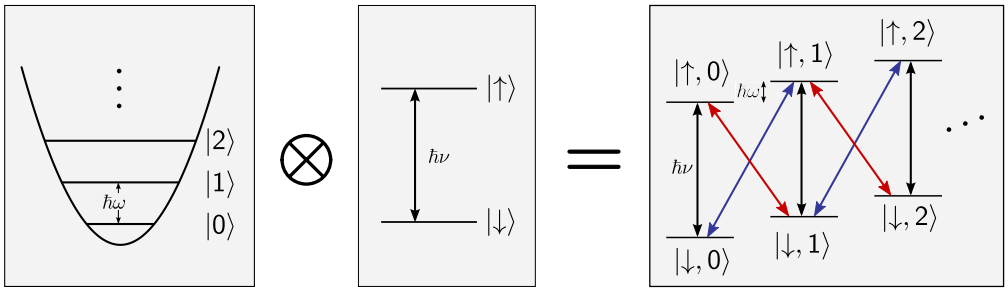

Fig. 4.2: Schematic representation of the harmonic oscillator of the trap combined with the two-level system of the qubit. On the right-hand side, carrier transitions are drawn in black and the red and blue sideband transitions in their respective colors.

Red sideband In the case of $\nu_l = \nu - \omega$, the states $|\downarrow, n\rangle \leftrightarrow |\uparrow, n-1\rangle$ are coupled by the effective Hamiltonian

$$H_{\text{red}}(t) = i\hbar\eta\Omega\left(a\sigma^+ e^{i\phi_{\text{red}}} - a^+\sigma^- e^{-i\phi_{\text{red}}}\right) \tag{4.15}$$

The coupling strength is given by $\Omega_{n,n-1} = \Omega\sqrt{n}\eta$.

Blue sideband For $\nu_l = \nu + \omega$, the states $|\downarrow, n\rangle \leftrightarrow |\uparrow, n+1\rangle$ are coupled as described by

$$H_{\text{blue}}(t) = i\hbar\eta\Omega\left(a^+\sigma^+ e^{i\phi_{\text{blue}}} - a\sigma^- e^{-i\phi_{\text{blue}}}\right) \tag{4.16}$$

Similar to the case of red sideband the coupling strength is given by $\Omega_{n,n+1} = \Omega\sqrt{n+1}\eta$.

Fig. 4.2 shows a graphical presentation of the two-level system combined with a harmonic oscillator and the coupling of the three transitions.

The high level of control available over the internal and motional state of the ion makes ions very good candidates for the investigation of quantum states. All three transitions have applications: the red sideband is used for sideband cooling, enabling the ion to reach the ground state of motional with very high probability. The blue sideband can be used to analyze the motional state [68] or to transfer information from the internal state to the ion's motional state [29].

For the case of a resonant excitation of the carrier transition, the time evolution of the state can be expressed by $|\psi(t)\rangle = U(t)|\psi(0)\rangle$, where

$$U = \begin{pmatrix} \cos\Omega t & -ie^{-i\phi}\sin\Omega t \\ -ie^{i\phi}\sin\Omega t & \cos\Omega t \end{pmatrix}. \tag{4.17}$$

This time evolution can be visualized as a rotation on the Bloch sphere (see Fig. 2.1) around the $\cos(\phi)\boldsymbol{e}_x + \sin(\phi)\boldsymbol{e}_y$ direction. The phase ϕ is set by the first laser pulse, and all following pulses are referenced to it. Acousto-optic modulators (AOM) are used to control the relative phase of the external light. In the experiment, setting the phase of the light field allows us to realize the $R_x(\theta)$ and $R_y(\theta)$ rotations presented in Sec. 2.1.5.

In the case of multiple ions, the spectrum exhibits additional components due to the increased number of vibrational modes of the ion crystal. For the experiments described in this thesis, at most two ions were used. In our setup the potential has one direction with a weaker confinement compared to the other two. The two ions have six vibrational modes. Three center of mass (COM) modes, one breathing mode along the weaker axial direction of the trap and two rocking modes where the ions rotate around their center of mass moving along the axial and one of the two transverse directions [69]. All experiments making use of a vibrational mode used the COM mode in the axial direction as it has the lowest frequency. A detailed analysis of the formation of ion crystals and their normal modes is given in Ref. [64].

4.3.1 AC-Stark shifts

As the resonant interaction is limited to the equatorial plane of the Bloch sphere, a third rotation around the z-axis ($R_z(\theta)$) is needed in order to realize arbitrary single qubit rotations. This rotation is achieved by addressing the ion with an off-resonant beam with a detuning much bigger than the Rabi frequency ($\delta \gg \Omega$). The non-resonant light field will induce the so-called *AC-Stark effect* that will shift both levels in opposite directions [70]. The direction of the shift depends on the detuning of the beam. If the beam is detuned to the red the levels will split further, while in the case of a blue detuning they will approach one another.

The relative difference in frequency caused by this effect amounts to

$$\delta_{\mathrm{AC}} = 2\frac{\Omega^2}{\delta} \tag{4.18}$$

which has equal contributions from both levels.

The AC-Stark effect has two important consequences. On one hand, by setting $\delta \gg \Omega$, the time evolution is a rotation on the Bloch sphere around the z-axis completing (with Eq. (4.17)) the set of all three rotations described in Sec. 2.1.5. A convenient feature of this technique is that there is no need for phase coherence between the far-detuned beam and other beams involved in the experimental sequence.

On the other hand, the AC-Stark shift can also cause unwanted effects. Important examples are the sideband transitions discussed in the previous section. If the laser

frequency is set on resonance with the sideband, the light field will also couple to the much stronger carrier transition. Intensity fluctuations will directly translate to relative phase fluctuations of the superposition state. This unwanted effect can be canceled by extracting a second light field from the same beam with a detuning in the opposite direction and a Rabi frequency that exactly cancels this effect. By using the same beam, the second light field has the same intensity fluctuations as the light field used for the actual coupling [71]. However, as our experiments usually do not rely on single-sideband operations with very high fidelity, this technique is not implemented in the current setup.

4.3.2 Off-resonant excitations

Another unwanted effect is the occurrence of off-resonant excitations. These also occur, e.g., when driving a sideband transition. Because the light field also drives the carrier transition coherently, the population of the target state shows unwanted oscillations. This effect can be on the order of a few percent and therefore should be avoided if one aims to achieve high-fidelity operations.

However, by adiabatically switching on and off the laser pulse that drives the transition, this effect can be largely suppressed. The benefit of this method is twofold: Firstly it avoids high frequency components in the Fourier transform. Secondly it adiabatically transforms the off-resonant excitations to zero since the amplitude of the pulse starts and stops at zero. Additional information on this topic, especially concerning the hardware that is used in our experiment to achieve this, is given in Ref. [72].

4.4 State-dependent coherent displacement

By combining the red- and the blue-sideband Hamiltonian (Eqs. (4.15) and (4.16)), another interesting application can be realized. The Hamiltonian of this bichromatic light field can be rewritten as

$$\begin{aligned} H_{\mathrm{disp}} = \hbar\eta\Omega \left[\sigma_x \cos\phi_+ - \sigma_y \sin\phi_+\right] \\ \otimes \left[(a + a^\dagger)\cos\phi_- + i(a^\dagger - a)\sin\phi_-\right] \end{aligned} \tag{4.19}$$

where $2\phi_+ = \phi_{\mathrm{red}} + \phi_{\mathrm{blue}}$ and $2\phi_+ = \phi_{\mathrm{red}} + \phi_{\mathrm{blue}}$ were used. The sum and the difference of the creation and annihilation operators can be identified as the $\hat{x}$ and $\hat{p}$ operators of the harmonic oscillator. With the additional identification $\alpha = i\eta\Omega t/\Delta$ (Δ being the width of the ground state of the harmonic oscillator), it is evident that application of the Hamiltonian is very similar to the displacement operator presented in Sec. 2.2.1.

However, in contrast to the standard displacement operator, the displacement operator of the bichromatic light field is state-dependent. The axis of the displacement within phase space can be set arbitrarily with ϕ_-. The direction along this axis is determined by the internal state of the ion and the setting of ϕ_+ determines which eigenstates are selected.

It should be noted that the Hamiltonian presented is only valid within the Lamb-Dicke regime. For states with high phonon numbers, higher order terms of η become relevant and have to be taken into account. As a state gets displaced from the origin, its average phonon number increases quadratically with $|\alpha|$. In Fig. 4.1 it can be seen that for a state with 100 phonons, the coupling strength of the sidebands is already reduced by one-sixth in comparison to the Lamb-Dicke approximation. These higher order effects set certain boundaries to the displacement operations that can be realized in our setup.

Experimental implementation of the displacement operator is straightforward. As the qubit in $^{40}Ca^+$ is realized with two levels connected via a quadrupole transition, the bichromatic light field can be set up in a co-propagating configuration. This configuration can directly be achieved by sending the light of the laser through an AOM driven with two frequencies that differ by twice the trap frequency. As both beams share the same optical path, phase stability is not compromised by mechanical vibrations or thermal drifts in the setup. Both beams have the same intensity and opposite detuning from the carrier transition avoiding AC-Stark shifts from this transition. However, AC-Stark shifts from other quadrupole transitions and the dipole transitions are present. These shifts can be compensated for by shifting the frequencies of the two light fields by the same amount and by adjusting the laser intensities. For the experiments presented in this thesis adjusting the frequencies was sufficient to realize the displacement operation with very high fidelity.

On the other hand, the displacement operation in phase space is very sensitive to the trap frequency. The trap frequency has to be stable to about 10 Hz for the experiments described in this thesis, corresponding to a stability of 10^{-5}. Slow drifts or a simple mismatch of the trap frequency compared to the bichromatic light field are possible error sources that have to be checked carefully. A mismatch in frequency modifies the displacement operation so that it is performed in a circle rather than a straight line, where the curvature is given by the detuning [73]. This behaviour can be used to match the frequencies of the trap and the laser or to check for drifts.

To this end, the ion is prepared in its motional and electronic ground state. As the electronic ground state $|-\rangle_z \equiv |S_{1/2}, m = 1/2\rangle$ is a superposition of eigenstates of σ_x or σ_y, the wave packet coherently splits under the evolution of H_{disp} from Eq. (4.19) into

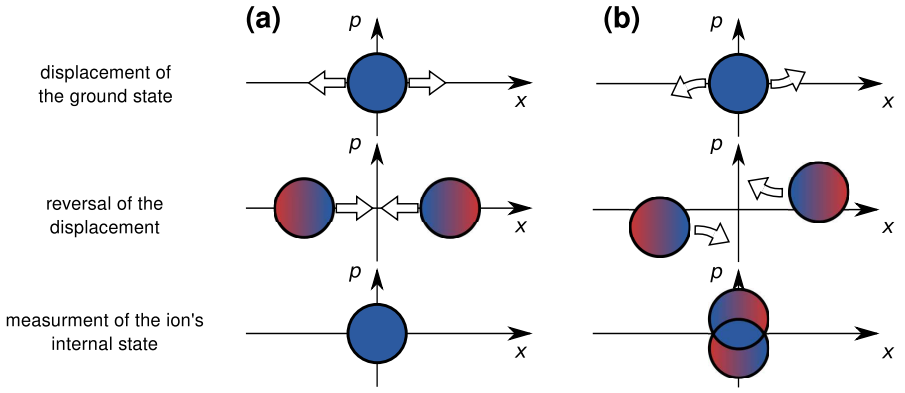

Fig. 4.3: Schematic representation in phase space of the procedure to match the laser and the trap frequencies. The electric ground state of the ion is colored in blue and excitation of the ions' internal state indicated by red. **(a)** Case where the frequencies of the bichromatic light field exactly match the trap frequency. The wave packet coherently splits along a straight line and the reversed displacement operation recombines the wave packets in the center. **(b)** In the case of a detuning, the displacement is performed along a curved line. Therefore, the two wave packets will not perfectly overlap in the center upon a reversed application of the displacement operator. The result is a remaining excitation in the internal state of the ion.

two parts along the axis set by ϕ_-, where the internal states are the two eigenstates set by ϕ_+. The displacement operator is applied for a suitable time, followed by a small waiting time and the sequence is concluded by a reversal of the displacement, recombining the wave packets in the ground state. If the frequencies are set correctly, the two wave packets interfere back to the electronic ground state and the internal state of the ion shows no excitation. In the case of a frequency mismatch, the curved displacement inhibits the two wave packets from overlapping perfectly, resulting in an excitation of the internal state of the ion. A schematic representation of the two cases is given in Fig. 4.3.

4.5 Wave function reconstruction

With the bichromatic light field introduced in Sec. 4.4, it is possible to reconstruct the probability distribution of a wave function along a line in phase space [74]. This line is perpendicular to the displacement performed and determined by ϕ_- in Eq. (4.19). In order to reconstruct the distribution along the $\hat{x}$-axis in phase space ϕ_- and ϕ_+ are set

to 0, yielding the unitary operation

$$U_p = \mathrm{e}^{i/\hbar H_{\mathrm{disp}}} = \mathrm{e}^{-ik\hat{x}\sigma_x/2}. \tag{4.20}$$

Here $k = 2\eta\Omega_{\mathrm{p}}t/\Delta$ where Δ is again the width of the ground state and t the time for which the bichromatic light field is applied. With the equality $\exp(i\theta\sigma_x) = \cos(\theta)I + i\sin(\theta)\sigma_x$ and $\sigma_i\sigma_j = \epsilon_{ijk}\sigma_k$ (I and σ are given in Eq. (2.24)), it can be shown that application of this unitary operation followed by a fluorescence measurement is equivalent to measuring the observable

$$O(k) = U_p^\dagger \sigma_z U_p = \cos(k\hat{x})\sigma_z + \sin(k\hat{x})\sigma_y. \tag{4.21}$$

From this expression, it can be seen that the probability distribution $\langle\delta(\hat{x} - x)\rangle$, or $|\Psi(\hat{x})|^2$ in the case of pure states, can be obtained with two measurements. By setting the internal state of the ion to either $|+\rangle_z$ or $|+\rangle_y$, a measurement with varying k will yield the even or uneven Fourier components of the probability distribution. This procedure performs a generalized measurement on the motional state of the ion as presented in Sec. 2.1.4. The displacement operator constitutes the unitary operation on the combined system of the internal and motional state of the ion. As this operation entangles both systems, a projective measurement on the qubit allows one to measure the motional state of the ion.

Prior to the desired eigenstate being set, we have to trace out the internal state of the ion, leaving the partial density operator of the motional state of the ion unchanged. This additional step is necessary as the internal and external state of the ion generally become entangled during the preceding experiment. To this end, all population in $|\mathrm{S}_{1/2}, m = 1/2\rangle \equiv |-\rangle_z$ is transfered to the auxiliary state $|\mathrm{D}_{5/2}, m = 5/2\rangle$ manifold, and the population in $|\mathrm{D}_{5/2}, m = 3/2\rangle \equiv |+\rangle_z$ is then transferred to $|-\rangle_z$. These two first pulses are usually performed using Rapid Adiabatic Passages [75] as these are less sensitive to the phonon number in the motional state compared to a normal π-pulse on resonance. A short pulse at 854 nm excites the population in $|\mathrm{D}_{5/2}, m = 5/2\rangle$ to $|\mathrm{P}_{3/2}, m = 3/2\rangle$, from which it spontaneously decays to $|-\rangle_z$. The efficiency of this process is $> 99\%$, limited only by the small branching fraction to the $\mathrm{D}_{3/2}$ state. Fig. 4.4 depicts all relevant levels and the four steps of this process. At the end of the recombination process it is possible to set the ion's internal state as required for this analysis method. The disadvantage of this procedure is that the motional state of the ion might change but the probability is very low due to the small Lamb-Dicke parameter. The problem of changing the ion's motional state could be completely circumvented by analyzing the motional state associated with internal states $|-\rangle_z$ and $|+\rangle_z$ separately, resulting in twice the measurement time.

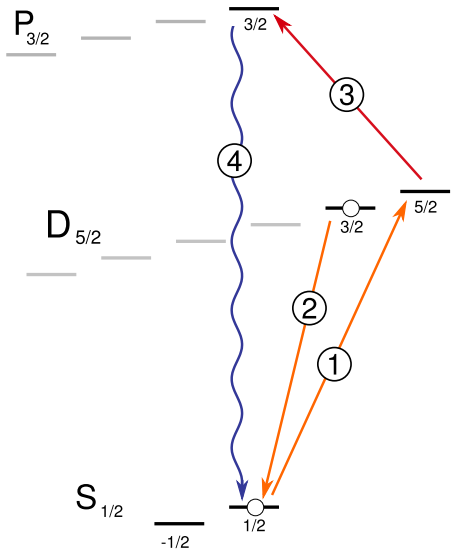

Fig. 4.4: Level scheme of $^{40}Ca^{+}$ showing the recombination process that is used to trace out the internal state of the ion. Only relevant levels are drawn. The qubit levels, $|S_{1/2}, m = 1/2\rangle$ and $|D_{5/2}, m = 3/2\rangle$, are indicated by circles and the magnetic number m is used to label the sublevels. The first pulse with the quadrupole laser transfers all population in the lower qubit state to the auxiliary state $|D_{5/2}, m = 5/2\rangle$. A second laser pulse then takes the population from the upper qubit level to the lower one. The third step is a short pulse at 854 nm that excites the population in the auxiliary state to $|P_{3/2}, m = 3/2\rangle$, from which it decays to the lower qubit level, completing the process.

With a finite number of measurements the expectation values of $\langle \cos(k\hat{x}) \rangle$ and $\langle \sin(k\hat{x}) \rangle$ can only be determined for a number of k values and the measured expectation values are also limited by errors—mostly by the finite number of measurements (see Sec. 6.2). A direct Fourier transformation of the measured data may result in negative and thereby unphysical components of the probability distribution. Instead, we apply a constraint least-squares fit based on convex optimization [76].

In order to use this technique, the problem has to be cast in a function F that can be minimized by the algorithm. In our case, we discretize the position space by using a suitable set of points x_i and search among the probability distributions with $p(x_i) \geq 0$ for all x_i the distribution that minimizes

$$F = \sum_k \left(\sum_i p(x_i) \cos(k x_i) - C_k \right)^2 + \sum_k \left(\sum_i p(x_i) \sin(k x_i) - S_k \right)^2 \qquad (4.22)$$

where C_k and S_k are the experimentally determined estimates of $\langle \cos(k\hat{x}) \rangle$ and $\langle \sin(k\hat{x}) \rangle$, respectively.

Another experimental limitation is that the observable given in Eq. (4.21) is only valid within the Lamb-Dicke approximation. For states with high phonon numbers, the coupling strength of the sideband is modified which not only affects creation of these states but also their analysis. Again, convex optimization is used to account for this effect, as it allows us to include higher orders of the Lamb-Dicke parameter η.

If we take resonant terms up to third order into account, the Hamiltonian H_{disp} becomes

$$H_{\text{disp}} = \hbar\eta\Omega\sigma_x \otimes \left[\left(a + a^\dagger \right) - \frac{\eta^2}{4} \left(\left(a + a^\dagger \right) \hat{n} + \hat{n} \left(a + a^\dagger \right) + 1 \right) \right] \tag{4.23}$$

where $\hat{n} = a^\dagger a$ is the number operator.

As this Hamiltonian no longer commutes with $\hat{x}$, it is not suited for the reconstruction method. However, by neglecting the kinetic energy in Eq. (4.23) an approximate Hamiltonian can be realized that commutes with $\hat{x}$. From Eq. (2.29) and Eq. (2.33) we have

$$\frac{\hat{p}^2}{2m} + \frac{1}{2} m\omega^2 \hat{x}^2 = \hbar\omega \left(a^\dagger a + \frac{1}{2} \right). \tag{4.24}$$

Since we look at states with high phonon numbers, the $1/2$ term on the right side can be neglected, and as $\hat{p}$ does not commute with $\hat{x}$, we also neglect the kinetic energy term on the left side and get

$$\frac{1}{2} m\omega^2 \hat{x}^2 = \hbar\omega a^\dagger a \tag{4.25}$$

$$\Leftrightarrow \quad \frac{1}{4} \left(a + a^\dagger \right)^2 = a^\dagger a = \hat{n}, \tag{4.26}$$

where $\hat{x} = \left(a + a^\dagger \right) \cdot \sqrt{\hbar / 2m\omega}$ was used in the last step. Using this approximation, the Hamiltonian H_{disp} in Eq. (4.23) becomes

$$H_{\text{disp}} = \hbar\eta\Omega\sigma_x \otimes \left[\left(a + a^\dagger \right) \left(1 - \frac{\eta^2}{8} \left(\left(a + a^\dagger \right)^2 + 1 \right) \right) \right]. \tag{4.27}$$

All reconstructed probability densities presented in this thesis are based on this Hamiltonian.

4.5.1 Accessing single parameters of the wave function

The experimental procedure described above can also be used to extract certain parameters of the wave function without the need to perform the full measurement. From

Eq. (4.21) we have

$$\frac{\mathrm{d}}{\mathrm{d}k}\langle O(k)\rangle|_{t=0} \propto \langle \hat{x}\sigma_y\rangle \qquad \text{and} \tag{4.28}$$

$$\frac{\mathrm{d}^2}{\mathrm{d}^2k}\langle O(k)\rangle|_{t=0} \propto \langle \hat{x}^2\sigma_z\rangle. \tag{4.29}$$

The first expression states that by setting the internal state of the ion to $|+\rangle_y$ and recording the fluorescence for short probe times, the expectation value of the position operator $\langle\hat{x}\rangle$ can be obtained. The measured slope is divided by $2\eta\Omega_p t$ to give $\langle\hat{x}\rangle$ in units of Δ.

With the second expression, it is possible to calculate the spread of the wave packet by simply measuring the curvature of the fluorescence signal for the even Fourier components. The width of the wave packet along x is given by

$$w_x = \sqrt{\langle\hat{x}^2\rangle} \tag{4.30}$$

and is obtained (in units of Δ) by taking the square root of the curvature divided by $2\eta\Omega_p t$.

By setting $\phi_- = \pi/2$, the same procedure can be carried out to measure $\langle\hat{p}\rangle$, $\langle\hat{p}^2\rangle$ and w_p. As it is convenient to express these quantities in units of the ground state size, we define $\Delta_x \equiv \Delta$ and $\Delta_p \equiv \hbar/2\Delta_x$ as the unit for them, where x and p indicate along which axis in phase space the quantity was measured.

5 Experimental setup

The following chapter describes the experimental setup that was used to carry out the experiments presented in this thesis. This setup was built up for the most part by Jan Benhelm and Gerhard Kirchmair and to a large extent has already been presented in their respective theses [77–79].

Here, only the aspects that are needed to understand the experiments presented in chapter 7 to 9 will be restated. One important feature of this setup, its capacity to perform experiments with the isotope ^{43}Ca, was not used in the experiments described and details about this aspect are therefore omitted.

The chapter starts at the core of the setup, the ion trap, and moves outward, describing the various mechanical, optical and electronic components that are needed to operate the experiment.

5.1 Linear Paul trap

The ion trap used for the experiments in this thesis is a linear Paul trap of the standard Innsbruck design [65]. It consists of four blades with one opposing pair driven with radio frequency (RF) while the other pair is grounded. This configuration creates the radial

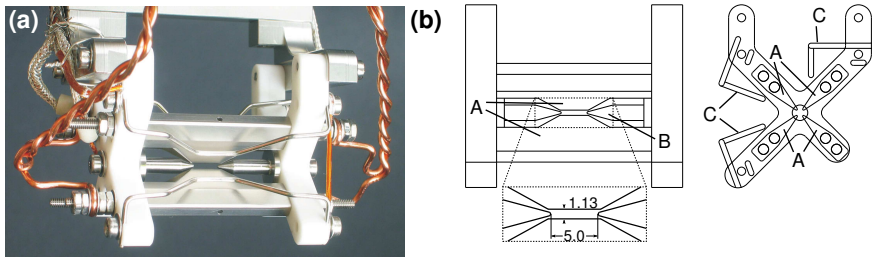

Fig. 5.1: **(a)** Photograph of the trap used in the experiments. **(b)** Schematic drawing of the trap. The distance between the blades (A) and the tips (B) is given in millimeters. Along with the compensation electrodes (C) the tips and the blades are held in place by two pieces of Macor.

confinement. Two tips supplied with a positive DC voltage complete the essential parts of the trap that create a confining three-dimensional potential (see Fig. 5.1).

The blades are operated at about 24.5 MHz created by a signal generator[1]; this signal is amplified[2] to between 8 to 9 W and then coupled into a helical resonator. This amplified RF signal results in a voltage of around 1200 V at the blades, creating a harmonic potential of about 3 MHz in the radial direction. The two radial modes are not perfectly degenerate due to the presence of the tips and error tolerances of the machining process. The splitting of the radial modes was measured to be around 50 kHz.

The tip voltages are typically set to 1000 to 1200 V. This creates an axial potential with trapping frequencies of 1.23 to 1.36 MHz for a single $^{40}Ca^{+}$ ion.

For such settings a linear string of ions will form along the axial direction of the trap, as it has the weakest confinement. The spacing between two ions is around 4 µm.

The ion trap also has two pairs of compensation electrodes positioned between the blades. These electrodes are necessary to cancel stray electric fields that shift the ions' equilibrium position out of the RF null. A mismatch of RF null and DC null due to such stray fields would lead to an increase in amplitude of the ions' motion with the same frequency as the driving frequency. By applying typically -150 V to +150 V to the compensation electrodes, this excess micromotion can be minimized, suppressing unwanted coupling to the micromotional sidebands [80]. With optimal values, the ratio of the coupling strength (measured in Rabi frequency) of the carrier to the first micromotional sideband is on the order of 100:1 for a single ion.

5.2 Vacuum vessel

The trap is situated in a custom-made vacuum chamber consisting of a round main part with eight CF63 connections and two CF200 connections for the top and bottom. A schematic drawing of the setup is shown seen in Fig. 5.2. Three of the eight CF63 connections hold inverted viewports[3], four normal viewports[4], and one connects a six-way cross that holds the ion getter pump, the titanium sublimation pump, the Bayard-Alpert gauge and the valve. The rearport of the six-way cross is also sealed with a normal viewport. The inverted viewports allow objectives be placed close to the ions for a larger solid angle to collect fluorescence light, good imaging resolution and the ability to tightly focus on a single ion within a string of ions.

[1] Rhode & Schwarz SML01
[2] Mini-Circuits LZY-1
[3] UKAEA, fused silica, one sided anti-reflection coating X/UIMCP/43 from Tafelmaier GmbH
[4] Caburn, fused silica, anti-reflection coating X/UIMCP/43 from Tafelmaier GmbH

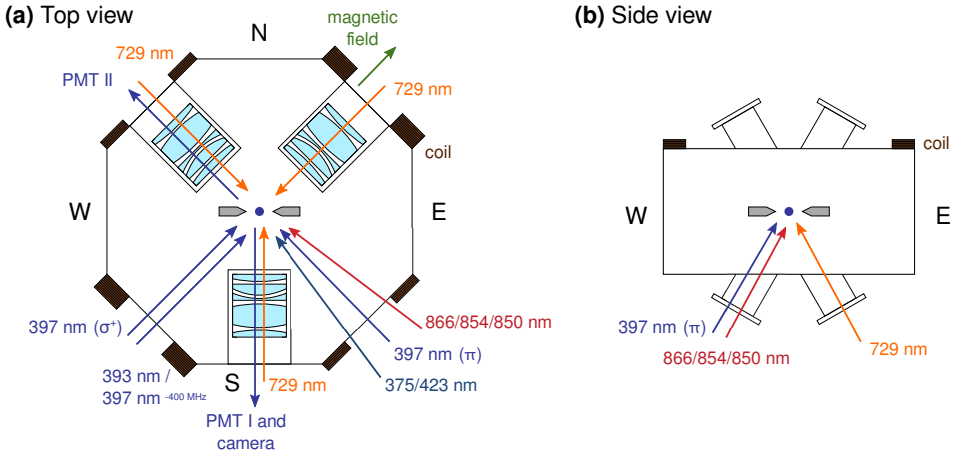

Fig. 5.2: Schematic drawing of the vacuum vessel and optical access. **(a)** Top view showing the orientation of the inverted viewports, the two pairs of magnetic field coils with respect to the trap, and the laser beams used in the equatorial plane. The larger pair of coils (SW-NE) defines the quantization axis, while the second pair is used to compensate external magnetic stray fields. The inverted viewports are shown with the custom-made objectives that each of them holds. **(b)** Side view showing the optical access from beneath the chamber to the ion through viewports that have an angle of 60° with respect to the equatorial plane. The beams for the fluorescence light and (optional) the repump lasers are guided through one bottom viewport. The other bottom viewport is used for another beam for coherent state manipulation that is focused with a normal fiber coupler instead of the custom-made objectives. The picture also shows the fifth magnetic field coil which is also used to compensate stray magnetic fields.

The top and the bottom lid are also custom-made to hold two CF40 viewports each for additional optical access at an angle of 60° relative to the equatorial plane. The bottom lid has additional electrical feedthroughs (CF16) for current to heat the oven, while the top lid possesses two feedthroughs to power the trap and supply voltages to the tips as well as the compensation electrodes.

To ensure a constant low pressure, the ion getter pump runs continuously, and the titanium sublimation pump is fired once a week. The measured pressure is below the range of the Bayard-Alpert gauge ($2 \cdot 10^{-11}$ mbar).

5.3 Magnetic field coils

Five magnetic coils are installed to provide full control of the quantization axis. One pair of coils at the SW and NE port is used to generate the primary magnetic field

that defines the quantization axis, while another pair on the NW and SE port and a large coil mounted to the top CF200 flange are used to compensate external magnetic fields, i.e., the earth's magnetic field (see Fig. 5.2). The pair for the quantization axis, with a separation of 300 mm and an inner diameter of 115 mm, does not constitute a perfect Helmholtz configuration. However, the resulting field gradient was measured to be smaller than 0.2 G/m, which is more than sufficient for our experiments.

All coils are driven by a home-built current stabilizer that has a relative current drift of less than $2 \cdot 10^{-5}$ over 24 hours. The coil pair for the quantization axis is usually operated with 1 A, which corresponds to a magnetic field of about 3.4 G at the location of the ions.

5.4 Optical access

The layout of the vacuum chamber allows for optical access to the ions from ten different directions. In three cases the optical access is through inverted viewports that allow getting closer to the center of the trap. Each inverted viewport holds a custom-made objective[5] consisting of five lenses. These objectives are not only antireflection coated for 397 nm and 729 nm but also correct for the aberrations of the inverted viewport. They are used to collect fluorescence light (see Sec. 6.2) and to focus light tightly at 729 nm onto the ions. A beam waist of 2.6 µm (FWHM) at the position of the ion has been achieved with telescope lenses in front of the objective to widen the incident beam prior to focusing.

This tight focus is used for the beam from the S viewport as it is perpendicular to the ion string and used for single ion addressing. The setup including the detection is shown in Fig. 5.3(a). By careful alignment, a difference in coupling strength between two ions between 10:1 to 15:1 can be achieved. As a consequence an operation on the addressed ion will cause the same operation to be carried out on the neighbouring ion with a much smaller coupling. This unwanted effect is usually refered to as *addressing error*. If used for an AC-Stark pulse (z-rotation) the addressing error is cubed and hence between 1 and 0.4%.

The beam coming from the NE viewport is focused to about 20 µm. This provides a decent compromise between intensity on one hand and stability and equal illumination of all ions on the other. In addition, the beam is σ^+-polarized for maximum coupling of the $S_{1/2}, m = 1/2$ to $D_{5/2}, m = 3/2$ transition.

Beams going through normal viewports are focused directly with fiber couplers onto

[5] Sill Optics GmbH

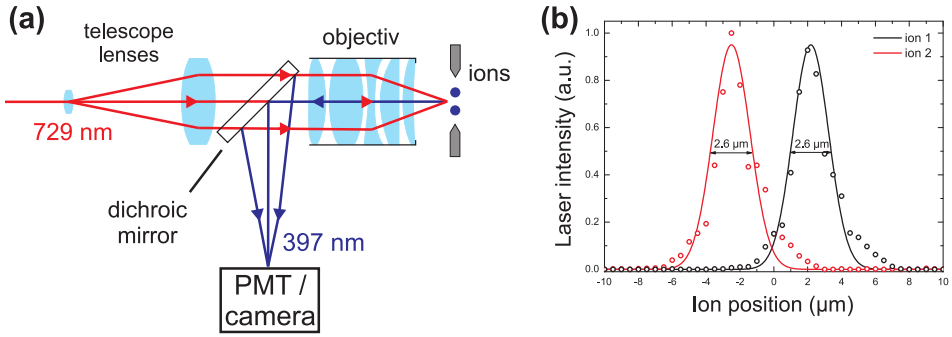

Fig. 5.3: **(a)** Schematic setup for the single ion addressing. The custom-made objective corrects for the aberrations of the inverted viewport and is antireflection coated for 397 nm and 729 nm. A telescope in front widens the beam before it gets focused down by the objective. A dichroic mirror placed between the two reflects fluorescence light from the ions to the camera and PMT. **(b)** Scan of two ions moving across the addressed beam. The intensity was set to perform a 3π rotation when centered on the ion. The laser intensity was calculated using the recorded excitation. From this scan the width of the beam as well as the addressing error can be deduced. Figure taken from Ref. [79].

the ions. These foci have a typical beam waist of 100 to 200 µm,which ensures stability and equal illumination of all ions. The same beam waist is set for the beam with light at 729 nm incident from the bottom, which is used for tasks that do not need high intensities but stability. All other beams are used to drive dipole transitions, for which intensity stability is not as critical.

The beam for optical pumping with σ^+-polarized light at 397 nm is sent along the magnetic field axis from the SW direction. The light at 397 nm and from all three infrared lasers (850 nm, 854 nm and 866 nm) is sent to the ions via the W bottom viewport.

The fluorescence light from the ion is collected with an electron-multiplying charge coupled device (EMCCD) camera[6]and/or a photomultiplier tube (PMT)[7] that collect light from the custom-made objective in the inverted viewport at S. A second PMT uses the NW viewport. As the photoionization beam is incident from the opposing direction (SE) the second PMT is mechanically blocked during loading to avoid damage.

[6] Andor iXon DV885JCs-VP, 8 × 8 µm pixel size, quantum efficiency at 397 nm 37%
[7] electron tubes, P25C, quantum efficiency 28% at 400 nm

5.5 Laser system

One advantage of calcium ions is that all necessary transitions for the use in QIP can be driven with commercially available lasers. In our experiment all dipole transitions are driven by Toptica diode lasers. In case of the lasers for the $S_{1/2} \rightarrow P_{1/2}$ (397 nm) and the $S_{1/2} \rightarrow P_{3/2}$ (393 nm), transitions the light is generated by laser diodes at 794 nm and 786 nm respectively and then frequency doubled by a second harmonic generation (SHG) stage. All diode lasers are referenced to medium-finesse cavities ($\mathcal{F} = 300$) using the Pound-Drever-Hall method [81] (for details on the setup see Jan Benhelm's thesis [77]). With this setup, a linewidth of roughly 100 kHz for these lasers is achieved, limited by acoustic vibrations of the cavity mirrors. All lasers are also monitored with a wavelength meter[8].

Due to higher requirements on linewidth and frequency stability, the light at 729 nm is generated by a narrowband titanium-sapphire (Ti:Sa) laser. With a sophisticated locking scheme to a high-finesse cavity, a linewidth below 10 Hz is achieved.

The setup of all laser sources used in our experiment is described in the following sections.

5.5.1 Diode lasers

All laser wavelengths discussed here are also given in Fig. 3.1. The setup is shown in Fig. 5.4.

397 nm This laser excites the ions on the $S_{1/2}$ to $P_{1/2}$ transition. The output power is between 5 and 10 mW and split by a polarizing beam splitter (PBS) into two polarization-maintaining fibers, which are used for the π- and the σ-beam. The π-beam is used for Doppler cooling and state detection and enters the vacuum vessel from a bottom viewport. Before going through the magnetic field coils (NW to SE) the σ-beam is sent through a PBS and a $\lambda/4$ plate to generate the right polarization needed for optical pumping. Both beams are switched by AOMs at 80 MHz.

866 nm During operation of the 397 nm laser, population from the $P_{1/2}$ level can decay to the $D_{3/2}$ level, where it gets trapped. The 866 nm laser is used to transfer any population from $D_{3/2}$ back to $P_{1/2}$. Again, switching is done via an AOM at 80 MHz.

[8] Toptica, HighFiness-Ångstrom WS/7

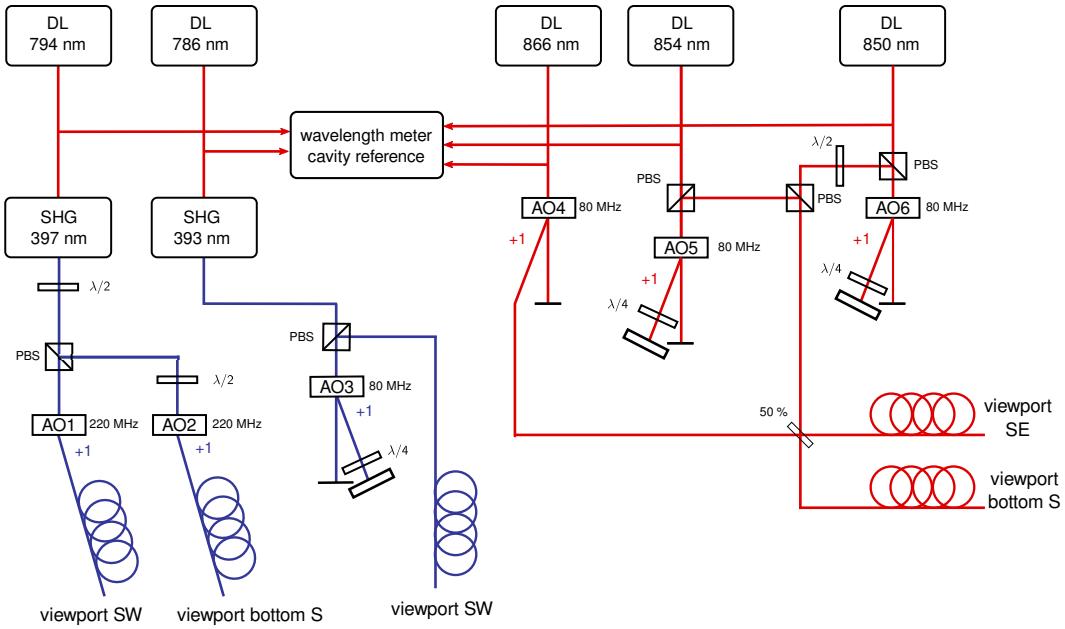

Fig. 5.4: Laser setup of the lasers for the dipole transitions. All lasers are locked to medium finesse cavities and monitored with a wavelength meter. The light at 397 nm is distributed with a PBS and a $\lambda/2$-plate between the weak σ^+ beam which is used for optical pumping and the π-beam used for Doppler cooling and state detection. The repump lasers at 850 nm, 854 nm and 866 nm are overlapped on a 50:50 beamsplitter and coupled into two fibers that enter the vacuum vessel from different directions.

854 nm Light at 854 nm is used to repump populations from the $D_{5/2}$ level to $P_{3/2}$ from which it can decay back to the $S_{1/2}$ ground state. As $D_{5/2}$ is a qubit level, switching is done with an AOM in double-pass configuration to suppress light leakage while the beam is switched off.

850 nm Another repump laser at 850 nm is available to pump population from the $D_{5/2}$ to the $P_{3/2}$ level. This option was needed for the experiment presented in chapter 7 but is not used in any standard operation scheme we employ.

393/397 nm Another frequency-doubled diode laser can be tuned between 393 nm and 397 nm. The light at 393 nm was used in the experiment described in chapter 7 to pump from the $S_{1/2}$ to the $P_{3/2}$ level. For experiments with two ions, this laser was used at a wavelength of 397 nm and red detuned by 400 MHz from the $S_{1/2} \leftrightarrow P_{1/2}$ transition. This allowes for an improved recrystallisation rate after occasional melting of the ion crystal caused by background gas collisions.

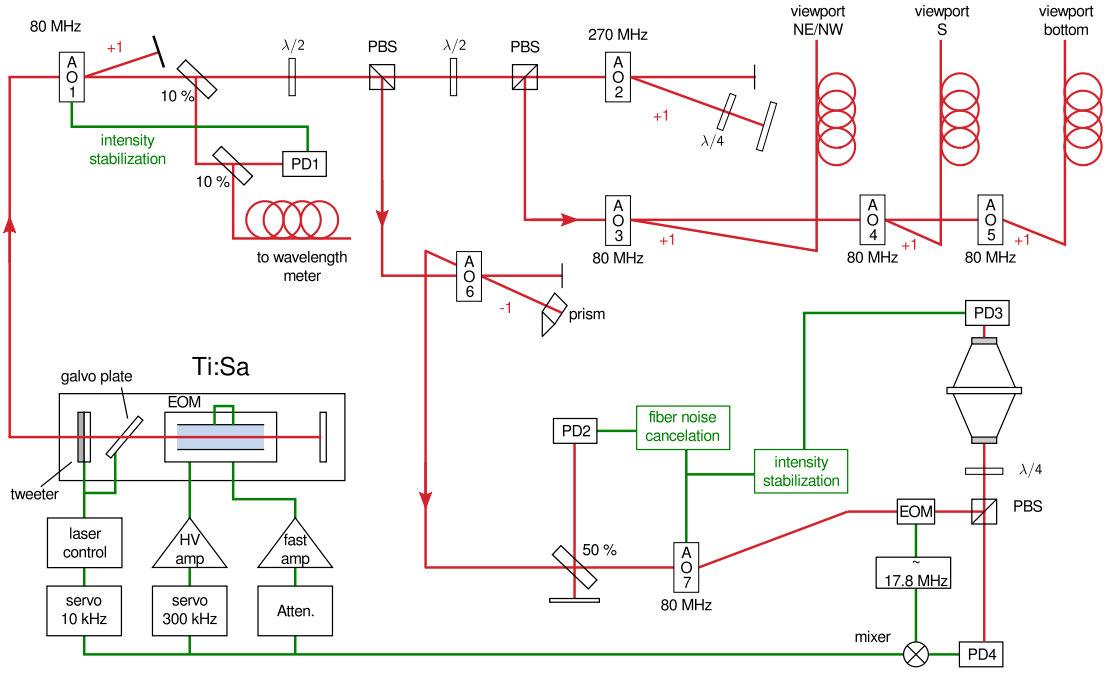

Fig. 5.5: Setup of the Ti:Sa laser at 729 nm. The laser intensity is stabilized via PD1 and AO1. AO2 controls the frequency, intensity and phase of the light that is sent to the ions. AO3 to 5 are used to switch between different fibers that go to different viewports. Another branch of light is sent to the high-finesse cavity for the Pound-Drever-Hall lock. The error signal is fed back to the tweeter and Brewster plate for low frequencies and to an intracavity EOM for mid- and high- frequency feedback.

5.5.2 Ultra-stable laser at 729 nm

The laser at 729 nm is used to coherently couple two states in the $S_{1/2}$ and the $D_{5/2}$ manifold.

In combination with the sideband transitions, this laser can be used for coherent manipulation of the ion's internal and motional state. This allows for several applications such as spectroscopy, sideband cooling, frequency-resolved optical pumping, optical shelving for state detection, state transfer and state initialisation.

Keeping in mind the small linewidth of the quadrupole transition, it is evident that the laser has to fulfill high demands regarding its linewidth, frequency and intensity stability. The setup also has to be capable of switching the frequency by several 100 MHz within a microsecond. The laser's setup and performance are described in Ref. [78]. Here, the optical setup and locking scheme as shown in Fig. 5.5 will be recapitulated.

This laser is locked in the same manner as the diode lasers, that is, using a cavity with the Pound-Drever-Hall method. However, given the requirements a high-finesse cavity is used in combination with a more sophisticated locking scheme.

The vertically mounted cavity[9] ($\mathcal{F}$ = 412,000, linewidth 4.7 kHz, FSR = 2 GHz) is made out of ultra-low-expansion material (ULE). It is mounted on Teflon feet inside a temperature stabilized (±1 mK) vacuum vessel (10^{-8} mbar). The vacuum vessel is placed in a wooden box to shield it from acoustical noise; the box itself is also temperature-stabilized. At the chosen temperature of 30 °C, the cavity's sensitivity to changes in temperature was measured to be 20 MHz/K. The value given here is valid for the cavity that was used in all measurements presented in this thesis. Recently, the cavity has been exchanged with a new one that can be operated at the temperature T_c at which the expansion coefficient is zero to first order. For this new cavity T_c was measured to be 21.2 °C. When the cavity is operated at this temperature, it shows a reduction of more than two orders of magnitude in temperature sensitivity.

The mirrors of the cavity are optically contacted to the spacer and therefore the resonance of the cavity cannot be tuned. The desired output frequency is generated instead by a 1.5 GHz AOM[10] (AO6) in double pass configuration. With a tuning range of 1 GHz, the AOM is capable of covering the free spectral range of the high-finesse cavity, allowing the output frequency to be set at any value. This AOM is also used to cancel the drift of the cavity by comparing the laser frequency to the transition frequency of the ions (see Sec. 6.4) and feeding it back to the AOM.

The sidebands for the locking signal are generated by an EOM[11] operating at 17.8 MHz. The error signal is detected by a photodiode (PD4) and fed back to the laser. The servo loop consist of three branches in order to correct fluctuations on different time-scales.

Slow fluctuations are compensated by feeding the error signal through a PI-servo that controls the tweeter, which consists of a piezo that moves one of the laser cavity mirrors and the scanning Brewster plate. The bandwidth of this branch is limited to 10 kHz by the mechanical resonance frequency of the piezo. Faster fluctuations are addressed by inserting an EOM into the laser cavity. A change in the refractive index of the EOM allows the effective length of the cavity to be changed with a very high bandwidth. This is done with the other two branches of the servo loop. One electrode of the EOM is connected to a fast proportional amplifier[12]. The other electrode of the EOM is connected to a high-voltage amplifier that is controlled by another PI-servo. Since the

[9] Advanced Thin Films, CO, USA
[10] Brimrose GPF-1500-1000
[11] Linos/Gsänger, PM25
[12] Femto HVA-10M-60-F

two grounds of the amplifiers are connected, the EOM is floating. This configuration achieves servo bandwidth of 300 kHz for the high-voltage part and 1.6 MHz for the fast amplifier.

The light from the laser to the cavity is directed via a polarization-maintaining single-mode fiber. To prevent frequency broadening caused by acoustic noise, active noise cancellation was installed [78, 82]. The light from the laser first impinges on a 50:50 beam splitter; one beam splitter output path is directly coupled into an AOM (AO7) while the other arm is retroreflected by a mirror. Opposite to the mirror is a photodiode (PD2) where the incoming light is overlapped with the light that gets reflected back from the fiber's end facet at the cavity. For this purpose, the facet of the fiber is perpendicular to the light direction, causing 4% of the light to be reflected back through the fiber. Since the AOM operates at 80 MHz, this causes a beat note at 160 MHz on the photodiode containing the phase fluctuation of the light caused by acoustic noise in the fiber. The error signal is generated from a stable reference frequency. The phase of the beat signal is kept constant by a phase-locked loop using the voltage-controlled oscillator that drives the AOM.

Additionally, the AOM is used for intensity stabilization. The intensity is monitored by a photodiode (PD3) that monitors at the transmission of the cavity. This intensity stabilization improves the frequency stability of the cavity further.

The resulting linewidth of the laser light was measured in comparison with a similar laser located at another laboratory via a 500 m fiber. The fiber has fiber-noise cancellation implemented as well, and the measured FWHM linewidth was 1.8 Hz [55, 83] for 4 s acquisition time. Assuming the same spectrum for both lasers, the resulting linewidth for each laser is 0.9 Hz.

The output of the laser intensity is stabilized with a photodiode (PD1) and an acousto-optic modulator (AO1). A second AOM (AO2) operated at 270 MHz is used to control the frequency, intensity and phase of the light sent to the ions. A switching network of AOMs (AO3-5) then directs the light to the various viewports. Optionally, AO3 can be driven with two frequencies simultaneously to create the bichromatic light field described in Sec. 4.4. As the two beams differ in frequency by twice the trap frequency, the resulting deviation in the diffraction is very small (0.025°) and allows both beams to be coupled into one fiber with sufficient intensity.

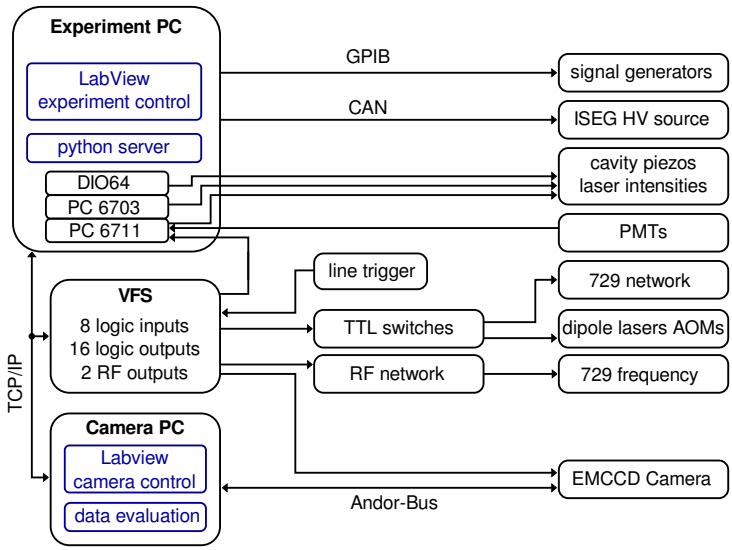

Fig. 5.6: Overview how the various hardware components controlling the experiment are connected. The experiment PC controls the VFS via a python server as well as the second computer that controls the camera and additionally performs automated data evaluation.

5.6 Computer control and radio frequency generation

All electronic aspects of the experiments are controlled by a computer. Almost all devices used in the experiment are managed by a software program written in LabView[13].

The experiment PC is equipped with three data acquisition cards. One fast counter input card[14] is used for readout the PMT data and for analog output together with a second card[15]. The second and the third card[16] are also used for analog and digital outputs. However, all output channels are only used for the controls that do not have to be switched during an experiment run, e.g., the frequencies or intensities of the dipole lasers.

For these switching tasks, a versatile frequencies source (VFS) was developed [72, 84] as experiments with trapped ions require switching and modulation of light fields on short time scales. In our experiment, the switching is achieved with AOMs that offer switching times in the range of microseconds with the ability of frequency tuning and amplitude modulation. This level of control is sufficient for the repump and fluorescence

[13] graphical programming language by National Instruments
[14] National Instruments, PCI 6711
[15] National Instruments, PCI 6703
[16] United Electronic Industries, DIO 64

lasers. In the case of the 729 nm laser, for the quadrupole transition, phase coherence of the frequencies is also needed.

The design of the VFS is based on a field-programmable gate array (FPGA) that controls a direct digital synthesis (DDS) board. This device can phase-coherently switch between up to 16 different frequencies. For experiments with ions, these frequencies are usually used for laser pulses of typically a few microseconds to several milliseconds. The frequency range is between 0 and 300 MHz, with a frequency resolution of 0.1 Hz. To allow for pulse shaping, the amplitude of the radio frequency is varied by a variable-gain amplifier that is also controlled by the FPGA. In addition, the VFS has 16 transistor transistor logic (TTL) channels that can switch with a time resolution of 10 ns.

The VFS is controlled via a server program written in python[17]. This server runs on the experiment control PC and programs the VFS through a TCP/IP connection before each experimental run. A trigger signal from the experiment PC starts the experimental run, which can be synchronized to the AC power line's phase.

A second PC with a PCI card connected to the EMCCD camera is also controlled by the experiment PC via TCP/IP and triggered with the VFS. The software to manage the communication and the camera settings is also written in LabView.

The high voltage source[18] for the tips is also controlled by the experiment PC with software supplied by the manufacturer. The signal generators are controlled by a GPI-Bus[19].

All signal generators as well as the VFS are referenced to a 10 MHz GPS-assisted quartz oscillator[20].

The data that the PMT and the camera measure are evaluated on-line and written to a network drive. Usually the recorded data is analyzed with a versatile evaluation tool. This tool is written in Ruby[21] and uses gnuplot[22] to perform simple data fitting and parameter extraction as well as automatic documentation in the form of html files. In combination with the ability of the experiment control software to process simple scripts, several standard tasks can be automated.

[17] high level programming language, www.python.org
[18] ISEG, EHQ F020p
[19] IEEE-488
[20] Menlo Systems GPS 6-12
[21] high level programming language, www.ruby-lang.org
[22] plotting tool, www.gnuplot.info

6 Experimental techniques

This chapter explains experimental procedures that are commonly used in our experiments. It covers the loading of ions and a description of a normal experimental sequence. This section is followed by a section about quantum state detection using the recorded fluorescence light of the ions. Also described is the process of referencing the 729 nm laser to the ions, which is essential in order to perform coherent operations with high fidelity.

6.1 Loading ions by photoionization

The elemental step of loading ions into the trap is done via a two-stage photoionization process. An oven is used to send a flux of neutral calcium atoms through the trap, where they are hit by the photoionization beam, become charged and hence are confined by the trap's electric potential.

The oven consists of a 8-cm-long steel tube with a 2-mm diameter that is aimed at the center of the trap. Only the lower part of the tube, where the calcium is stored, is heated electrically, while the rest of the tube is designed to collimate the beam in order to avoid excessive contamination of the trap.

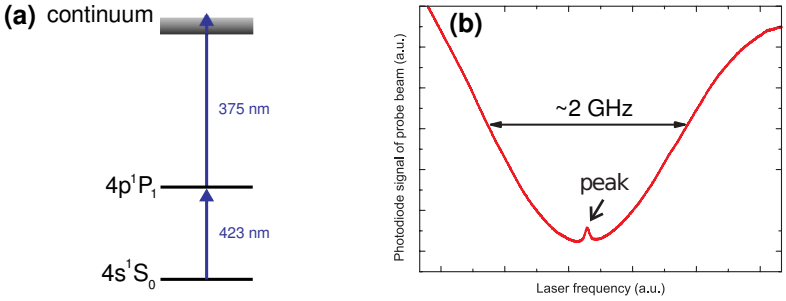

Fig. 6.1: **(a)** Two-step photoionization of calcium. **(b)** Scan of the saturation spectroscopy cell. The small peak in the middle corresponds to the Doppler-free resonance of the $4s^1S_0$ to $4p^1P_1$ transition [77].

The two light fields necessary to ionize calcium are 423 nm and a second laser with a wavelength below 389 nm (see Fig. 6.1(a)). The first laser resonantly excites the $4s^1S_0$ state to $4p^1P_1$ transition. The wavelength of this laser is checked with the wavemeter and by saturation spectroscopy on a calcium vapor cell. The laser is set to sweep continuously around the Doppler-free resonance peak. A spectroscopy scan of the cell is shown in Fig. 6.1(b).

The second laser is a free-running diode laser at 375 nm. Both beams are overlapped on a beam cube and coupled into a single-mode fiber leading to the SE viewport of the experiment. Typically 50 to 100 µW for the laser at 423 nm and 500 µW for the laser at 375 nm are used.

By setting the oven to a temperature of about 300 °C, loading rates of one to two ions every minute are typically observed. The number of ions loaded is checked with the PMT and the camera, and the loading process is stopped once the desired number of ions is in the trap. Since we cannot remove individual ions from the trap, all ions have to be ejected if too many ions are loaded. In this case, the loading starts again.

One side effect of loading in our setup is heating and a resulting expansion of the trap. This slightly shifts the trapping frequencies, which is a problem for experiments that make use of motional sidebands. For these experiments, the trapping frequencies are usually monitored after loading and data acquisition is only started if the frequencies no longer drift. This waiting interval can last up to 15 minutes.

6.2 Quantum state detection

The fluorescence light for state detection at 397 nm is collected by the custom-made objective introduced in the previous chapter. The inverted viewport allows us to get close to the ions. With a distance from the first lens to the ions of $r = 58$ mm and a diameter of $d = 38$ mm, the solid angle covered by the objective is

$$\frac{\mathrm{d}\Omega}{4\pi} = \frac{1}{2}\left(\sqrt{1 - \frac{1}{1 + \left(\frac{2r}{d}\right)^2}}\right) \approx \frac{1}{40}. \tag{6.1}$$

Additional losses in detection efficiency are caused by absorption of the objective of about 4 % and a narrow band-width filter[1] of about 6 %, which is needed to suppress all light outside the wavelength range from 393 nm to 397 nm.

In the current setup two of the three inverted viewports are used to collect fluorescence light: At the NW port the light is directed to a PMT and at the S port a dichroic mirror

[1] Semrock FF01-390/18-25 or FF01-377/50-23.7-D

is used to direct the light to an optical switching box that allows directing all light to another PMT, 90% to the PMT and the rest to the EMCCD camera or all to the camera by sliding either no mirror, a 90:10 beamsplitter or a fully reflective mirror in the beam path.

Both detection setups are placed in the imaging plane, 1.5 m after the objective. This configuration results in a magnification of 24.5. Additionally, a variable slit aperture[2] is installed before both setups to suppress stray light.

6.2.1 Quantum state detection with a PMT

For state discrimination of a single ion with the PMT, the lasers at 397 nm and 866 nm are switched on, typically for 3 to 5 ms (see Fig. 6.2(a)). Fluorescence is detected if the ion is in either the $S_{1/2}$ or the $D_{3/2}$ state. If the ion is in the $D_{5/2}$ level, only background light is detected.

During this time period, a certain number of counts is recorded by the counter attached to the PMT. A histogram of those counts is depicted in Fig. 6.2(b) and clearly shows the two Poissonian peaks that can be associated with the 'bright' and the 'dark' state of the ion. A logarithmic scale was chosen as it more clearly shows the small tail acquired by the dark peak. This tail is caused by the finite lifetime of the metastable $D_{5/2}$ state, as a small fraction of the state decays during the state detection period.

There are various ways of evaluating the measured count rates of the PMT, and the three different methods we employed in the experiment are as follows:

Threshold This method is used in most of our experiments, as it is straight forward to implement. A threshold is set, and we assign the $D_{5/2}$ state ('dark') if the count number is below it and the $S_{1/2}$ state ('bright') if it is above. As an example, in Fig. 6.2 (b) the threshold would be around 35 counts. This scheme can be directly expanded to multiple ions by just setting the same number of thresholds as ions. Naturally the overlap of the peaks increases for more ions, if the detection time is kept constant.

Maximum likelihood The probability of observing the detected number of photon counts for each state is computed by fitting a suitable function to the PMT histogram. These probabilities are multiplied with each other to obtain an overall probability Π. The probability determined by the maximum likelihood estimate then corresponds to the probability of being in the quantum state that maximizes the

[2] Owis, Spalt 40

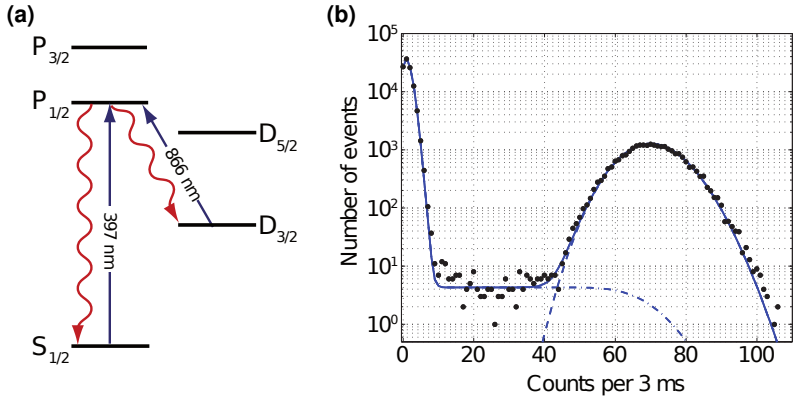

Fig. 6.2: Quantum state detection in Ca^+. **(a)** The ion is excited by laser light on the $S_{1/2} \leftrightarrow P_{1/2}$ and $D_{3/2} \leftrightarrow P_{1/2}$ transitions for a few milliseconds. **(b)** Photon count distribution constructed from 10^5 experiments. In the bright state to the right, the ion scatters on average 70 photons detected by the photomultiplier within the detection time of 3 ms. In the dark state to the left, on average 1.4 background photons are detected due to scattering of laser light from the trap electrodes. The lines drawn in the plot show a fit, from which the probability for the state can be inferred given a certain number of counts. The data presented show a probability of 0.803(1) for the ion to be in the $D_{5/2}$ state. Figure taken from Ref. [61].

probability Π. This method was used in Ref. [61] to post-process measured data but was never implemented for on-line evaluation during measurements.

Bayesian detection scheme The third method tested in our setup is based on Bayes' theorem. In this scheme, the detection time is binned and a probability assigned to the possible states for each count number [85]. By accounting for the possible decay of the meta-stable state, this method does not produce larger errors for longer detection times. The state is then again chosen by maximum likelihood. While this approach offers slightly lower error rates, it comes with a significant technological overhead, i.e., amount of data stored per measurement. The other advantage of this method is a detection time that is *on average* shorter. However, this advantage requires a dynamic stop of the state detection in order to be beneficial. Given the fact that all measurement sequences were carried out using a line trigger at 50 Hz, the overhead of this method did not justify its implementation.

As already mentioned, the state detection process has several marginal error sources: As the photon counts follow a Poisson distribution, there is always a finite overlap between both states. Another error source is the spontaneous decay of the $D_{5/2}$ level.

With typical count rates and detection time, the overall detection error for a single ion is in the range of 0.2%. The methods presented differ in how they handle these imperfections. With this low read-out infidelity in our experiments, the statistical error in the determination of the state (*quantum projection noise*) is the dominant error source for a typical measurement of 100 repetitions per data point.

It should also be pointed out that in the case of multiple ions, the PMT is not able to determine which ion is in the $D_{5/2}$ state but only how many.

6.2.2 Quantum state detection with an EMCCD camera

The other device in our setup to detect the quantum state of the ions is an EMCCD camera. While it has more technological overhead compared to the PMT, it offers the significant advantage that it can read out the quantum state of each individual ion as it also resolves the ions spatially.

The camera is placed in the focal plane of the imaging system such that the ions are imaged on the chip with the ion string's axis parallel with the orientation of the pixels. The ions' image is placed in the center of the chip and a region of interest (ROI) is defined. This area is usually 6×40 pixel wide and thus considerably smaller than the entire 1024×1024 pixel chip.

The current procedure for state discrimination with the camera is carried out using the following steps. For a reference measurement two pictures are taken: one with all ions fluorescing, and a background picture with the laser at 866 nm switched off. The pictures are subtracted from one another and all pixels are summed up perpendicular to the ion string. Next, a Gaussian is fitted to each peak. These peaks are used to construct all 2^N possible states, where N is the number of ions in the trap.

During data recording, the picture is taken and the background again subtracted, before the pixels are summed up. The data obtained are then compared to each of the constructed states and the one with the least square sum deviation is selected. With a detection time of 5 ms for a single ion this method achieves infidelities smaller than 1%.

Inspired by the Bayesian detection scheme for the PMT, we investigated its possibilities for the camera. Here, instead of the temporal information the spatial information is used to obtain a maximum likelihood for the measured quantum state [86].

A probability is assigned to each pixel for each state and for a given count number detected by that pixel. After multiplying all probabilities for each state over all pixels, the state with the biggest probability is selected.

Even from this general description, it becomes apparent that calibration is a crucial step in this scheme. It is necessary to gather enough statistics for each possible state to

produce a meaningful probability table for each pixel. As the number of states grows with 2^N taking reference pictures for eight or more ions will become very time consuming. The number of reference pictures needed could be reduced by grouping pictures, such that all pictures are used that have the same state for the ion in question and its nearest neighbor. This is justified since cross-talk spanning more than one ion position is negligible with the usual magnification and imaging quality [77].

Another aspect of this scheme is the creation of the desired states for the reference pictures. Infidelities for state creation are usually higher than for the targeted read-out. In Ref. [86], this was solved by performing a global $\pi/2$-pulse on all ions and sandwiching the reference picture between two pictures with longer exposure times. Reference pictures are discarded, where the two other detection steps disagree.

As this procedure was technically not possible for our setup, we took a slightly different approach. The reference pictures were also taken by imaging ions after a $\pi/2$-pulse. Afterwards they were processed using the "k-means" data clustering algorithm [87]. Using this procedure we could demonstrate a read-out infidelity of about 0.1% for two ions under normal experimental conditions using a detection time of only 2 ms. For shorter detection times, the clustering algorithm failed to produce reliable probability tables.

Despite its superiority compared to the current evaluation method, this method has not yet been implemented due to its high demands on computational power. This should change once the camera control setup currently running with LabView and Matlab is exchanged with a program written in C++.

6.3 Experimental sequence

All experiments are conducted using a pulsed mode of operation. Here, a typical sequence used to acquire data is listed step by step. Before going into pulsed mode certain parameters must first be set properly. Especially the settings for the Doppler cooling beam have to be set with care. The 397 nm laser is slightly red-detuned from the $S_{1/2} \rightarrow P_{1/2}$ resonance by half a linewidth and the power is set to be half the saturation intensity [66]. The beam of the 397 nm laser overlaps with all modes cooling all of them.

The 866 nm laser has to be set as well since it is used in combination with the 397 nm laser to avoid trapping populations in the $D_{3/2}$ level. The frequency is set to give almost maximum fluorescence with a slight blue detuning to avoid coherent population trapping. The intensity is set just below saturation.

(1) Doppler cooling At this stage, the lasers at 397 nm and 866 nm are switched on for

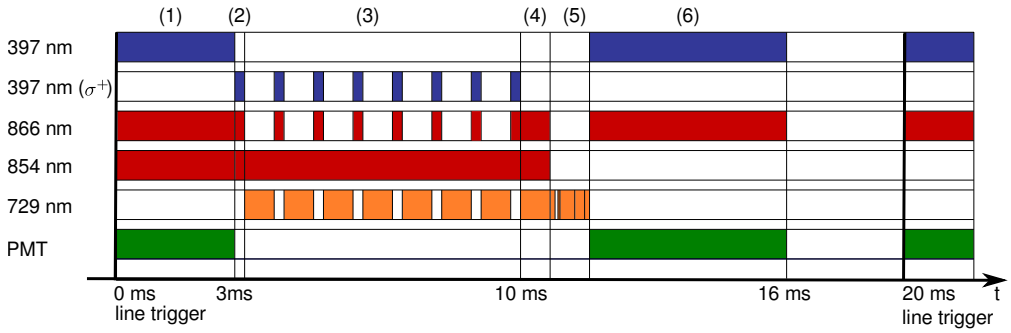

Fig. 6.3: Graphic representation showing when the lasers are used during the execution of a typical sequence. Triggered by the line cycle at 50 Hz, the sequence consists of (1) Doppler cooling, (2) optical pumping, (3) sideband cooling, (4) frequency-resolved optical pumping, (5) quantum-state manipulation and (6) state discrimination. As a typical sequence is shorter than 20 ms, the experiment is idle until the next line trigger.

typically 3 ms with the settings described above. During the same time, the PMT is switched on to check if the ions are still crystallized. If the fluorescence rate is below a certain threshold, the data point is discarded and the same experiment executed again. Various measurements of the ions motional state after this step yielded an average phonon number between 15 and 20.

(2) Optical pumping A weak pulse for 80 µs at 397 nm with σ^+ polarization combined with the 866 nm laser transfers 99% of the population to the $S_{1/2}, m_j = 1/2$ state.

(3) Sideband cooling This step is used to cool the ions to the motional ground state. The laser at 729 nm is set to the red sideband of the stretched state $S_{1/2}, m_j = 1/2 \rightarrow D_{5/2}, m_j = 5/2$. A successful transfer reduces the mean phonon number by one. The laser at 854 nm is also switched on all the time to transfer the population in $D_{5/2}$ to $P_{3/2}$ from which it can decay back to $S_{1/2}$. The other decay channel from $P_{3/2}$ to $D_{3/2}$ is prevented from trapping population in $D_{3/2}$ by also switching on the laser at 866 nm. As this procedure does not guarantee a decay back to $S_{1/2}, m_j = 1/2$, several pulses with the 397 laser with σ^+ polarization are used to avoid leaking into $S_{1/2}, m_j = -1/2$. This step typically takes 7 ms and reaches a mean phonon number of $\langle n \rangle = 0.05(5)$.

(4) Frequency resolved optical pumping The 729 nm laser is then used to increase the optical pumping efficiency further. By coupling the $S_{1/2}, m_j = -1/2$ level to $D_{5/2}, m_j = 3/2$, the undesired Zeeman state is depleted. Again, both repump

lasers at 866 nm and 854 nm are switched on. This step is usually performed for 500 µs and reaches an efficiency of more than 99.8% for a single ion.

(5) Quantum state manipulation After the ions are cooled to the ground state and initialized in the lower qubit state, the protocol for the specific experiment in question is run. Most of the time, only the quadrupole laser for coherent manipulation of the ion is used during this step. However, this part of the sequence can also include pulses with lasers acting on dipole transitions.

(6) State discrimination The outcome of the experiment is measured by switching on the lasers at 397 nm and 866 nm. The intensity of the former is increased to get a high fluorescence rate, allowing state discrimination within a few milliseconds. The PMT is used to determine, how many ions are in the $D_{5/2}$ level as this is usually sufficient for experiments with few ions. If it is necessary to know the quantum state of each individual ion, the camera is used instead, which requires slightly longer detection times and more technical overhead.

One sequence is usually run between 50 and 200 times to ensure enough statistical significance, and depending on the tolerable quantum projection noise of that data set.

6.4 Referencing the 729 nm laser to the ions

Given the narrow linewidth of the $S_{1/2} \leftrightarrow D_{5/2}$ transition and the correspondingly narrow linewidth of the laser at 729 nm used to drive it, a precise knowledge of the actual transition frequency is mandatory in order to carry out high-fidelity operations. These transition frequencies between the two manifolds are set by the external magnetic field, and the frequency of the laser is determined by the reference cavity. Both frequencies are determined by measuring two of the transitions that depend differently on the magnetic field. This measurement is done in the following way:

After Doppler cooling and optical pumping, the ions are initialized. Next, a Ramsey experiment is carried out. To this end, a $\pi/2$ pulse on the probed transition creates a superposition, followed by a waiting time τ_R, followed by another $\pi/2$ pulse. While the applied pulse has a phase of $\phi_1 = \pi/2$ in the first measurement, it is set to $\phi_2 = 3\pi/2$ for a second pulse.

The pulse sequence is finished by state discrimination, and the entire procedure is usually repeated 100 times for both phase settings. The extracted excitation probabilities p_{ϕ_1} and p_{ϕ_2} can then be used to infer the frequency difference between the laser and the

probed transition:

$$\Delta\nu/(2\pi) = \frac{1}{2\pi\,(\tau_R + 2\tau_\pi/\pi)\arcsin\frac{p_{\phi_1}-p_{\phi_2}}{p_{\phi_1}+p_{\phi_2}}}. \tag{6.2}$$

Here, τ_π denotes the length of the $\pi/2$-pulse. Typical values for τ_R are between 100 and 250 µs, while τ_π is between 10 and 15 times shorter.

Once two transitions have been measured, the difference in the two measurements is used to determine the magnetic field. With that knowledge, the transition frequency at zero magnetic field is deduced to serve as a reference for all transitions.

The entire procedure is fully automated and usually runs every minute. The measurements are recorded over time and a polynomial fit is applied to the data. For the cavity-drift a first order linear fit is used most of the time to extrapolate the cavity drift and feed it back to the AOM (AO6 in Fig. 5.5) between the cavity and the laser.

With this feedback scheme in place, the frequency of the laser is kept close to the transition frequency, deviating by less than 200 Hz (rms-deviation).

The magnetic field is set by the magnetic field coils and should not change. In addition to the small fluctuations ($\approx$ 50 µG) that one expects from a lab environment with various electric devices, the magnetic fields exhibits certain erratic jumps (100-300 µG) of unknown origin. To account for this behaviour, the fit for the magnetic field is just an average over the previous five minutes, while older data points are discarded.

A more significant change in the magnetic field is caused by the line cycle of 50 Hz [77]. Fortunately, the effect can be greatly reduced by triggering the experiment on the line cycle and running the part of the sequence in which the coherent state manipulation is carried out at the maximum of the line cycle. In this region the magnetic field does not change in first order.

Recently, a magnetic shielding for the new setup was installed. This reduces the magnetic field noise further, resulting in longer coherence times of the ionic qubit [88].

7 Precision measurement of the branching fractions of the 4p $^2P_{3/2}$ decay

In this chapter a precision measurement of the branching fractions of the 4p $^2P_{3/2}$ of Ca II is presented [61]. A novel technique based on a repeated optical pumping scheme is demonstrated, yielding a forty-fold improvement in accuracy compared to the best previous measurement [89].

7.1 Introduction

A precise knowledge of the radiative properties of stellar matter [90] is crucial for matching theoretical models to observations in many domains of astrophysical research [91]. Modelling isotopic abundances or the energy transport by photons in a star or a gas, in turn, requires a precise knowledge of atomic transition frequencies and oscillator strengths based on atomic structure calculations and experiments with a wide variety of neutral atoms and ions. Singly charged calcium ions have been used in various astrophysical observations [92, 93]. In particular, monitoring of emission and absorption lines of dipole transitions between low-lying states has provided information about systems like galaxies [94, 95], interstellar gas clouds [96], gas disks surrounding stars [97, 98], and stars [99].

Theoretical physicists have devoted a considerable effort to improve calculations of matrix elements of transition rates and polarizabilities [100–104] in $^{40}Ca^+$. Singly charged calcium is a quasi-hydrogenic system that constitutes an interesting model system for testing atomic structure calculations of other singly charged alkali-earth ions with higher nuclear charge. An improved knowledge of their atomic structure would also be of interest for parity non-conservation experiments [105] in Ba^+ or Ra^+ that require precise values of transition matrix elements for a determination of the strength of parity-violating interactions. For a comparison of theoretical predictions with experimental observations, theorists often turn to precision measurements of excited state lifetimes [62, 63, 89, 106–108]. Alternatively, precise measurements of branching fractions [109] of the decay of an excited state into lower-lying states could be used.

Measurements of branching ratios or oscillator strengths in ions often date back quite a long time [89] and are usually performed on ensembles of ions in discharges, ion beams [110] or trapped clouds of ions. A notable exception is a recent experiment [111] measuring the branching fractions of the $P_{3/2}$ state decay with a single trapped Ba^+. Single trapped and laser-cooled ions form an attractive system to perform such precision measurements, as state preparation and quantum state detection can be carried out with very high fidelity. In addition, the use of single ions eliminates errors due to depolarizing collisions.

For the precision measurements reported here, a single $^{40}Ca^+$ ion is employed for determining the branching fractions of the decay of the excited state 4p $^2P_{3/2}$ into the states 4s $^2S_{1/2}$, 3d $^2D_{5/2}$ and 3d $^2D_{3/2}$ (see Fig. 3.1). We introduce a novel technique based on repetitive optical pumping to shuffle populations between two of the lower-lying states. The shuffling steps are followed by detection of the population transferred to the third state. This technique surpasses the branching ratio measurement of Gallagher [89] by a factor of forty in precision and provides branching fractions with a precision of better than 1%. In combination with precision measurements of the excited $P_{3/2}$ state lifetime, our measurements lead to a more precise determination of the transition probabilities on the $S_{1/2}$–$P_{3/2}$, $D_{3/2}$-$P_{3/2}$, and $D_{5/2}$-$P_{3/2}$ transitions.

7.2 Measurement method

A partial level scheme of $^{40}Ca^+$ showing its five lowest energy levels is depicted in Fig. 3.1. The $P_{3/2}$ state decays into the three states $S_{1/2}$, $D_{3/2}$, and $D_{5/2}$, the D-states being metastable with a lifetime of about 1.2 s [62, 108]. The branching fractions p_j, i. e. the relative strengths of the decay processes, will be labelled by j, j being the angular momentum quantum number of the state into which the ion decays ($j \in \{\frac{1}{2}, \frac{3}{2}, \frac{5}{2}\}$). By definition, p_j fulfil the normalization condition $p_{1/2} + p_{3/2} + p_{5/2} = 1$. In this situation, a branching ratio is conveniently measured by (i) preparing the ion in one of the lower states, (ii) optically pumping it via the $P_{3/2}$ to the other two states, and (iii) detecting the state populations in these states [111]. This scheme is illustrated by Fig. 7.1(a). An ion, initially in $S_{1/2}$, is prepared in $D_{3/2}$ by optical pumping with light at 397 nm (step 1). Then, the state is completely emptied by a pulse of light at 850 nm exciting the ion to the $P_{3/2}$ state so that the ion decays into either of the states $S_{1/2}$ and $D_{5/2}$ (step 2). Finally, a quantum state measurement reveals the state into which the ion decayed. By repeating this elementary sequence M times and averaging over the measurement

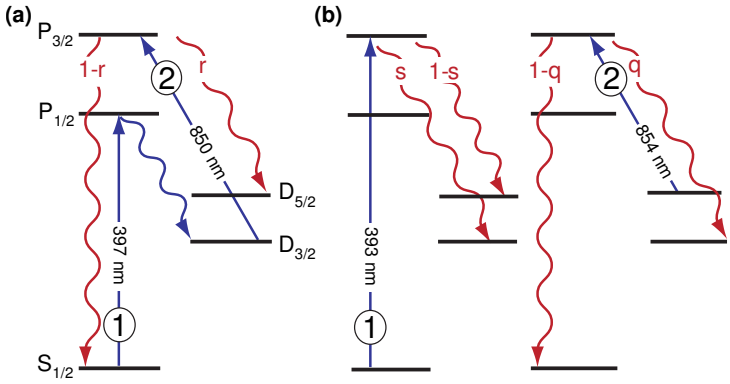

Fig. 7.1: Scheme for measuring the branching fractions of the $P_{3/2}$ state's decay. **(a)** To determine the branching ratio r between decay to the $S_{1/2}$ and $D_{5/2}$ states, we first shelve the population in the $D_{3/2}$ state by a 397 nm laser pulse (step 1). Next we empty the population in this state by a pulse of 850 nm light (step 2). After N of these cycles we measure the population in the $D_{5/2}$ state by fluorescence detection. **(b)** To measure another branching ratio, we first apply a pulse of 393 nm light, to populate the D-manifold via the $P_{3/2}$ state (step 1). Next we perform N cycles consisting of a pulse of 854 nm light to empty the population in the $D_{5/2}$ (step 2), followed again by a pulse of 393 nm light (step 1). Again, after N such cycles, a fluorescence measurements detects the population in the $D_{5/2}$ state. The combination of measurements (a) and (b) provides enough information to unambiguously determine the branching fractions p_j.

outcomes, an estimate $\hat{r}$ of the decay probability into $D_{5/2}$

$$r = p_{5/2}/(p_{1/2} + p_{5/2}) \tag{7.1}$$

is obtained with a statistical error $\sigma_{\hat{r}} = \sqrt{r(1-r)/M}$ set by quantum projection noise. Note that in this measurement the branching fraction $p_{5/2}$ is normalized by the factor $p_{1/2}+p_{5/2}$ to account for the fact that population decaying back into $D_{3/2}$ is immediately pumped back by the 850 nm laser pulse. In $^{40}Ca^+$, earlier experiments [89] had shown that the likelihood of a decay into $D_{5/2}$ was rather small ($r \approx 0.05$). For $r \ll 1$, the accuracy of the measurement is improved by repeating steps 1 and 2 many times before performing the state measurement. In this way, population is shuffled back and forth between $S_{1/2}$ and $D_{3/2}$, with a growing fraction accumulating in $D_{5/2}$. The population in this state after applying N cycles is given by

$$r_N = 1 - (1-r)^N. \tag{7.2}$$

Resolving this equation for r yields an estimate $\hat{r} = 1 - \sqrt[N]{1-\hat{r}_N}$ for the decay probability. A short calculation shows that the uncertainty of $\hat{r}$ can be expressed as

$$\sigma_{\hat{r}}(N) = \frac{1-\hat{r}}{\sqrt{M}N}\sqrt{(1-\hat{r})^{-N}-1}, \tag{7.3}$$

where it was assumed that the measurement of r_N is quantum-limited in precision. Minimization of $\sigma_{\hat{r}}$ as a function of N results in the optimum number of cycles given by

$$N^* = \frac{x^*}{-\log(1-r)}, \tag{7.4}$$

with the constant $x^* \approx 1.594$ minimizing the function $f(x) = \sqrt{e^x - 1}/x$. For the optimum number of measurements N^*, we have $r_N(N^*) = 1 - e^{-x^*} \approx 0.8$ and the measurement uncertainty is reduced compared to the single-cycle experiment by

$$\frac{\sigma_{\hat{r}}(N^*)}{\sigma_{\hat{r}}(N=1)} = -\sqrt{\frac{1-r}{r}}\log(1-r)f(x^*) \approx 1.24\sqrt{r}, \tag{7.5}$$

the approximation being valid in the case $r \ll 1$. For $r = 0.05$, the optimum cycle number is given by $N^* = 31$. The reduction in the number of measurements needed to reach a certain level of precision directly translates into a reduction of overall measurement time as the duration of a single experiment is dominated by the time required for cooling the ion and measuring its quantum state.

A second type of experiment detecting another branching ratio is needed for determining the branching fractions p_j. Towards this end, the scheme shown in Fig. 7.1(b) is employed: An ion in state $S_{1/2}$ is excited to the $P_{3/2}$ state and subsequently decays into states $D_{3/2}$ and $D_{5/2}$ (step 1). Afterwards, measurement of the $D_{5/2}$ state population reveals the probability

$$s = p_{3/2}/(p_{5/2} + p_{3/2}) \tag{7.6}$$

of a decay into $D_{3/2}$.

Again, the measurement accuracy can be increased by shuffling population between the states $S_{1/2}$ and $D_{5/2}$. For this, in a second step, the $D_{5/2}$ state is emptied by light at 854 nm. In this step the probability of decay into $D_{3/2}$ is given by

$$q = p_{3/2}/(p_{1/2} + p_{3/2}). \tag{7.7}$$

Now, the measurement prescription is to perform step 1, followed by N cycles consisting of step 2 and step 1, and to measure the $D_{5/2}$ state population given by

$$s_N = (1-s)\left\{(1-q)(1-s)\right\}^N. \tag{7.8}$$

In combination with the normalization condition $\sum_k p_k = 1$, the two measurements are sufficient for unambiguously determining the branching fractions p_j.

7.3 Setup

For this experiment the ion trap was operated at trapping frequencies of 1.24 and 3 MHz in the axial and radial direction, respectively.

All lasers described in Sec. 5.5 are used for this experiment. The second laser with a second harmonic generation stage is run at 393 nm and used to excite the $S_{1/2}$ to $P_{3/2}$ transition.

The quantum state detection is carried out as described in Sec. 6.2.1. For a detection time of 3-5 ms an average photon count rate of 23 kcounts/s is recorded when the ion is in either of the 'bright' $S_{1/2}$ and $D_{3/2}$ states. If the ion is in the 'dark' $D_{5/2}$ state, an average of 0.5 kcounts/s is detected, caused by scattering of the laser off the trap electrodes. The experiment is repeated M times and the recorded photon counts are evaluated using the maximum likelihood method also described in Sec. 6.2.1.

In order to discriminate between the $S_{1/2}$ and the $D_{3/2}$ state, the $S_{1/2}$ state population is coherently transferred to the $D_{5/2}$ state prior to state detection by a laser exciting the $S_{1/2} \leftrightarrow D_{5/2}$ quadrupole transition. For this, either resonant laser π-pulses or rapid adiabatic passages [75] are used connecting pairs of Zeeman states in the ground and the metastable state. This way, we achieve a transfer probability of better than 99.5%.

7.4 Results

For the experimental determination of the $P_{3/2}$ state's branching fractions, a single ion is loaded into the trap. The first experiment implements the scheme depicted in Fig. 7.1(a). We start by measuring the time it takes to completely empty the $S_{1/2}$ state by light at 397 nm. For this, a laser pulse of variable length is applied to an ion prepared in state $S_{1/2}$, and subsequently the population transferred to the $D_{3/2}$ state is detected by shelving the remaining $S_{1/2}$ state population in the $D_{5/2}$ level. Fitting an exponentially decaying function to the $S_{1/2}$ state population, we find a $1/e$ time of 1 µs. In a similar measurement, we determined the decay time of population in $D_{3/2}$ to be 16 µs when emptying the state by light at 850 nm. In a next step, we implement a population shuffling cycle by switching on the laser at 397 nm for 20 µs before turning on the laser at 850 nm for a duration of 100 µs. We repeat this cycle N times to slowly accumulate all the population in the $D_{5/2}$ state. Fig. 7.2 (a) shows the $D_{5/2}$ state population for cycle numbers ranging from 5 to 200 by repeating the experiment for each value of N between 20000 and 23000 times. The experimental results are fitted by

slightly modifying Eq. (7.2) to

$$r_{N,\mathrm{exp}} = A(1-(1-r)^N) \tag{7.9}$$

by introducing a scaling factor A to account for the fact that even after 200 pumping cycles the measurement finds 0.3% of the population to be outside the $D_{5/2}$ state. This effect is caused by the finite lifetime of the metastable states as will be discussed in Sec. 7.5.2. A similar procedure is applied for implementing the scheme depicted in Fig. 7.1(b). The $1/e$ pumping times for emptying the states $S_{1/2}$ and $D_{5/2}$ by light at 393 nm and 854 nm are determined to be 2 µs each. Based on this measurement, a pumping cycle - transferring population from $D_{5/2}$ to $S_{1/2}$ and back again- was chosen that consisted of a laser pulse at 854 nm of 20 µs duration, followed by another 20 µs pulse at 393 nm. Again, we measure the population remaining in the $D_{5/2}$ state after N pumping cycles, N varying between 0 and 69. Fig. 7.2 (b) shows the experimental results obtained by repeating the experiment 20000 times for each value of N. We fit the results by modifying Eq. (7.8) to

$$s_{N,\mathrm{exp}} = (1-s)\left\{(1-q)(1-s)\right\}^N + B. \tag{7.10}$$

Here, the offset B accounts for 0.03% of the population seemingly remaining in the $D_{5/2}$ state. The error bars appearing in Fig. 7.9 and Fig. 7.10 are of statistical nature due to the finite number N of experiments.

The parameters r, s, q appearing in equations (7.9) and (7.10) can be expressed by $p_{3/2}$ and $p_{5/2}$. To determine the branching fractions p_j, we use a weighted least-square fit to jointly fit both decay curves by the set of parameter $\{p_{3/2}, p_{5/2}, A, B\}$, assuming that the measurement error is given by quantum projection noise. With this procedure, we find $p_{1/2} = 0.9347(3)$, $p_{3/2} = 0.00661(4)$, $p_{5/2} = 0.0587(2)$, and $A = 0.9971(3)$, $B = 0.0013(2)$. The error bars are obtained from a Monte-Carlo bootstrapping technique [112]. We randomly vary the experimentally observed $D_{5/2}$ populations p by shifting their values assuming a Gaussian distribution with variance $p(1-p)/M$ and fit the resulting data set. Repeating this procedure 1000 times, the spread of the simulated fit parameters provides us with an error estimate for the branching fractions.

7.5 Discussion

7.5.1 Statistical errors

In the regression analysis used for determining the branching fractions, we assume the errors to be quantum-noise limited. This means that we consider the outcome of an

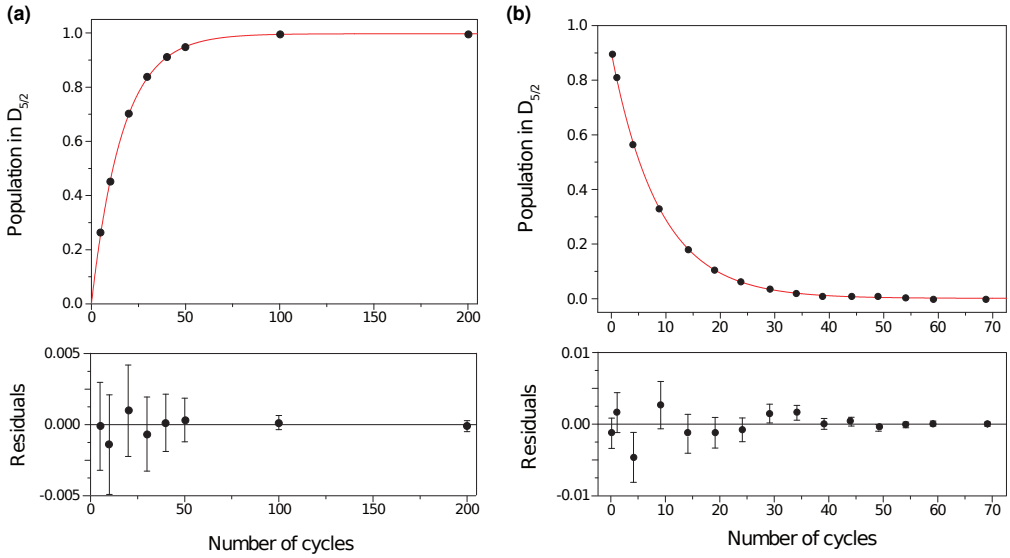

Fig. 7.2: **(a)** Population in the $D_{5/2}$ state as a function of the number of cycles N as depicted in Fig. 7.1(a). Every data point consists of at least 2×10^4 measurements to determine the average population in $D_{5/2}$. The data points are jointly fitted with the measurement results presented in Fig. 7.2(b) to obtain the branching fractions p_j as described in the main text. The fitted curve is given by Eq. (7.9). The lower plot shows the residuals with errors bars given by the statistical uncertainty due to the finite number of measurements. **(b)** Population in the $D_{5/2}$ state as a function of the number of cycles N as depicted in Fig. 7.1(b). The lower plot shows the residuals after fitting the data. The fitted curve is given by Eq. (7.10).

individual experiment to be given by a random variable X_i, $i = 1, \ldots, M$, yielding the outcome '1' with probability p and the outcome '0' with probability $1 - p$. For a set of M experiments, we then assume the standard deviation of $X = \frac{1}{M}\sum_{i=1}^{M} X_i$ to be given by $\sigma_p = \sqrt{p(1-p)/M}$. If, however, due to experimental imperfections the probability p slightly changes over the course of time needed for carrying out the M experiments, this assumption would be violated. We therefore checked the validity of our hypothesis by subdividing our data into K sets S_k, $k = 1, \ldots, K$, each containing M/K consecutively taken experiments described by the random variables $\{X_{j_k+1}, \ldots, X_{j_k+M/K}\}$. For each set S_k, we compute its mean value $p^{(k)} = \frac{K}{M}\sum_{i\in S_k}\langle X_i\rangle$ and its deviation $p^{(k)}$–p from the average probability. We repeat this procedure for different values of K ranging from 2 to 1000. A comparison of the distribution of $p^{(k)}$–p with the one expected for truly random variable all having the same probability p leads us to conclude that the assumption of quantum-limited errors is well-justified.

Tab. 7.1: Branching fractions of the decay of the $P_{3/2}$ state as found in the present work compared to various theoretical values from the literature. Ref. [102] gives the relative decay strengths of the state 4p into 4s and 3d.

Transition	Branching fractions				
	Present work	Ref. [100]	Ref. [101]	Ref. [102]	Ref. [103]
$4P_{3/2} \leftrightarrow 4S_{1/2}$	0.9347(3)	0.9381	0.9354	0.9357	0.9340
$4P_{3/2} \leftrightarrow 3D_{3/2}$	0.00661(4)	0.00628	0.00649	0.0643	0.00667
$4P_{3/2} \leftrightarrow 3D_{5/2}$	0.0587(2)	0.0556	0.0581		0.0593

Tab. 7.2: Einstein coefficients A_{fi} measured from the branching fractions in combination with the lifetime measurement of Ref. [63] and the theoretical prediction of Ref. [103].

Transition	$A_{fi} \times 10^6 s^{-1}$	
	Present work+[63]	Ref. [103]
$4P_{3/2} \leftrightarrow 4S_{1/2}$	135.0(4)	139.7
$4P_{3/2} \leftrightarrow 3D_{3/2}$	0.955(6)	0.997
$4P_{3/2} \leftrightarrow 3D_{5/2}$	8.48(4)	8.877

7.5.2 Systematic errors

The method of measuring the branching fractions by repeated optical pumping assumes that the optical pumping steps are perfect. If, however, a small fraction $\epsilon_{1,2}$ is not pumped out in the two pumping steps of the cycle, the measured decay rates will be smaller than for perfect optical pumping. This systematic effect is taken into account by defining an effective cycle number $N_{\text{eff}} = N(1 - \epsilon_1 - \epsilon_2)$ that replaces the cycle number N in Eqs. (7.9) and (7.10). This correction was actually applied in the data evaluation of the first experiment as it turned out that the laser pulse at 850 nm of 100 µs duration was too short to completely empty the $D_{3/2}$ state ($\epsilon_2 = 0.3\%$ of the population were left behind).

The finite lifetime $\tau_D = 1.2$ s of the metastable D-states also has a small effect on the measured branching ratios. The quantum state detection method we use is not affected by spontaneous decay processes occurring during the detection time. Spontaneous decay during the pumping cycle, however, slightly modifies the results. This is best illustrated by the pumping scheme shown in Fig. 7.1(a). Spontaneous decay of the $D_{3/2}$ state is negligible since the state is emptied by light at 850 nm in 16 µs, i.e. with a rate roughly 10^4 times bigger than the spontaneous decay rate. The situation is different for the $D_{5/2}$

state which is populated by a rate $R_a = r\tau_{\text{cycle}}^{-1}$ where $\tau_{\text{cycle}} = 120\,\mu\text{s}$ is the duration of a single pumping cycle. Here, spontaneous decay gives rise to a steady-state $D_{5/2}$ state population $p_{D,\infty} = 1 - R_a\tau_D \approx 99.8\%$ in the limit of an infinite number of pumping cycles which is consistent with the measured value of the fit multiplier A. In addition to changing the steady state solution, the additional decay process also decreases the time required for reaching the equilibrium (see Eq. (7.9)). This effect was taken into account in the analysis of the branching fractions stated in Tab. 7.1.

A similar argument can be made for spontaneous decay affecting the pumping scheme of Fig. 7.1(b). Here, the $D_{3/2}$ is populated with a rate $R_b \approx s\tau_{\text{cycle}}^{-1}$ which needs to be compared to the spontaneous decay rate $1/\tau_D$. Due to this effect, we expect to find a steady-state population of about 0.04% that is not in $D_{3/2}$. Here, the effect is smaller since $r < s$ and the duration of the pumping cycle was about five time shorter than in the other experiment. The correction to the measured rate is also about 0.04% and does not significantly alter our measurement. Before performing the branching ratio measurements, we had checked that the lifetimes of the metastable states were not significantly shortened by the lasers at 850 and 854 nm which could occur either by a broad-band frequency background of the diode lasers producing the light or by imperfectly switched off laser beams.

In general, any additional mechanism that leads to an exchange of population between the atomic states will modify the steady-state population obtained in the limit of large N and shorten the time scale required for reaching the steady-state. Spin-changing collisions leading to transitions between the $D_{3/2}$ and the $D_{5/2}$ state are of no importance in our measurements as they occur at a rate that is smaller than $10^{-2}s^{-1}$.

7.5.3 Comparison with other measurements and calculations

The branching fractions obtained from fitting the two decay measurement can be compared to previous measurements and theoretical calculations. By evaluating the ratio $p_{3/2}/(p_{1/2} + p_{5/2})$, we find $A_{(P_{3/2}-S_{1/2})}/\sum_J A_{(P_{3/2}-D_J)} = 14.31(5)$ for the branching ratio of the decay into the S- and D-states. This is a bit lower than the value of 17.6(2.0) measured by Gallagher [89] in a discharge experiment in 1967. A comparison with theoretical calculations [100–103] is given in Tab. 7.1, showing a good agreement between experiment and theory.

When combining the branching ratio measurements with an experimental determination [63] of the $P_{3/2}$ state's lifetime, the relative decay strengths can be converted into Einstein A coefficients which are also given in Tab. 7.1. We also list the theoretical predictions of Ref. [103] which are all about 4% higher, a discrepancy much bigger than

for the relative decay strengths. From this point of view, it might be of interest to use a single trapped ion for a measurement of its excited state lifetime [113] or its absolute oscillator strengths.

7.5.4 Measuring Einstein coefficients in a single ion

A large variety of methods exists for measuring transition matrix elements in ensembles of neutral atoms or ions [109]. In view of the discrepancy between the Einstein coefficients calculated from experimental observations and predicted by theory, we would like to propose yet another technique capable of directly measuring Einstein coefficients in a single ion. We will discuss the technique for the case of the decay rate of the $P_{1/2} \leftrightarrow D_{3/2}$ transition.

We start with an ion initially prepared in the $S_{1/2}$ state. A narrow-band laser off-resonantly exciting the $S_{1/2} \leftrightarrow P_{1/2}$ transition pumps the ion into the $D_{3/2}$ state. If the detuning Δ of the laser is much bigger than the inverse of the excited state lifetime, the pumping rate is given by $R = A_{(P_{1/2}-D_{3/2})}\rho_{P_{1/2}}$ where $\rho_{P_{1/2}} = \Omega^2/(4\Delta^2)$ is the excited state population and Ω the Rabi frequency of the laser exciting the transition. The Rabi frequency is related to the AC-Stark shift $\delta_{AC} = \Omega^2/(4|\Delta|)$ experienced by the $S_{1/2}$ state due to the presence of the off-resonant light. In this way, the Einstein coefficient can by expressed by

$$A_{(P_{1/2}-D_{3/2})} = R\frac{\Delta}{\delta_{AC}}.$$

A measurement of the pumping rate could be performed in a similar way as the experiments presented in this chapter by shelving the $S_{1/2}$ population in $D_{5/2}$ prior to quantum state detection. For the determination of the light shift δ_{AC}, a spin echo experiment could be performed on the $S_{1/2} \leftrightarrow D_{5/2}$ transition, measuring the shift of the transition frequency by the light pumping the ion. Measurements of this type have recently been shown [114] to be able to resolve level shifts as small as 1 Hz. To give an example, we assume $\Delta = (2\pi)\,10^{10}$ s^{-1} and adjust the Rabi frequency to get $R = 10^2$ s^{-1}. Because of $A(P_{1/2} - D_{3/2}) \approx 10^7\,\mathrm{s}^{-1}$, the light shift will be $\delta_{AC} = (2\pi)\,10^5$ s^{-1}. To measure the Einstein coefficient to better than 1% would require a measurement of the light shift with a precision of better than 1 kHz within a measurement time somewhat shorter than $1/R = 10$ ms which appears to be feasible.

For a proper treatment, the Zeeman sublevels of the atomic levels need to be taken into account. Fortunately, in the case of the $S_{1/2} \leftrightarrow P_{1/2}$ transition, the pumping rate and the induced light shift are independent of the polarization of the exciting laser as long as it is linearly polarized. In this way, the Einstein coefficient could be independently measured

with high precision to complement the branching ratio measurements presented in this chapter.

7.5.5 Conclusion

Our experiments demonstrate that single trapped ions are perfectly suited for a precision measurement of branching fractions. As compared to experiments based on a single pumping step, the technique of repeated optical pumping offers two important advantages. Firstly, it reduces the number of measurements required for obtaining a given level of accuracy in the case where the transition probabilities to the lower-lying states are very different. Secondly, monitoring the population transfer as a function of the number of the pumping cycle provides a means to detect possible sources of errors like atomic state changes induced by sources other than the lasers used for optical pumping.

The pumping technique used in this chapter requires an atom with a tripod level structure, i.e., an upper state decaying into three lower-lying states. As this level structure exists not only in $^{40}Ca^{+}$ but also in many other isotopes, the method should be widely applicable.

8 Experimental realisation of a quantum walk

The random walk on a line was first introduced more than a century ago [115, 116]. Since then it has become a well known concept in many fields such as physics [117], biology [118], computer science [119] and economics [120].

In 1993 Aharonov *et al.* [121] introduced the quantum walk as the quantum mechanical analogue to the classical random walk. Due to the wave nature of quantum mechanics, interference of the walker with himself is possible, giving rise to striking new features [122]. Similar to its classical counterpart the quantum walk is expected to find applications in various fields, e.g., quantum computation [123] or biology [49].

In the last decade, several experimental realizations of one-dimensional quantum walks have been proposed in various systems, including atoms in an optical lattice [124], trapped ions [125] or cavity QED [126].

In recent years, improved experimental control over single particle systems has allowed realizations of quantum walks performed by a trapped atom in an optical lattice [127], a single trapped ion [128] and photons [129].

In this chapter, a quantum walk on a line in phase space using one and two trapped ions is presented [130]. Several properties of the final state are measured, with the probability distributions visualized by means of the wave function reconstruction method introduced in Sec. 4.5.

The chapter is structured as follows: first, the concept of the quantum walk is introduced and its features are discussed. Next, the experimental realization is presented, followed by the results measured. The chapter concludes with a discussion of these results.

8.1 Concept of the discrete quantum walk on a line

Let us consider a spin-$\frac{1}{2}$ quantum particle described by the wave function $|\Psi_0\rangle$ centered around the initial position x_0. The particle is then state-dependently displaced by the unitary operation $U_\mathrm{d} = \exp\left(-\frac{i}{\hbar}\sigma_j \hat{p} d\right)$ of length d, where $\hat{p}$ is the momentum operator

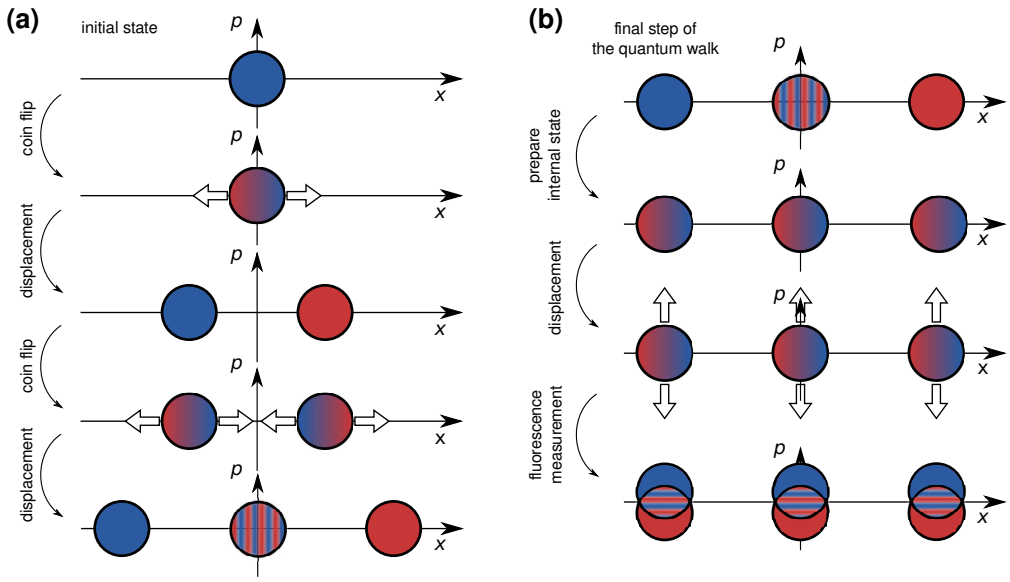

Fig. 8.1: **(a)** Schematic representation of a quantum walk with two steps. The initial state is put into a superposition state, followed by a state-dependent displacement along x that coherently splits the wave function into two parts. Repetition of these two operations leads to interference effects, as depicted schematically in the last stage. **(b)** Schematic representation of the measurement procedure that follows the quantum walk. The internal state is prepared in the required state, and then a state-dependent displacement in the p-direction is performed. This gives rise to interference effects, which can be measured by varying the displacement length and recording the excitation of the internal state. A Fourier transformation of the data obtained allows a reconstruction of the probability distribution in phase space along x.

and σ_j is one of the three Pauli spin matrices (see Eq. (2.24)). This operation coherently splits the wave packet along a line in phase space according to the internal state of the particle. The first step of the quantum walk is completed by a so-called coin-flip operation $U_\mathrm{c} = \exp\left(-i\frac{\pi}{4}\sigma_k\right)$, with $\mathrm{Tr}(\sigma_j\sigma_k) = 0$, which places the internal state into a superposition of the eigenstates of σ_j.

Applying these two unitary operations N times will result in a quantum walk of N steps (see Fig. 8.1(a)), and the initial wave function will have evolved into

$$|\Psi_N\rangle = (U_\mathrm{c}U_\mathrm{d})^N\,|\Psi_0\rangle = \left(e^{-i(\pi/4)\sigma_k}e^{-(i/\hbar)\sigma_j\hat{p}d}\right)^N|\Psi_0\rangle. \tag{8.1}$$

From the procedure described it becomes clear that the walker interferes with himself during each step after the first one. This quantum interference causes the second mo-

mentum of the wave packet to grow linearly with the number of steps: $\langle \hat{x}^2 \rangle \propto N^2$. As the interference does not happen at the outermost positions, the final probability distribution of the quantum walk is peaked on the outer edge. This behaviour differs strongly from the classical case, where the diffusion follows the binomial probability distribution, which grows with the square root of the number of steps performed: $\langle x^2 \rangle \propto N$.

Another property of the quantum walk is its reversibility, as it is composed out of unitary operations that can be undone by applying their inverse. Obviously, this is not possible in the case of the random walk.

These general features apply to all quantum walks, yet the specific shape of the probability distribution is governed by the initial internal state of the walker and the type of coin operation that is used. The most general unitary coin can be written as

$$U_\mathrm{c} = \begin{pmatrix} \sqrt{\rho} & \sqrt{1-\rho}\mathrm{e}^{i\theta} \\ \sqrt{1-\rho}\mathrm{e}^{i\varphi} & -\sqrt{\rho}\mathrm{e}^{i(\theta+\phi)} \end{pmatrix} \tag{8.2}$$

where $0 \leq \theta, \phi \leq 2\pi$ are arbitrary angles and $0 \leq \rho \leq 1$. An irrelevant global phase has been removed leaving the leading diagonal element real. Any input state can be written as

$$|\Psi\rangle_\mathrm{input} = (\sqrt{\eta}|+\rangle_z + \sqrt{1-\eta}\mathrm{e}^{i\alpha}|-\rangle_z)|x_0\rangle. \tag{8.3}$$

A straightforward approach to get a symmetric probability distribution is to use a balanced coin operator ($\rho = 1/2$) and input state ($\eta = 1/2$). In this case, $\alpha + \theta$ has to be $\pi(m + 1/2)$ with integer m [131].

From these requirements, we can see that for an implementation in our experiment, the $R_x(\pi/2)$ and $R_y(\pi/2)$ single-ion operations described in Sec. 2.1.5 are possible balanced coin operations, where $|\pm\rangle_x$ and $|\pm\rangle_y$ are suitable respective input states for a symmetric quantum walk. In contrast to the displacement operator in the theoretical description in Ref. [131], the state-dependent displacement operator employed in our experiment does not act in the z-basis. This can be taken into account by substitution of the experimental displacement operator by a displacement operator acting on the z-basis that is sandwiched between two rotation operations that rotate from the basis of the displacement operator to the z-basis and back. The criteria given above then have to be applied to the resulting input state and coin-flip operations.

Fig. 8.2 shows simulations of a symmetric and an asymmetric quantum walk of 20 steps assuming the validity of the Lamb-Dicke approximation. While the coin flip operation was used to set the symmetry of the walk ($R_x(\pi/2)$ or $R_y(\pi/2)$), the displacement operation was set to a step size of twice the width of the ground state ($d = 2\Delta_x$). The resulting overlap of the first two wave packets is about 2% but, as can be seen in both

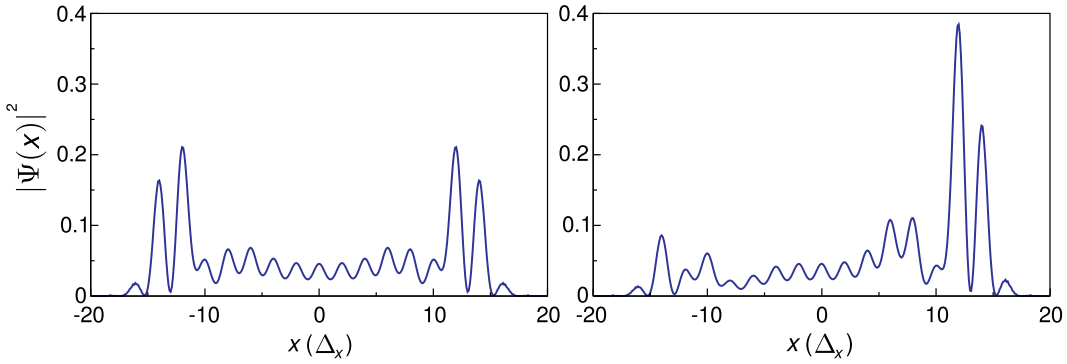

Fig. 8.2: Simulation of a symmetric ($\alpha + \theta = \pi/2$, right plot) and an asymmetric ($\alpha + \theta = 0$, left plot) probability distribution for a quantum walk of 20 steps ($\rho = \eta = 1/2$ in both cases). The displacement step size is twice the width of the ground state wave packet ($d = 2\Delta_x$) resulting in an overlap of the two wave packets of only 2% after the first step. This corresponds to the unitary operation used in the experimental realization.

plots, after 20 steps the local minima around the center are less pronounced than at the positions further away from the center. The reason for this is that more interference events happen in the center, where the overlap results in a mixing of the wave packets.

8.2 Experimental realisation

For the experimental implementation a single $^{40}Ca^{+}$ ion is trapped with radial and axial trap frequencies of $\omega_{\mathrm{rad}} \approx (2\pi)$ 3 MHz and $\omega_{\mathrm{ax}} = (2\pi)$ 1.356 MHz, respectively. Doppler cooling, resolved sideband cooling on the $S_{1/2} \leftrightarrow D_{5/2}$ transition in a magnetic field of 4 G prepare the ion in the axial motional ground state and in the internal state $|S_{1/2}, m = 1/2\rangle \equiv |-\rangle_z$. The narrow linewidth laser at 729 nm coherently couples the states $|-\rangle_z$ and $|D_{5/2}, m = 3/2\rangle \equiv |+\rangle_z$.

The coin-flip operation is performed by a $\pi/2$-pulse on the carrier transition.

A bichromatic light field resonant with the upper and lower axial motional sidebands of the $|-\rangle_z \leftrightarrow |+\rangle_z$ transition performs the state-dependent displacement described in Sec. 4.4. By setting $\phi_- = \pi/2$ and $\phi_+ = 0$ in Eq. (4.19) the Hamiltonian

$$H_{\mathrm{d}} = -2\eta\Omega\Delta_x\sigma_x\hat{p} \tag{8.4}$$

is realized. Applying the two light fields for a fixed time τ generates the wanted propagator U_{d} with $d = 2\eta\Omega\tau\Delta_x$ where $\Delta_x = \sqrt{\hbar/2m\omega_{\mathrm{ax}}}$ is the size of the harmonic oscillator ground state. In our experiment we use a pulse of 40 µs with a Rabi frequency of

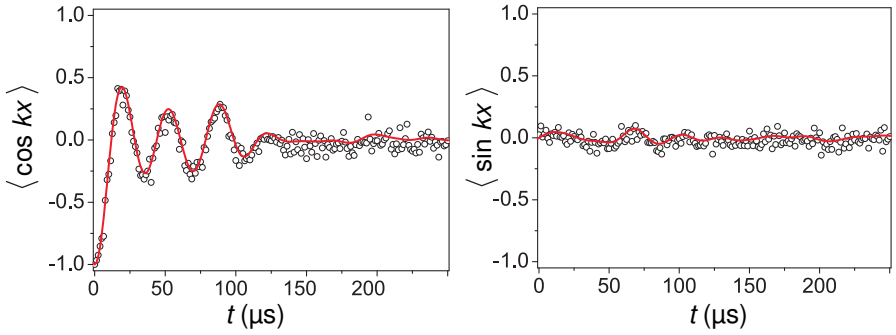

Fig. 8.3: Measurement of the Fourier components $\langle \cos(kx) \rangle$ and $\langle \sin(kx) \rangle$ for a seven-step quantum walk. The data are obtained by varying the duration of the probe pulse for the ion prepared in the internal state $|+\rangle_z$ (left) or $|+\rangle_y$ (right) after completing the walk. The probability distribution is obtained by Fourier transforming a fit to the data (solid line). The data displayed in the right plot deviates slightly from the expected flat line of a symmetric quantum walk. We attribute this to slow drifts of experimental parameters. The reconstructed probability distribution is shown in Fig. 8.4 in the fifth graph.

$\Omega = (2\pi)68$ kHz to achieve a step size of $d = 2\Delta_x$. This is a good compromise as it creates two nearly orthogonal wave packets with an overlap of approximately 2% but still allows for a large number of steps.

By repeating these two basic building blocks of a step we can perform the quantum walk and reconstruct its wave function afterwards with the method described in Sec. 4.5. The approximation for the displacement Hamiltonian in Eq. (4.27) that ignores the kinetic energy of the state is well justified in the case of our quantum walk, as the states produced show a much bigger spread along x than along p.

A schematic representation of the measurement procedure can be seen in Fig. 8.1(b). For the reconstruction we set $\Omega_\mathrm{p} = (2\pi)$ 26 kHz and measure $\langle \sigma_z \rangle$ for probe times between 0 and 300 μs. The displacement along p is realized by routing the RF signal to the AOM through a slightly longer BNC cable that causes the signal to be phase-shifted by $\pi/2$. The desired cable length is selected with an accuracy of ± 1 cm using standard connectors. For a signal at 80 MHz the resulting error in the phase shift is less than a percent. Fig. 8.3 shows the even and uneven Fourier components of a seven-step quantum walk.

The reconstructed probability distribution $\langle \delta(\hat{x} - x) \rangle$ based on the even Fourier components for up to 13 steps can be seen in Fig. 8.4. This is in principle sufficient since the performed walk is symmetric. Additionally, the uneven terms were checked to be close

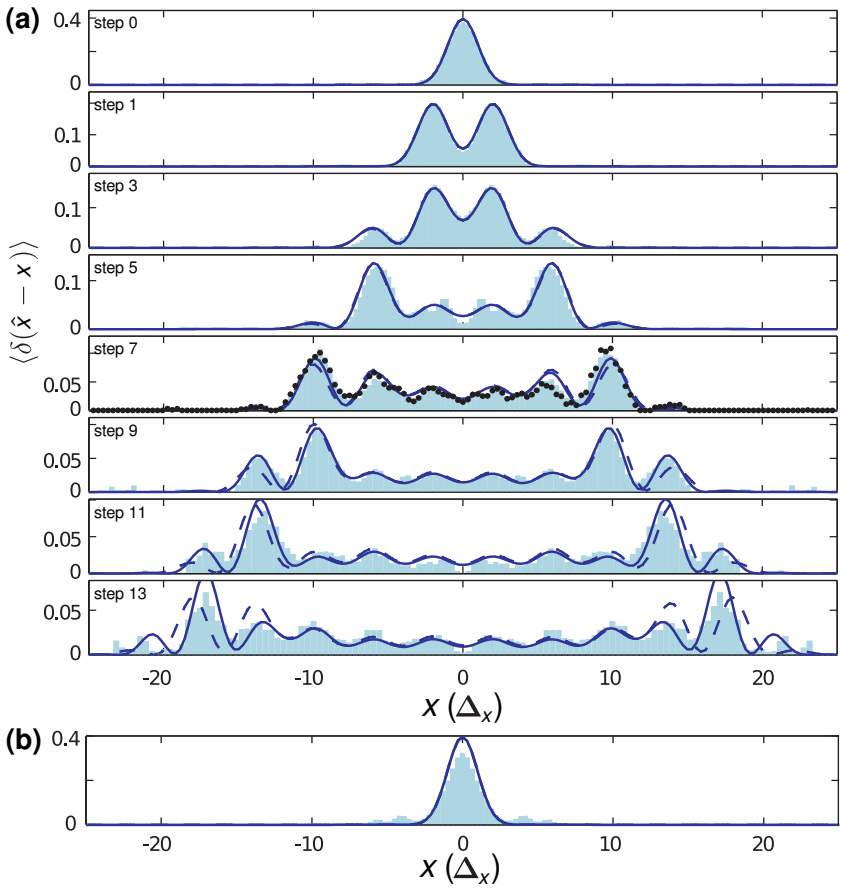

Fig. 8.4: **(a)** Reconstruction of the symmetric part of the probability distribution $\langle\delta(\hat{x}-x)\rangle$ for up to 13 steps in the quantum walk. The blue dashed curve is a numerical calculation for the expected distribution within the Lamb-Dicke regime. The blue solid curve takes into account corrections to the Lamb-Dicke regime. In step 7, the dotted curve represents the full reconstruction using also the $\langle\sin(kx)\rangle$ shown to the right in Fig. 8.3. **(b)** Probability distribution of a five-step quantum walk after application of five additional steps which invert the walk and bring it back to the ground state.

to zero for all N. The dashed lines in the plots are numerical simulations based on the Lamb-Dicke approximation. These lines deviate from the reconstructed distribution for $N > 7$ due to higher order terms in η that are not taken into account. The solid lines are based on a numerical simulation using resonant terms up to the third order.

To get smoother distributions additional constraints were invoked by the reconstruction algorithm. The maximal kinetic energy is a physical constraint that can be estimated by the measured momentum distribution.

For a wave function $\psi = A(x)e^{i\phi(x)}$, a lower bound on the kinetic energy is given by

$$\begin{aligned}
\langle\frac{\hat{p}^2}{2m}\rangle &= \frac{\hbar^2}{2m}\int_{-\infty}^{\infty}\mathrm{d}x\left(\left(A(x)\phi'(x)\right)^2 - A(x)A''(x)\right) && (8.5)\\
&\quad \underbrace{-\frac{\hbar^2}{2m}\int_{-\infty}^{\infty}\mathrm{d}x\frac{\mathrm{d}}{\mathrm{d}x}\left(A(x)^2\phi'(x)\right)}_{=0} && (8.6)\\
&= \frac{\hbar^2}{2m}\int_{-\infty}^{\infty}\mathrm{d}x((A(x)\phi'(x))^2 + A'(x)^2) && (8.7)\\
&\geq \frac{\hbar^2}{2m}\int_{-\infty}^{\infty}\mathrm{d}xA'(x)^2 && (8.8)
\end{aligned}$$

where differentiation with respect to x is indicated by primes. For $p(x) = |\psi(x)|^2$, we then have because of $A(x) = p(x)^{\frac{1}{2}}$ and $A'(x) = \frac{1}{2}p'(x)p(x)^{-\frac{1}{2}}$ that

$$\langle\frac{\hat{p}^2}{2m}\rangle \geq \frac{\hbar^2}{8m}\int_{-\infty}^{\infty}\mathrm{d}x\frac{p'(x)^2}{p(x)}. \tag{8.9}$$

This constraint is also valid for mixed quantum states (see Appendix B for details). Eq. (8.9) can be implemented in our optimization algorithm as an additional convex constraint. The kinetic energy of the analyzed state is provided as an input to the algorithm so that it excludes distributions $p(x)$ that are not compatible with this constraint, i.e., that have excess kinetic energy. As the kinetic energy is linked to the derivative of $p(x)$, the probability distributions obtained show less steep gradients, resulting in smoother distributions $p(x)$. Adding the constraint works particularly well for the states produced by the quantum walk. These states ideally do not have any phase gradients $\phi'(x)$, in which case inequality (8.9) becomes an equality.

The measurement for the width of the wave packet along the x- and p-axis can be seen in Fig. 8.5(a). The data for $w_x = \sqrt{\langle\hat{x}^2\rangle}$ was directly taken from the reconstructed probability distributions and shows both the linear dependence of $\langle x\rangle$ and N and that the momentum distribution is not seriously affected during the walk. The measurement of $w_p = \sqrt{\langle\hat{p}^2\rangle}$ was obtained using quadratic fitting for short probe times (see Sec. 4.5.1).

The third (red) line in Fig. 8.5(a) is the width of a classical walk we also realized in our setup. To this end, the phase is randomized between each step while keeping the coin flip-displacement operator pair coherent for each individual step. The phase for each step was generated by a random noise generator. This mimics a completely mixed ensemble of measurement outcomes that behaves classically. By reducing the amplitude in the noise signal, we were able to set the results to any point between the classical and the quantum regime. A good way of quantifying the difference between the quantum

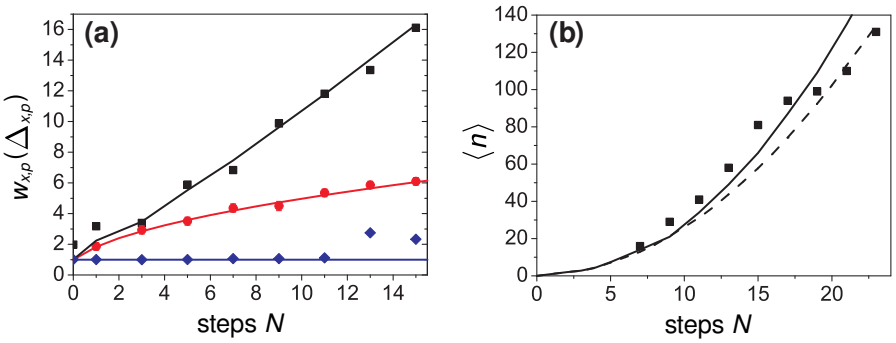

Fig. 8.5: **(a)** Width w_x of the probability distribution in units of the ground state size Δ_x as a function of the number of steps for a quantum (■) walk. The solid curve represents a full numerical simulation of the quantum walk as realized in the experiment. The width of the x-distribution for a classical random walk (●) increases more slowly and is described (solid red line) by Eq. (8.10). The data points (♦) show the measured width w_p of the marginal distribution along the p-direction with $\Delta_p = \hbar/2\Delta_x$. **(b)** Average number of vibrational quanta after N steps in the quantum walk measured by driving oscillations on the carrier transition. The solid line is based on a full simulation, the dashed line assumes the validity of the Lamb-Dicke approximation.

and classical walks is by measuring the average width of the probability distributions. For a classical walk with a step size $d = s\Delta_x$ we have

$$w_x = \Delta_x \sqrt{\frac{2s^2 N}{\pi} + 1}, \tag{8.10}$$

where the second term takes into account the initial width Δ_x of the probability distribution. To measure w_x for the random walk, the curvature of $\langle \sigma_z \rangle$ at short probe-time was analyzed. Quadratic fitting gives direct access to the width w_x as presented in Sec. 4.5.1.

To avoid problems in the measurement of the motional state due to leaving the Lamb-Dicke limit for large numbers of steps, we implemented a method suggested in Ref. [132]. Outside the Lamb-Dicke regime the coupling strength $\Omega_{n,n}$ on the carrier depends on the phonon number n as $\Omega_{n,n} = \Omega_0 L_n(\eta^2)$. Here, $L_n(\eta^2)$ is the n-th order Laguerre polynomial. The mean phonon number $\langle n \rangle$ is determined by a constrained least-square fit of the carrier Rabi flops with the number state distribution as a fit parameter. In Fig. 8.5(b), the resulting average vibrational quantum numbers are shown. As expected for the quantum walk, we observe a quadratic dependence $\langle n \rangle \propto N^2$ on the number of steps.

To demonstrate the reversibility of the quantum walk we performed a quantum walk of five steps and refocused it afterwards. This was done by switching the phase of the

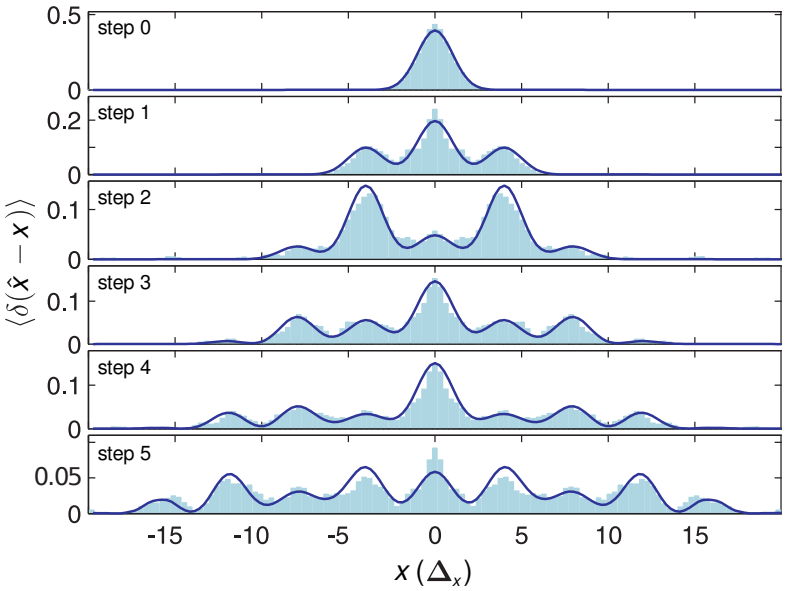

Fig. 8.6: Reconstructed probability distribution $\langle\delta(\hat{x}-x)\rangle$ for a two-ion quantum walk with up to five steps with a step size of $4\Delta_x$.

subsequent five displacement and coin flipping pulses by π. In this way the quantum walk is exactly reversed and the ion returns to the ground state. The corresponding reconstructed probability distribution shown in Fig. 8.4 (b) closely resembles the one of the initial state and demonstrates once more the coherence of the quantum walk.

8.2.1 Extension with two ions

In the case of trapped ions the extension to two walkers is straight forward by simply adding another ion to the system. In our case we make use of the lowest common vibrational mode, the center-of-mass mode. To account for the second ion, all Pauli matrices σ_i in Eq. (8.1) are replaced by $\sigma_i^{(1)} + \sigma_i^{(2)}$. This changes the coin from two sided to four sided, with three possible operations. The "side" belonging to the state $|++\rangle_x$ ($|--\rangle_x$) corresponds to a step to the right (left) while the sides belonging to the states $|+-\rangle_x$ and $|-+\rangle_x$ correspond to no step at all. The ions are prepared in the state $|++\rangle_y$ with a $\pi/2$-pulse leading to a symmetric walk. For the two ion quantum walk all pulses are applied to both ions simultaneously. The probability distribution of the center of mass mode is obtained in the same way as for a single ion. The results for a walk of up to five steps are shown in Fig. 8.6. Again, the distribution deviates strongly from the classical version and shows a faster spreading.

8.3 Discussion

The experiments presented in this chapter could be further extended in two dimensions by using two ions and second vibrational mode, allowing the walk to be performed with entangled walkers. A two-dimensional quantum walk with photons has been demonstrated in the meantime [133]. With the use of squeezed states [58] it might be possible to increase the number of possible steps even further, but this approach also has limits, as the squeezing would affect the reconstruction measurement that would be performed along the perpendicular axis in phase space. However, all possible realizations within reach at the moment cannot reproduce the number of steps in theoretical investigations ,e.g., Ref. [134]. These investigations also look into modifications of the walk, such as sites that can absorb the walker [135, 136], which are not possible to implement in our current setup. Still, the quantum walk is a good way to benchmark the control over a quantum system, in our case, the system is the the harmonic oscillator coupled to a qubit.

From the results it is possible to identify experimental imperfections and error sources in our implementation of the quantum walk. The most dominant deviation from the ideal quantum walk is visible in the failure of the Lamb-Dicke approximation. Strictly speaking, this is not an error but a modification that can be accounted for in the evaluation. Yet the dependence of the coupling strength gives rise to other errors. The quantum states produced during the quantum walk spread out over many phonon modes. As a result, the coupling strength for the displacement operator and the coin flip operations differ over the wave function, reducing the fidelity of these operations.

Decoherence is another contributing error source. Typical coherence times of our qubit in the setup we used are two to three milliseconds. Each step takes 40 µs for the displacement and about 10 µs for the coin flip operation. As the pulse sequence for the state measurement take up to 300 µs, it can be seen that quantum walks of 20 steps are on the same time scale as the qubit coherence time. However, the largest error source for the presented experiments is motional decoherence. Even small fluctuations in the trap frequency heavily affect large wave functions but could be addressed by technological improvements.

The motional coherence time can be prolonged by simple technological improvement, by a voltage supply with higher stability. The internal state coherence can be prolonged with magnetic shielding, which is already installed in the new setup. In the case of the failure of the Lamb-Dicke approximation, more substantial changes would be necessary to improve the situation. The use of higher trap frequencies and higher laser power would

be one way to reduce the Lamb-Dicke parameter without sacrificing coupling strength.

Another option would be the use of an ion trap with a magnetic field gradient at the position of the ion [137]. In these traps the magnetic field gradient changes the Coulomb interaction of the ion depending on its internal state. Given suitable internal levels of the ion separated by a few gigahertz, the internal states can be coupled to the motional state, while microwave radiation is used to drive the transitions between these levels. This technology has the advantage that the wavelength used is several orders of magnitude larger than the spatial extension of the ion's wave packet in the trap. For these wavelengths, in contrast to optical wavelengths, the Lamb-Dicke approximation is still a good one. However, the implementation of such a magnetic field gradient increases the technical overhead.

9 Quantum simulation of the Klein paradox

One motivation for analogue quantum simulations is the use of a controllable laboratory system to investigate a quantum system that is not as easily accessed or cannot efficiently be simulated on a classical computer [1]. The laboratory system has to allow for a controlled state initialisation, a mapping of the observables between both systems, and it has to have the same underlying mathematical model as the system under investigation.

Recently, we investigated the one dimensional Dirac equation using a single ion [45, 79]. *Zitterbewegung*, a peculiar quivering motion of the free Dirac particle, was studied, as well as the cross-over from relativistic to non-relativistic dynamics.

This chapter is based on Ref. [138], in which we used a second ion to extend the previous work by simulating external potentials for the Dirac particle. The simulated state of the scattered particle is encoded both in the electronic and vibrational state of an ion, representing the discrete and continuous components of relativistic wave functions. The high level of control over our system and the reconstruction of the particle wave packet are used to demonstrate textbook examples of relativistic scattering "frame-by-frame".

9.1 The Dirac equation

The Dirac equation successfully merges quantum mechanics and special relativity and provides a natural description of the spin. Additionally, it accurately reproduces the spectrum of the hydrogen atom, and it predicted the existence of anti-matter [139]. However, several properties of the Dirac equation are, due to technical difficulties, not directly observable, suggesting quantum simulation as a way to provide new insights. Different physical setups have been proposed to investigate relativistic quantum effects [140–146]. Experimental realizations have been shown with photonic lattices [147] and trapped ions [45].

The following text gives a short introduction to the Dirac equation and how to simulate it with ions. The introduction to the 1+1 dimensional Dirac equation follows closely Ref. [148] and further details on our experimental implementation can be found

in Ref. [45, 79].

The equation for a spin-1/2 particle with mass m is given by

$$i\hbar\frac{\partial\psi}{\partial t} = \left(c\alpha\cdot\hat{\mathbf{p}} + \beta mc^2\right)\psi, \tag{9.1}$$

where c is the speed of light, $\hat{\mathbf{p}}$ is the momentum operator, and α and β are the Dirac matrices:

$$\alpha_i = \begin{pmatrix} 0 & \sigma_i \\ \sigma_i & 0 \end{pmatrix}, \quad \beta = \begin{pmatrix} I_2 & 0 \\ 0 & I_2 \end{pmatrix}, \tag{9.2}$$

where σ_i are the Pauli matrices and I_2 is the identity in two dimensions (see Eq. (2.24)). As the entries in the Dirac matrices are 2-by-2 matrices, the wave function ψ is a 4-component spinor related to the spin and the positive or negative energy solutions.

By going to 1+1 dimensions, the equation simplifies to [140, 148]

$$i\hbar\frac{\partial\psi}{\partial t} = \left(c\hat{p}\sigma_x + mc^2\sigma_z\right)\psi = H_{\mathrm{D}}\psi \tag{9.3}$$

but still shows effects such as *Zitterbewegung* [149] or the Klein paradox [150].

The two components of the spinor in 1+1 dimensions do not represent the spin, as all magnetic fields in one dimensions are pure gauge fields [148]. Here, they are associated with the appearance of positive and negative energy states

$$\psi(x,t) = \begin{pmatrix} \psi_1(x,t) \\ \psi_2(x,t) \end{pmatrix}. \tag{9.4}$$

The matrix H_{D} in Eq. (9.3) has two eigenvalues $E(p) = \pm\sqrt{p^2c^2 + m^2c^4}$. We write the two types of plane wave solutions to the Dirac equation $u_\pm(p;x,t)$ as

$$u_\pm(p;x,t) = \frac{1}{\sqrt{2\pi}}u_\pm(p)e^{ipx/\hbar\mp iE(p)/\hbar t} \tag{9.5}$$

with $u_\pm$ the eigenvectors corresponding to the respective eigenvalues $E(p)$. These plane waves are solutions to the Dirac equation with positive and negative energy

$$H_{\mathrm{D}}\ u_\pm(p;x,t) = \pm E(p)\ u_\pm(p;x,t). \tag{9.6}$$

The probability of finding the particle between $x = +\infty$ and $x = -\infty$ has to be one, hence we demand that the integral $\int_{-\infty}^{+\infty}(|\psi_1(x,t)|^2 + |\psi_2(x,t)|^2)dx$ is equal to one. Of course, the same argument holds for the momentum distribution given by the Fourier transformed spinors $\hat{\psi}_{1,2}(p,t) = \mathfrak{F}(\psi_{1,2}(x,t))$. The normalization of the Dirac spinor is time-independent due to the unitary time evolution of the Dirac equation. This remains true for arbitrary external fields. As a result, the Dirac equation cannot describe particle

creation or annihilation; quantum field theory is needed to describe these processes. In the Dirac equation it is always the case that if there is a particle at the beginning, there will be a particle in the end. Of equal importance for the experiments presented in this chapter is the notion that the individual components $\psi_{1,2}$ are not normalized.

Square-integrable wave packets can be obtained by the superposition of plane waves

$$\psi(x,t) = \int_{-\infty}^{+\infty} (\hat{\psi}_+(p)\ u_+(p;x,t) + \hat{\psi}_-(p)\ u_-(p;x,t))dp. \tag{9.7}$$

The coefficient functions $\hat{\psi}_\pm(p)$ can be obtained by a projection of $\psi(p,0)$ onto the positive and negative energy subspace

$$\hat{\psi}_\pm(p) = P^\pm(p)\psi(p,0). \tag{9.8}$$

$\psi(p,0)$ is obtained by Fourier transforming the initial wave function $\psi(x,0)$. In momentum space, the projection operators are given by

$$P^\pm(p) = \frac{1}{2}\left(I_2 \pm \frac{H_\mathrm{D}(p)}{E(p)}\right) = \frac{1}{2}\left(I_2 \pm \frac{c\hat{p}\sigma_x + mc^2\sigma_z}{\sqrt{c^2\hat{p}^2 + m^2c^4}}\right). \tag{9.9}$$

From this expression it can be seen that in the general case the positive and negative energy states are not encoded in the spinor; this only holds for $p = 0$.

The positive and negative energy parts of the spinor are important for the occurrence of Zitterbewegung. The velocity of a particle described by the 1+1 dimensional Dirac equation is

$$d\hat{x}/dt = [\hat{x}, H_\mathrm{D}]/i\hbar = c\sigma_x \tag{9.10}$$

in the Heisenberg picture. In the case of a massless particle σ_x is a constant of motion because $[\sigma_x, H_\mathrm{D}] = 0$ holds. For a massive particle, on the other hand, $\hat{x}$ and H_D no longer commute, and the evolution of the particle is described by [149]

$$\hat{x}(t) = \hat{x}(0) + \hat{p}c^2 H_\mathrm{D}^{-1} t + i\,\hat{\xi}(e^{2iH_\mathrm{D}t/\hbar} - 1), \tag{9.11}$$

with $\hat{\xi} = \frac{1}{2}\hbar c(\sigma_x - \hat{p}cH_\mathrm{D}^{-1})\,H_\mathrm{D}^{-1}$. The last term deviates from the description of a free particle and may cause Zitterbewegung. For Zitterbewegung to appear, both energy parts have to be present with a significant overlap in position and momentum space. It does not occur for spinors that consist entirely of positive or negative energy.

Eq. (9.3) can be realized with an ion by using a bichromatic beam resonant with the sidebands of a vibrational mode and an additional beam that causes an AC-Stark shift [140]. Applying all three light fields simultaneously realizes the Hamiltonian

$$H_\mathrm{D} = 2\eta\Delta\tilde{\Omega}\sigma_x\hat{p} + \hbar\Omega\sigma_z \tag{9.12}$$

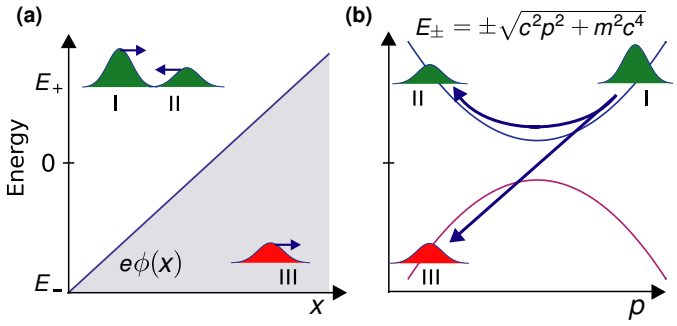

Fig. 9.1: Klein tunneling in position **(a)** and momentum space **(b)**, for a relativistic particle scattering from a linear potential $\phi(x) = gx$. A wave packet initially in the positive energy branch and with positive momentum (I) moves up a slope where it can reflect (II) while remaining in the positive energy branch or tunnel (III) while switching energy branch.

where η is the Lamb-Dicke parameter, $\tilde{\Omega}$ is the bichromatic Rabi frequency (see Eq. (4.19)) and 2Ω is the overall detuning of the AC light field from resonance of the carrier transition. The momentum operator is $\hat{p} = i\hbar(a^\dagger - a)/2\Delta$ with $\Delta = \sqrt{\hbar/4\tilde{m}\omega_{\mathrm{ax}}}$, the size of the ion's ground state wave function, $\tilde{m}$ the ion's mass (not to be confused with the mass of the simulated particle) and $a^\dagger$ (a) the creation (annihilation) operator on the vibrational mode used.

The first term is obtained by setting the proper phases in Eq. (4.19) and the second term is caused by the AC-Stark shift. Instead of using the second beam it is also possible to detune both bichromatic beams from resonance in the same direction. By making the identifications $c := 2\eta\tilde{\Omega}\Delta$ and $mc^2 := \hbar\Omega$, this becomes equivalent to Eq. (9.3).

The time evolution of an arbitrary input state can then be studied by applying the detuned bichromatic laser field for a certain time, followed by either a full wave reconstruction or by looking at a certain parameter of interest, such as $\langle\hat{x}\rangle$.

9.2 The Klein paradox

In its original form [150] the Klein paradox considers a relativistic electron described by the Dirac equation, with total energy E and rest mass energy mc^2, hitting a step-shaped potential barrier of height V. For barrier heights smaller than the kinetic energy of the electron, $V < E - mc^2$, the particle is predicted to partially transmit. For a slightly larger barrier, $E + mc^2 > V > E - mc^2$, the particle should completely reflect. These situations agree with the predictions of the (non-relativistic) Schrödinger equation. However, for

$V > E + mc^2$ the particle can propagate undamped in the potential barrier, by turning into its anti-particle. This effect is known as the Klein paradox. Klein's results have been extended to other types of potentials [151–153] and the physics of Klein tunneling emerges for electrons in graphene [154–156]. In quantum field theory, the paradox is resolved by the notion of pair creation by the external potential [157, 158].

In one dimension, the Dirac equation for a particle in an electrostatic potential $\phi(x)$ is given by Ref. [159]

$$i\hbar\frac{\partial\psi}{\partial t} = \left(c\,\hat{p}\,\sigma_x + mc^2\sigma_z + e\phi(x)I_2\right)\psi = H_{\mathrm{D,lp}}\psi. \tag{9.13}$$

Here c is the speed of light, $\hat{p}$ the momentum operator, m the particle mass and e its charge. In one dimension there is no spin (no magnetic fields) and therefore the wave functions ψ are 2-component spinors, reflecting that there are positive and negative energy solutions $E_\pm = \pm\sqrt{c^2p^2 + m^2c^4}$. A spinor allows for arbitrary superpositions of these components. Free particles ($\phi(x) = 0$) in one of the two energy branches remain there indefinitely, but for $\phi(x) \neq 0$ the spinor can switch energy branch and Klein tunneling can occur.

For linear potentials $e\phi(x) = gx$ the situation is conceptually equivalent to Landau-Zener tunneling [151, 159, 160], as shown in Fig. 9.1. Depending on the size of the splitting of the two energy branches ($2mc^2$) and the acceleration (g/m), the particle can either adiabatically follow the positive energy branch and reflect, or make a non-adiabatic transition to the negative energy branch and tunnel. For ultra-relativistic particles ($c^2p^2 \gg m^2c^4$), the energy branches are linear and have the slope $E_\pm = \pm c$. The other important parameter in this process is the change in momentum of the particle

$$d\hat{p}/dt = [\hat{p}, H_{\mathrm{D,lp}}]/i\hbar = g \tag{9.14}$$

given by the linear potential gx. Both parameters, together with the mass, enter the probability for tunneling, which is given by [160]

$$P_{\mathrm{tunnel}} = \mathrm{e}^{-2\pi\frac{m^2c^3}{2\hbar g}} = \mathrm{e}^{-2\pi\Gamma}. \tag{9.15}$$

With the mass of the particle m given and all other factors being constants, the tunneling probability depends only on the slope g. In Fig. 9.1(b) this can be interpreted as the speed with which the initial wave packet is moved to the other branches. As the states created in our experiment are only approximately ultra-relativistic, the Landau-Zener formula (Eq. 9.15) should be considered an ideal case for the tunneling rate.

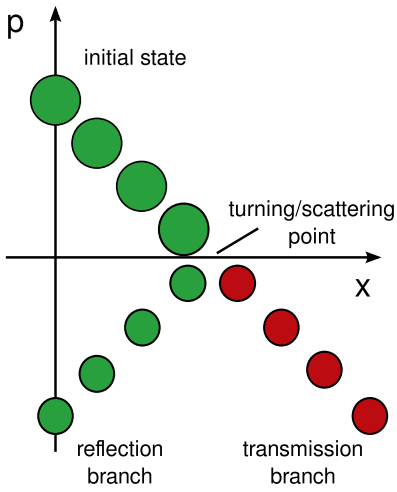

Fig. 9.2: Phase space representation of the scattering event with a steep slope. The wave packet is prepared in a state with high momentum and evolves under the influence of the slope. At the turning point a fraction of the wave packet switches energy branches and Klein tunneling occurs, while the remainder of the wave packet is reflected. Positive energy states are colored in green, while negative ones are red.

9.3 Experimental realization

For the purpose of an experimental realization it is necessary to create a potential which depends on the position of the wave packet in phase space. As the implementation of a step-shaped potential is not possible in our setup, we decided on a linear and a quadratic potential, since these are feasible and still show Klein tunneling [159]. For the case of a linear potential, the resulting dynamics in phase space are represented in Fig. 9.2. The wave packet is initialized as a purely positive energy state with high momentum. During its time evolution, it will slow down because of the slope. At the turning point, one part of the wave packet gets reflected while, depending on the slope, a fraction of the wave packet turns into a negative energy state. While moving in opposite directions, both wave packets get accelerated by the slope.

There are at least two possible ways to implement such a potential in our experiment. The following section will briefly discuss both of them.

9.3.1 Possible implementations

As presented in Sec. 2.2.1, a resonant, oscillating force applied to the ion in the trapping potential results in a displacement operation. This displacement acts as a slope, while

the other terms of the Hamiltonian in Eq. (9.13) are realized with a bichromatic beam as in Ref. [45]. The technical realization is straightforward by applying a radio frequency (RF) signal to the tips of the trap. This option is not state-dependent on the internal state of the ion and can only realize linear potentials.

Another option, which was used in the experiments presented here, is to use a second bichromatic light field driving a different transition on a second ion. Of course, both bichromatic light fields have to couple to the same vibrational mode. By performing a displacement operation on the second ion, the slope is directly realized for the other ion. Similar to the Hamiltonian in Eq. (9.12) the Hamiltonian for two ions with two bichromatic light fields, one acting on each ion can be written as

$$H_{\mathrm{KP}} = 2\eta\Delta\tilde{\Omega}_1\sigma_x^{(1)}\hat{p} + \hbar\Omega_1\sigma_z^{(1)} + \eta\tilde{\Omega}_2\sigma_x^{(2)}\hat{x}/\Delta + \hbar\Omega_2\sigma_z^{(2)} \tag{9.16}$$

where the brackets denote the ion to which the spin operation is applied. From this expression it can be easily seen that the slope proportional to $\hat{x}$ is realized by using the second bichromatic light field with no detuning on the second ion ($\Omega_2 = 0$).

Additionally, the second bichromatic light field can be used to implement a quadratic potential. If the center frequency is far detuned from the resonance ($\Omega_2 \gg \eta\tilde{\Omega}_2$), Eq. (9.16) can be approximated as [159]

$$H_{\mathrm{KP}} \approx 2\eta\Delta\tilde{\Omega}_1\sigma_x^{(1)}\hat{p} + \hbar\Omega_1\sigma_z^{(1)} + \frac{\hbar\eta^2\tilde{\Omega}_2^2\hat{x}^2}{2\Delta^2\Omega_2}\sigma_z^{(2)}. \tag{9.17}$$

Here, the AC-Stark effect has the same behaviour as described in Sec. 4.3.1. The $\sigma_z^{(2)}$ operation is realized with an effective coupling strength given by the resonant coupling strength squared, divided by twice the detuning.

Another way of looking at this is that this case corresponds to the classical limit of a particle with a large mass. As the classical Hamiltonian for a free particle is given by $H_{\mathrm{cl}} = p^2/2m$, the resulting Dirac Hamiltonian is proportional to $\hat{p}^2$, which can be exchanged for $\hat{x}^2$ in the harmonic oscillator by a simple phase shift.

9.3.2 Experimental setup

The laser setup presented in Sec. 5.5.2 and Fig. 5.5 was modified to realize the second bichromatic light field with perpendicular polarization. The modification can be seen in Fig. 9.3. The initial beam is split into two arms by a $\lambda/2$ plate and a polarizing beam splitter (PBS). Both arms consist of an AOM in double pass configuration making it possible to set the center frequency of both bichromatic beams. The two frequency modulated beams leave the PBS in the forth direction with orthogonal polarization.

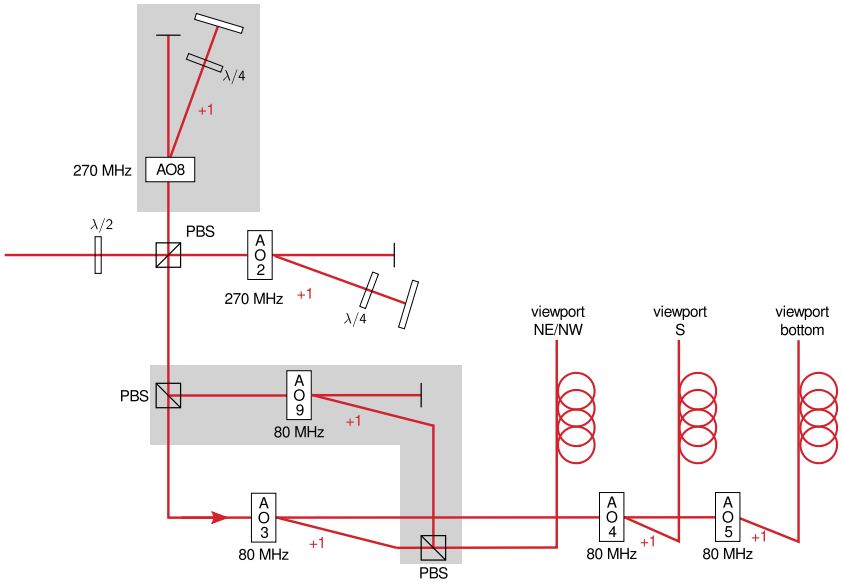

Fig. 9.3: Modification to the laser setup shown in Fig. 5.5. The optical paths that have been added are highlighted by a grey background. Two AOMs were added to the setup. While AO8 is used to set the new center frequency for the second bichromatic beam, AO9 is driven by the same RF signal as AO3 but the signal can be independently phase-shifted. The two driving frequencies differ by exactly twice the trap frequency. A convenient feature of this setup is that both bichromatic light fields are perpendicular in polarization. As the light passes through a $\lambda/4$ wave plate after the fiber, the polarization of both light fields (σ^- and σ^+) is optimized for their respective transition ($|\mathrm{S}_{1/2}, m = 1/2\rangle \leftrightarrow |\mathrm{D}_{5/2}, m = 3/2\rangle$ and $|\mathrm{S}_{1/2}, m = -1/2\rangle \leftrightarrow |\mathrm{D}_{5/2}, m = -3/2\rangle$). In this way, each bichromatic light field causes very little light shifts on the other transition.

This beam is then split again by another PBS, sending both light fields through their respective AOM that create the bichromatic light field. Afterwards, the beams are overlapped on a third PBS. The resulting laser beam consists of two bichromatic light fields with perpendicular polarisation that are then coupled into the fiber leading to the experiment.

The discrete components of the spinor are encoded in the first ion using our normal qubit transition $|\mathrm{S}_{1/2}, m = 1/2\rangle \leftrightarrow |\mathrm{D}_{5/2}, m = 3/2\rangle$, while the $|\mathrm{S}_{1/2}, m = -1/2\rangle \leftrightarrow |\mathrm{D}_{5/2}, m = -3/2\rangle$ transition is used for the second ion (see Fig. 9.4). We will denote the upper (lower) state of the ions $\binom{1}{0}_j$ $\left(\binom{0}{1}_j\right)$, where j is the number of the ion. As both bichromatic fields have perpendicular polarization (σ^+ and σ^- when entering the vacuum vessel), they are optimized for their respective transition, particularly reducing

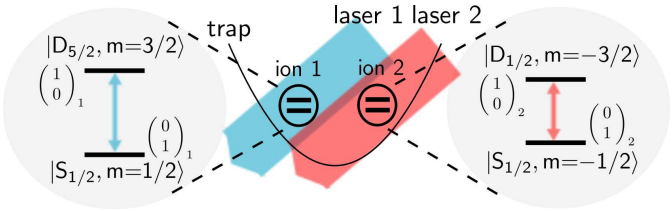

Fig. 9.4: The Dirac spinor is encoded in an internal state of ion 1 and a collective motional state of both ions. The Hamiltonian for a free Dirac particle (H_{D}) is implemented by bichromatic laser 1 which couples ion 1 to the collective motional mode. A second bichromatic laser couples ion 2 to the same motional mode and in this way creates the potential $\phi(x)$.

AC-Stark shifts on the other ion. The continuous position and momentum components are mapped to the quadratures of the COM mode. The two $^{40}Ca^{+}$ ions are trapped with trapping frequencies $\omega_{\mathrm{ax}} = (2\pi)$ 1.36 MHz axially and $\omega_{\mathrm{rad}} = (2\pi)$ 3 MHz radially.

9.3.3 Measurements

With appropriately set phases the interaction Hamiltonian is given by $e\phi_1 = g\sigma_x^{(2)}\hat{x}$ with $g = \hbar\eta\tilde{\Omega}_2/\Delta$ [159]. Here, $\tilde{\Omega}_2$ is the Rabi frequency of the second bichromatic light field and $\hat{x} = (a^\dagger + a)\Delta$ is the position operator. When ion 2 is prepared in an eigenstate of $\sigma_x^{(2)}$ this operator can be replaced by its $+1$ eigenvalue, reducing the interaction to a linear potential and $\Gamma = \Omega_1^2/(4\eta^2\tilde{\Omega}_1\tilde{\Omega}_2)$.

Again, the spatial probability distribution is reconstructed with the wave function reconstruction method described in Sec. 4.5 and the previous chapter. As in the quantum walk, the reconstruction axis is along x. In contrast to the quantum walk, the measured states generally posses kinetic energy. Although it does not account for the kinetic energy, the approximate Hamiltonian H_{disp} of Eq. (4.27) was used in the reconstruction method. This is justifiable as the produced states usually show a larger spread along x than p. As the Hamiltonian allows us to account at least partially for higher order effects, it is still better suited than a Hamiltonian using the Lamb-Dicke approximation.

For spinors with high momentum, it is also possible to obtain the wave packets associated with positive and negative energy separately. In these cases the internal spinor states are not entangled with the motional state, and are given by the states $\binom{1}{\pm 1}_1$. A $\pi/2$-pulse can be used to map either of these energy states to $\binom{1}{0}_1$ after which a short (200 μs) projective fluorescence measurement is done. Since the state $\binom{1}{0}_1$ scatters no photons during fluorescence detection, the motional state of the ions remains intact and

Tab. 9.1: Tunneling probability for different slopes shown in Fig. 9.5. The ideal column is obtained by the Landau-Zener formula. The numerical simulations are closer to the measured tunnel rates as they account for the input state.

subfigure	$\tilde{\Omega}_2/2\pi$ (kHz)	P_{tunnel} ideal	P_{tunnel} numerical simulation	P_{tunnel} measured
a	0	0.00	0.00	0.017(7)
b	22	0.03	0.07	0.10(1)
c	50	0.21	0.22	0.32(2)
d	76	0.36	0.39	0.45(3)

can be analyzed afterwards. The cases where ion 1 is found in $\binom{0}{1}_1$ are discarded.

At the start of each experiment, laser cooling, optical pumping and coherent laser pulses, in a magnetic field of 6 G, prepare the ions in the axial center-of-mass mode ground state and internal states $\frac{1}{\sqrt{2}}\binom{1}{1}_1$ and $\frac{1}{\sqrt{2}}\binom{1}{1}_2$ (see Fig. 9.4.). We create an initial spinor state corresponding to a particle with $\langle\hat{x}\rangle = 0$ and $p_0 = \langle\hat{p}\rangle = 3.5\hbar/\Delta$ by a displacement along the momentum quadrature. The generated spinor,

$$\psi(x;t=0) \propto e^{ip_0x/\hbar}e^{-\frac{x^2}{4\Delta^2}}\binom{1}{1}_1, \tag{9.18}$$

is comprised largely of positive energy: $|\langle\psi(x;t=0)|P^+|\psi(x;t=0)\rangle|^2 > 0.98$, where P^+ is the projector onto the positive energy state (see Eq. (9.9)). The rest mass energy is set to $\hbar\Omega_1 = \hbar\,(2\pi)$ 1.3 kHz and $\tilde{\Omega}_1 = (2\pi)$ 17.5 kHz corresponding to an equivalent speed of light of $c \sim 0.01\Delta/\mu$s. Fig. 9.5 shows the scattering for different slope gradients (g). The corresponding numerical values are listed in Tab. 9.1.

The expectation values $\langle\hat{x}\rangle$ for the four slopes are shown in Fig. 9.6. In the case of no slope, the particle moves with constant velocity. For the other cases, the steepness of the slope determines the fraction of the inital wave packet that will tunnel through the potential. As can be seen in the figure, not only does the movement of $\langle\hat{x}\rangle$ change sign in the presence of the potential, but the speed is modified depending on how big the tunneling fraction is.

We are also able to create approximately quadratic electric potentials which, due to Klein tunneling, are non-confining in the relativistic limit [153]. The quadratic potential is implemented experimentally by detuning the bichromatic beam on ion 2 by $2\Omega_2$, so that the coupling between this ion and the vibrational mode becomes $\hbar\eta\tilde{\Omega}_2\sigma_x^{(2)}\hat{x}/\Delta + \hbar\Omega_2\sigma_z^{(2)}$. In the limit of a large detuning, $\Omega_2 \gg \eta\tilde{\Omega}_2$ the effective interaction Hamiltonian becomes $e\phi_2 = q\sigma_z^{(2)}\hat{x}^2$ with $q = \hbar\eta^2\tilde{\Omega}_2^2/(2\Delta^2\Omega_2)$ [159]. Preparing ion 2 in the $+1$ eigenstate of σ_z this reduces to a quadratic electric potential.

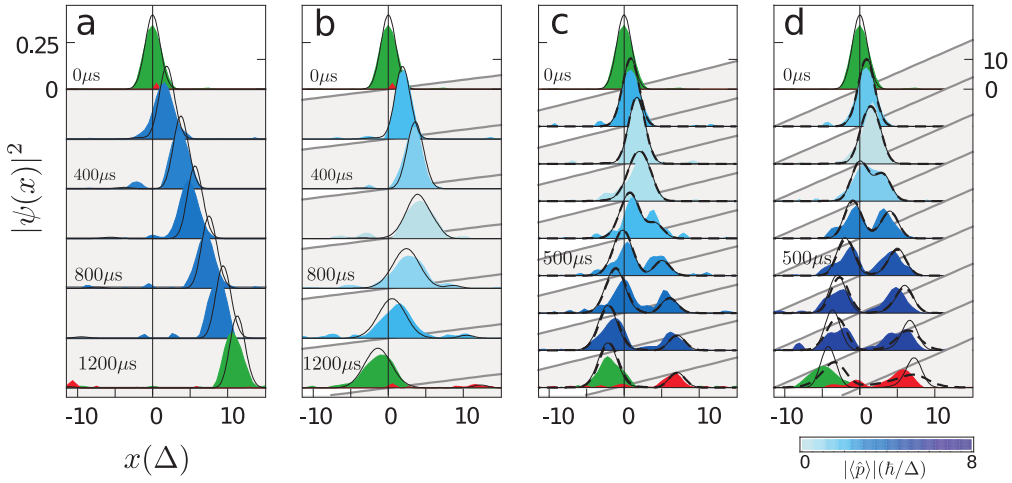

Fig. 9.5: Quantum simulation of relativistic scattering for linear potentials. Measured particle wave packets (filled curves) are compared with ideal predictions (solid black lines) and predictions taking corrections to the Lamb-Dicke approximation into account (dashed black lines). In the first and last frames of each sequence the positive (green) and negative (red) energy components are reconstructed separately. The blue color scale of these panels represents the measured expectation value of momentum. The axis on the right shows the potential energy in units of initial kinetic energy. Without a potential, the particle moves to the right with constant velocity (a). For a shallow potential gradient, the particle is almost completely reflected (b) and for steeper gradients (c,d) part of the wave packet propagates into the repulsive potential via Klein tunneling.

Fig. 9.7 shows results from our investigation of quadratic potentials. The first sequence (a) shows a particle, with initially positive energy, $\langle\hat{x}\rangle = 0$ and $\langle\hat{p}\rangle = 0$, evolving as a free particle ($\tilde{\Omega}_2 = 0$). As expected, the wave packet simply disperses. Sequence (b) shows the same initial state evolving under a quadratic potential generated by setting $\Omega_2 = (2\pi)\ 33$ kHz and $\tilde{\Omega}_2 = (2\pi)\ 50$ kHz, such that $\eta\tilde{\Omega}_2/\Omega_2 = 0.067 \ll 1$ and $q = (2\pi)\ 73\ \text{Hz}\ \hbar/\Delta^2$. The dynamic is clearly different in this case: the wave packet is still unconfined, due to Klein tunneling, but it spreads more slowly. Sequence (c) shows results for the same potential, but for a positive energy particle with an initial momentum $\langle\hat{p}\rangle = 0.23\ \hbar/\Delta$. The scattering dynamics in this case correspond to that of a quantum relativistic mass on a spring that is given a small initial kick and show Klein tunneling at each turning point.

The state used for the simulations in Fig. 9.7 (a) & (b) was created by applying a

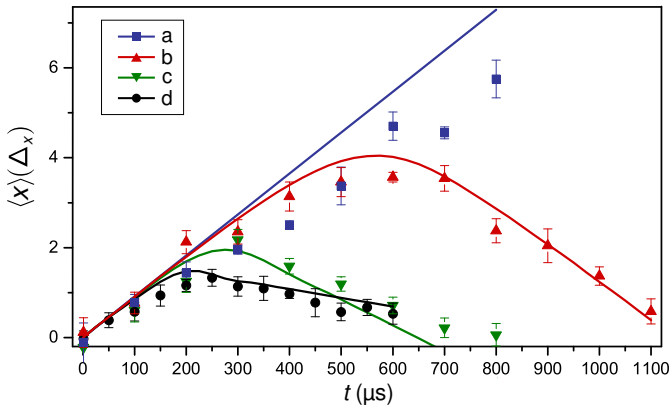

Fig. 9.6: $\langle\hat{x}\rangle$ for the four different slopes. The solid lines are obtained from simulations. The legend indicates the corresponding cases in Tab. 9.1 and Fig. 9.5. The blue data shows the simple translation of the wave packet without any slope. In the case of the red data set, the wave packet is almost perfectly reflected, which can be seen from the fact that the positive and the negative gradient of the curve are the same. The last two cases (green and black) show a partial transmission. This is best visible in the last case (black) where the curve not only differs in sign but also shows a different gradient after the turning/scattering point.

bichromatic displacement operation to ion 1 of the form $U_{\text{prep}_2} = e^{-iH_{\text{prep}_2}t/\hbar}$ with

$$H_{\text{prep}_2} = \hbar\eta\Omega_{\text{prep}_2}\hat{x}\sigma_x^{(1)}/\Delta \tag{9.19}$$

and ion 1 prepared in the internal state $\binom{1}{0}_2$. A 16 µs pulse with $\Omega_{\text{prep}_2} = (2\pi)$ 83 kHz produces a spinor with $\langle\hat{p}\rangle = 0$ and $|\langle\psi(x;t=0)|P^+|\psi(x;t=0)\rangle|^2 > 0.98$. The state used in Fig. 9.7 (c) was created in a similar way, but an additional pulse was used to give the state a momentum of $\langle\hat{p}\rangle = 0.23\ \hbar/\Delta$.

During setup of the experiments, various measures were taken to determine experimental parameters such as phase settings between the laser pulses. For example, all pulses were set up at a fixed position in the line cycle to ensure the same magnetic field for different experiments. Also both bichromatic light fields were switched on, even if only one of them was scanned for a particular parameter, to account for possible AC-Stark shifts caused by the other bichromatic light field. Looking for a maximum in the simulation, such as momentum at the end of the simulation, generally worked well as a method to find experimental parameters as in these cases errors can only reduce the signal.

There are a number of errors that reduce the quality of our quantum simulations. The internal state coherence time for the ions is about 3 ms, limited by magnetic field

fluctuations, while the whole simulation takes up to 1.5 ms. The motional coherence is limited by slow drifts, which can change the trap frequency by about about 25 Hz. Both effects cause broadening of the wave packets, whereas systematic errors in state preparation due to slowly varying experimental settings can cause additional structure in the reconstructed data. For the steepest slope, states of more than 150 phonons on average were created, for which the Lamb-Dicke approximation starts to fail. This changes the simulated Hamiltonian somewhat, while also affecting the reconstruction (see Sec. 4.5).

These error sources can be addressed by the same technical improvements that have been presented in the last two paragraphs of the previous chapter.

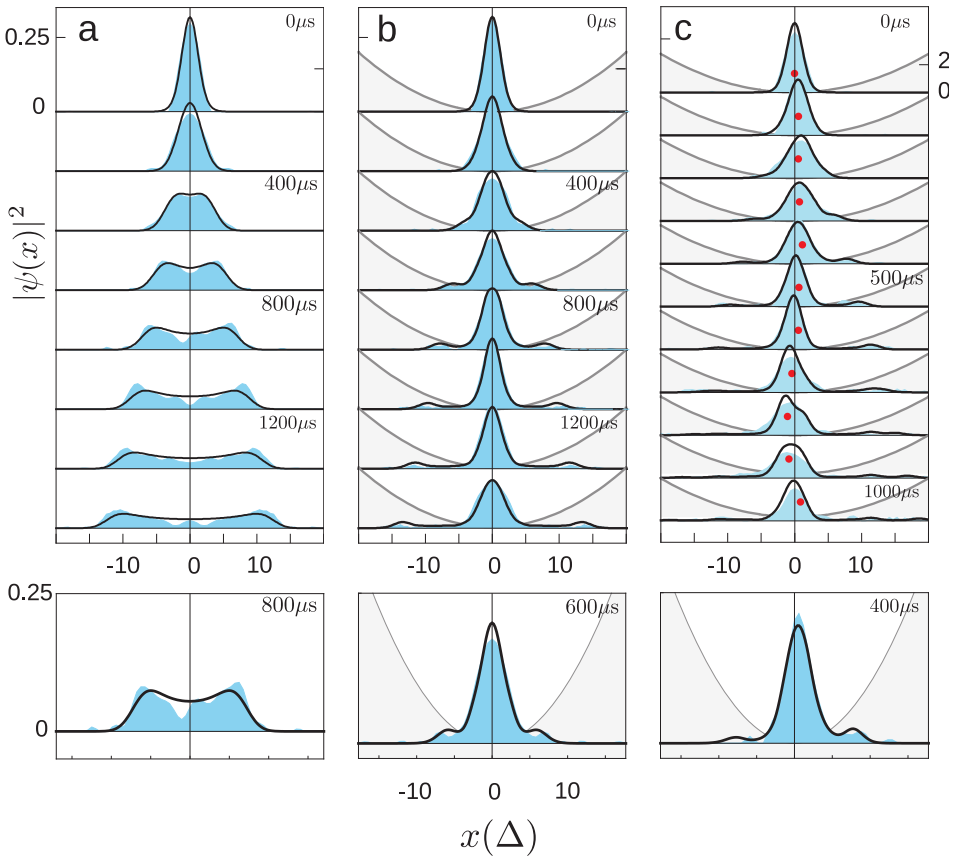

Fig. 9.7: Quantum simulation of scattering for quadratic potentials. Measured particle wave packets (filled curves) are compared with theoretical predictions (black lines) for quadratic potentials. The particle's rest mass energy is set to $\hbar\Omega_1 = \hbar\,(2\pi)$ 0.65 kHz. In (a) & (b) the initial state has almost purely positive energy, and momentum $\langle\hat{p}\rangle = 0\hbar/\Delta$. Without a potential (a) the wave packet diffuses. With the potential switched on (b) the spreading is significantly restricted, but can continue through Klein tunneling. In (c) the initial state has a small momentum $\langle\hat{p}\rangle = 0.23\hbar/\Delta$ and the wave packet oscillates. The red dots represent $\langle\hat{x}\rangle$. The lower three figures show larger versions of some of the wave packets. The axis on the right is in the same units as in Fig. 9.5.

10 Summary and outlook

The main results of this thesis show three different aspects of quantum optics with trapped ions: spectroscopy, quantum information processing and quantum simulation. The experiments presented demonstrate the versatile use of procedures that are developed and used for quantum information processing with ions—in this case with $^{40}Ca^{+}$.

A new spectroscopic method of repetitive laser pulses was employed to measure the branching ratio of the $4s^2P_{3/2}$ level with high precision. After the ion is prepared in the electronic ground state, the population is pumped to the target state, and the ratio between the decay channels is measured by observing the population that ends up in the lower-lying energy levels. Because the electronic population is pumped to the excited state several times, the precision of this measurement is further enhanced. The branching fractions into the $4s^2S_{1/2}$, $3d^2D_{5/2}$ and $3d^2D_{3/2}$ levels are found to be 0.9347(3), 0.0587(2) and 0.00661(4), respectively. For the branching ratio $A(P_{3/2}-S_{1/2})/\sum_J A(P_{3/2}-D_J) = 14.31(5)$ the results are a forty-fold improvement in accuracy, as compared to the best previous measurement [89]. The method is also applicable to other ion species that share a similar level structure.

In addition to fluorescence and repump lasers, our experimental setup includes a ultra-stable narrow linewidth laser used to realize a qubit between the $S_{1/2}$ ground state and the meta-stable $D_{5/2}$ level. Previously, a high-fidelity gate operation was demonstrated with this laser [37, 55]. To this end, the light is used in a bichromatic, co-propagating configuration, where the frequency is detuned slightly in opposite directions from the motional sidebands of the ion in the harmonic trap potential [53, 54].

On the other hand, if the detuning is set in the same direction, the resulting Hamiltonian resembles that of the Dirac equation in 1+1 dimensions. This quantum simulation was also previously demonstrated in our experiment [45].

Another possibility is to set both frequencies on resonance with the motional sidebands. Applying these two light fields to a trapped ion realizes a state-dependent displacement operator [74]. This operation is used for a quantum walk on a line in phase space with one and two ions. In contrast to its classical counterpart, the random walk, the quantum walk is performed by a two-level quantum system that is shifted in posi-

tion by a state-dependent displacement operator. The equivalent to the coin-flip is a unitary operation that puts the internal state into a superposition. Performing both operations in an alternating fashion realizes the quantum walk, in the course of which the walker will interfere with himself. This interference gives rise to features that are quite different compared to the classical random walk. These features can be used for certain algorithms in quantum information processing.

In our experiment, the quantum walk with up to 23 steps was performed and the resulting possibility distribution of the wave function was visualized with a measurement procedure also involving the state-dependent displacement operator. Various measurements are presented to highlight the differences of the quantum walk to the classical random walk.

The quantum simulation of the Dirac equation was extended by adding a second ion and an additional bichromatic light field in order to simulate potentials. The second light field was coupled to a different transition in the second ion but to the same vibrational mode as the first one. By choosing suitable parameters for the second light field, a linear and a quadratic potential were realized.

In its original version, the Klein-Paradox was presented for a step-shaped potential barrier [150]. If the barrier has a certain height, the relativistic particle can tunnel into the classically forbidden region by turning into its own anti-particle. A similar effect can be observed for the potentials that can be realized with a second ion. The reconstruction of the wave function in phase space was used to visualize the scattering processes "frame-by-frame".

These last two experiments, the quantum walk and the quantum simulation of a relativistic particle, demonstrate how the bichromatic light field can achieve a high level of control over the ion's motional state. Employed in the presented reconstruction method, the bichromatic light field also allows one to read out the motional state of the ion with high fidelity. This application is very attractive in the context of quantum information processing and quantum simulation, as the motional state of the ion can be utilized to hold information or represent observables.

Spectroscopy can also benefit from this versatile tool, as it allows the creation of non-classical states which find application in quantum metrology [161]. With their greater sensitivity, these states enhance spectroscopic measurements, making this is a possible direction of future research.

For the new trap with its improved vacuum conditions that will be presented in the next chapter, certain quantum simulations are within reach in the near future. Among these are the Dirac equation in 2+1 dimensions [143], the simulation of the Majorana

equation [162] or even quantum field theory [163]. Further quantum simulations have been proposed for trapped ions [164]. Some examples are spin models [165], spin boson models [166], the Unruh effect [167, 168], cosmological particle creation [169] and the Frenkel-Kontorova model [170].

Broadly speaking, for the field of experimental quantum simulation, the next big step is the demonstration of a quantum simulation that is challenging for a classical computer. In order to achieve this goal, two major aspects need to be addressed. The first is that the performed simulation has to be able to estimate the experimental errors. This information is essential in order to assess the results. The other aspect is improvement in experimental control. The already impressive control over quantum systems has to increase further, which in many cases can be achieved through technological development.

In the case of trapped ions, improvements in trap parameters and laser stability, both in frequency and in intensity, are necessary. Another important step that has proven challenging is scaling up to several tens of ions. Toward this purpose, micro-fabricated traps [171–176] and quantum networks [177, 178] are currently under investigation, but additionally the number of available laser beams has to be scaled up without compromising their performance.

Once accomplished, these steps will advance not only quantum simulations but also quantum information processing as well as spectroscopy with trapped ions.

A New trap setup with high vacuum demands

In parallel to the experiments presented in this thesis, a new vacuum vessel with a new trap was set up. Although the vacuum vessel described in chapter 5 served us well in the past, vacuum conditions are a limiting factor. Especially experiments with ion strings on the order of ten ions demand very high vacuum quality. Simple background gas collisions alone can render experimenting challenging or even impossible if they happen too often. With better vacuum quality and a slightly improved trap design the new setup offers new experimental options.

The first part of this chapter describes the new trap design that was chosen as a successor to the previous one. The second part deals with the investigation of the achieved vacuum.

A.1 The new trap design

As the ion-trap design described in chapter 5 showed very good properties in general, it was only slightly modified. The first modification affects the overall size. The heating rate of ion traps increases as the distance between electrodes and ions becomes smaller. Conversely, smaller traps allow for higher trapping frequencies. Since the heating rate has a power law dependence on the distance [179], the size was reduced by only a factor of $\sqrt{2}$.

A second modification concerns the tips: the new design has holes that allow beams to be directed along the trap axis. In this way, light can be shone on the ions without laser power limitations due to widening of the beam.

The new trap can be seen in Fig. A.1. The smaller design made changes to the mounting of the blades and the tips necessary. The redesign required us to manufacture the trap more precisely. It also necessitated a sturdier mounting in order to keep the blades aligned, especially during bakeout. As an additional feature, the DC blades of the trap are not grounded, but connected to the outside of the vacuum vessel to apply an

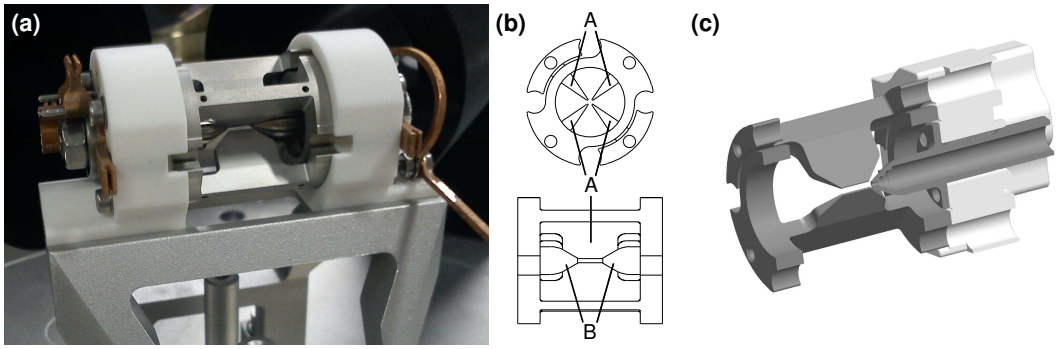

Fig. A.1: **(a)** Photograph of the new trap. All electrical connections go through the Macor blocks holding the blades and tips. **(b)** Schematic drawing of the trap. The distance between two opposing blades (A) is 1.13 mm. The tips (B) are separated by 4.5 mm, which is not exactly a factor of $\sqrt{2}$ smaller than the separation of the predecessor in order to account for the holes. The compensation electrodes have been omitted in this figure. **(c)** Three dimensional drawing of a sliced trap. The ring structure of the blade mounting allows for a precise alignment. The tip has a tapered hole with a diameter of 0.5 mm. The left tip and left Macor piece have been omitted for better visualization.

offset voltage to the DC blades. In this way, the splitting of the radial trap frequencies can be adjusted.

During the course of our investigation of the vacuum quality, several traps of this type were tested. The measured properties varied only slightly, demonstrating the reproducibility of the design regarding the assembly and alignment process.

For the axial trap frequencies a value of around 1.2 MHz was found if both tips are set to 1000 V. The helical resonator is designed to drive the trap at 30 MHz. Driven with 5 W the resulting radial trap frequencies are around 3.2 MHz. If the DC blades are set to ground, the two radial trap frequencies are degenerate preventing Doppler cooling from working properly. To overcome this problem, typically 3 V are applied to the DC blades, resulting in a splitting of about 180 kHz. After Doppler cooling an average phonon number of $\bar{n} = 12(2)$ was found. However, once the splitting is big enough for Doppler cooling to work properly, the reached average phonon number does not depend noticeably on the voltage applied to the DC blades.

The heating rate was also investigated and measured to be around 16 phonons per second. This number is almost a factor of four higher than for the predecessor, but still offers good working conditions.

The trap has two pairs of electrodes to compensate for excess micromotion [80]. A

good supression of excess micromotion is desirable. The stronger the micromotional sideband is, the easier it is for the fluorescence laser to excite a motional sideband of that micromotional sideband. If the motional sideband is a blue sideband, this has a negative effect on Doppler cooling. The coupling of the quadrupole laser is also negatively affected by excess micromotion, as this reduces the coupling strength on the carrier transition [77].

Typical voltages used with these electrodes are between -80 to +80 V. Usually, the achieved micromotion compensation is given by comparison of the Rabi frequencies of the carrier and the first micromotional sideband. For the first tested traps the achievable suppression in the radial directions was between 30:1 and 70:1. However, inspection, after they had been removed from the vacuum vessel, revealed damaged Macor holders.

This damage can explain why the supression rates were not as good as in the old trap. Excess micromotion can also be caused by tilting of the trap electrodes with respect to the other electrodes and this cannot be canceled by the compensation electrodes. As the trap is designed for an assembly with very high accuracy, damaged Macor holders indicate a deviation from this accurate alignment. By looking at the best achievable suppression rate of excess micromotion, conclusions about the actual alignment of the trap can be drawn.

The damage was probably caused by too small manufacturing tolerances for the Macor pieces that led to damages during bake out, since Macor has a considerably smaller expansion coefficient than steel. The axial micromotion was measured to be 190:1 and, in the case of a severely damaged trap, 13:1. The currently installed trap has Macor holders with slightly higher tolerances, and here the suppression was measured to be better than 100:1 in all directions. From this we conclude that the slightly higher manufacturing tolerances avoid damage to trap parts during bake out, resulting in a better alignment of the trap electrodes.

Altogether, the trap design performed very close to the properties predicted by calculations and computer simulations.

A.2 Investigating vacuum quality

Achieving a very low pressure ($< 10^{-11}$ mbar) at the location of the ions can be difficult. The new setup consists of the same vacuum vessel and components as the old setup, and only the trap has been replaced.

After an airbake of most components, the setup was baked under vacuum at 300 °C without windows and the trap. As these parts cannot withstand temperatures over

200 °C, they were built in later, and then baked with the entire chamber under vacuum at 180 °C for several days. All parts were cleaned with several solvents before the entire assembly was integrated.

Unfortunately, the new setup also had vacuum conditions that were not suitable for measurements with long ion strings.

A.2.1 Types of vacuum problems

The vacuum problems observed in the new setup can be divided in three categories.

Background gas collisions Collisions with background gas disturb measurements, as they can change the internal state of the ion or melt the ion crystal. The collision rate depends on the local pressure at the position of the ions. In cases when the crystal melts, the measurement has to be repeated, which can be automated. As these collisions will always be present, the important parameter is, how often they occur. For our purposes, the string should not melt more often than every ten minutes, as the automated refreezing feature requires the RF power into the trap to be reduced. This change of the drive power requires a rethermalization of the trap until measurements can continue. For a ten-ion crystal this translates into a local pressure requirement of $\approx 10^{-11}$ mbar.

Chemical reactions Another more problematic condition is the possibility for chemical reactions of the ions with background gas. In this case, the ions form molecules with the background gas that can no longer be excited by the lasers and appear as "dark" ions on the camera, meaning that the position in the ion string appearss unoccupied. Several mass spectroscopic measurements of these "dark" ions were always consistent with a mass of 57 u. This mass points to the laser-assisted reaction with water

$$\mathrm{Ca}^{+*}(\mathrm{D}_J) + \mathrm{H_2O} \rightarrow \mathrm{Ca}^{+}(\mathrm{H_2O}^{*}) \rightarrow \mathrm{HCaOH}^{+} \rightarrow \mathrm{CaOH}^{+} + \mathrm{H}$$

investigated in Ref. [180].

Unwanted trapping of other ion species It was also observed that unwanted ion species randomly enter the trap. These ions also appear as dark on the camera. Spectroscopy on these ions revealed the masses 41 u, 57 u and 71 u associated with this phenomenon. While the first two have a high probability of being calcium molecules, namely CaH^{+} and CaOH^{+}, we can only speculate about the third species. Generally this problem is not as severe as the one described above, since

these are extra ions and the measurement can continue once they are removed from the trap. However, the removal requires a large enough mass difference and will disrupt the running measurement.

The first two conditions are, to various extents, present in all ion trap setups using $^{40}Ca^{+}$ in our group. However, the last phenomenon was only observed with traps that had been heated to more than 400 °C under vacuum prior to assembly. This procedure was introduced in order to further eliminate contamination from the trap, as it is closest to the ions. Both a reduced background gas collision rate and fewer chemical reactions were observed for these traps.

A.2.2 Characterization and investigation methods

In order to address the phenomena listed above, we characterized them using available tools in the lab. These methods will be described in this section.

Observation with camera

All three types of vacuum problems can be investigated with an EMCCD camera:

A longer string of ten to twenty ions is loaded into the trap with weak confinement ($\omega_{\mathrm{rad}} \approx (2\pi)$ 2 MHz and $\omega_{\mathrm{axial}} \approx (2\pi)$ 210 kHz) and observed over a period of several hours. The chosen trap parameters allow longer ion strings to recrystallize easily, but dark ions are still stably trapped and show up in the string. Using many ions has several advantages. Many ions can sympathetically cool present dark ions, allowing for longer observation times with many dark ions. In this way, also more partners for the chemical reaction with water or for normal collisions with background gas are provided.

The collision rate can be easily observed given that the string of ions contains at least one dark ion. In this case collisions show up as position changes of the dark ion(s) within the crystal.

Investigation of "dark" ions by mass spectroscopy

It is of interest to determine the "dark" ions' masses in order to draw conclusions about the origin of the problem.

This information can be obtained by applying a small perturbation RF of the form $V_{\mathrm{tickle}} \sin \omega t$ on one of the compensation electrodes. If ω is resonant with the transverse trap frequency of one of the ions, this ion gets excited, resulting in a melting of the ion crystal. This melting can be observed as a dip in the fluorescence seen by the PMT or directly with the camera.

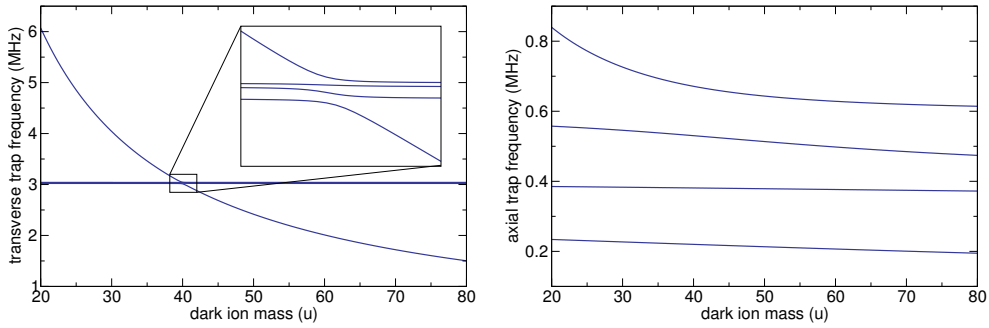

Fig. A.2: Calculated mass dependency of the transverse and axial oscillation frequencies of a four ion string with one ion of variable mass. The trap parameters are the same as those used in the experiment. The inset in the left plot shows the avoided crossing and the four different frequencies which are not visible in the main plot. Comparing the left plot (transverse trap frequencies) to the right plot (axial trap frequencies), it can be seen that the transverse trap frequencies are better suited to infer the mass of the other ion as the relative change of the frequencies is much more pronounced for the transverse trap frequencies. The general pattern of both plots does not change significantly if higher axial trap frequencies are used.

This method has little technical overhead and is well suited for our experimental conditions: in case of a very weak axial and a strong radial confinement, the transversal oscillation frequencies of the ion crystal are almost completely decoupled. Therefore, the ions oscillate at a frequency very close to their bare resonance frequency, allowing for a mass resolution of about 0.2 u. The mass dependency between axial and radial trap frequencies is compared in Fig. A.2. The frequencies were calculated using the formulas given in [181], which have been slightly modified for the case of different ion masses.

Applying UV light to the trap electrodes

By illuminating the electrodes of the trap with UV light, we were able to show that the phenomenon of unwanted additional ion species in the trap was a surface effect on the trap; probably caused by the bake out of the trap at 400 °C in combination with calcium contamination of the trap surface by the oven. A photoelectric effect was confirmed, indicating an acceleration of free electrons by the trap's RF which in turn caused molecules to be ejected from the surface.

The trapping of unwanted ion species stopped after a 20 mW laser at 375 nm was applied to the electrodes overnight. However, from the subsequent observations it is not clear if this procedure does not have unwanted side effects, i.e., forming additional water close to the trap.

Heating separate parts of the vacuum vessel

It is also important to know whether the vacuum problems observed at the ions are local or present in the entire chamber. A local problem was suspected as only the trap and the oven are manufactured in-house and all other components are specified for ultra high vacuum (UHV) by their respective manufacturer. This hypothesis was tested by shining a 5 W laser[1] onto the trap and then loading and observing ions. The same procedure was then repeated, but this time the laser was aimed at the walls of the chamber with a comparably large separation from the ions. In both cases, the rate of the chemical reaction with water increased by a factor of more than 40, while the rate of background collisions only slightly increased. This finding indicated a contamination of the entire chamber with water.

A.3 Summary

As a result of these investigations, a complete reassembly of the vacuum vessel was decided upon and has significantly reduced the problems with background collisions and chemical reactions. This reassembly included several precautious procedures and changes to the setup. Notable among these is that, the last cleaning step of the vacuum parts was done with demineralized water, which was confirmed with a residual gas analyzer to improve overall vacuum quality. Interestingly, the omission of a high temperature bake at 300 °C prior to full assembly did not negatively affect the achieved vacuum quality.

Nevertheless, the lack of a systematic investigation makes it impossible to draw resilient conclusions. With the long manufacturing and bake-out times in mind such an investigation would be justified if the problems described hinder other setups as well.

On the other hand, the new trap design was thoroughly investigated and performed as expected. Except for the expected increase of the heating rate, the trap performed equal or better than the "Innsbruck standard." As the heating rate can still be considered very low, the new design represents a good candidate for future setups.

[1] Verdi V-10, 532 nm

B Lower bound on the kinetic energy of mixed quantum states

The constraint for the kinetic energy of a pure state (as given in Eq. (8.9))

$$\langle\frac{\hat{p}^2}{2m}\rangle \geq \frac{\hbar^2}{8m}\int_{-\infty}^{\infty}\mathrm{d}x\frac{p'(x)^2}{p(x)} \tag{B.1}$$

is convex. Any function of the type $\frac{f(x)^2}{g(x)}$ with $g(x) > 0$ is convex and therefore the integral above is also convex. Since $p(x)$ is a probability distribution of a quantum state, the condition $p(x) > 0$ is fulfilled.

In order to show that inequality (B.1) is also valid for mixed states, we treat the probability distribution $p(x)$ as being composed out of several probability distributions $p(x) = \sum_i \lambda_i p_i(x)$.

Analogue to a pure state the calculation for a mixed state $\varrho = \sum_i \lambda_i|\psi_i\rangle\langle\psi_i|$ should give

$$\begin{aligned}\langle\frac{p^2}{2m}\rangle &= \sum_i \lambda_i\langle\psi_i|\frac{p^2}{2m}|\psi_i\rangle &\text{(B.2)}\\ &\geq \frac{\hbar^2}{2m}\sum_i\lambda_i\int_{-\infty}^{\infty}\mathrm{d}xA_i'(x)^2 = \frac{\hbar^2}{8m}\sum_i\lambda_i\int_{-\infty}^{\infty}\mathrm{d}x\frac{p_i'(x)^2}{p_i(x)} &\text{(B.3)}\end{aligned}$$

In order to proof this lower bound on the kinetic energy for mixed quantum states, it is sufficient to show that

$$\frac{\hbar^2}{8m}\sum_i\lambda_i\int_{-\infty}^{\infty}\mathrm{d}x\frac{p_i'(x)^2}{p_i(x)} \geq \frac{\hbar^2}{8m}\int_{-\infty}^{\infty}\mathrm{d}x\frac{p'(x)^2}{p(x)}. \tag{B.4}$$

If inequality (B.4) is valid for any interval δx then it must also be valid in its integral form.

For the proof we use the following inequality, which is true for any two probability distributions $p_i(x)$ and $p_k(x)$ and their derivatives

$$\begin{aligned}\left(p_i'(x)p_k(x) - p_k'(x)p_i(x)\right)^2 &\geq 0 &\text{(B.5)}\\ p_i'(x)^2p_k(x)^2 + p_k'(x)^2p_i(x)^2 &\geq 2p_i'(x)p_k'(x)p_i(x)p_k(x). &\text{(B.6)}\end{aligned}$$

Since we have $1 \geq \lambda_j \geq 0$ (with $\sum_j \lambda_j = 1$) and $1 \geq p_j(x) > 0$, we can rewrite the last expression as

$$\lambda_i \lambda_k \left(\frac{p_i'(x)^2}{p_i(x)} p_k(x) + \frac{p_k'(x)^2}{p_k(x)} p_i(x) \right) \geq 2\lambda_i \lambda_k p_i'(x) p_k'(x). \tag{B.7}$$

This inequality still holds if we extent it to an arbitrary number of probability distributions. Therefore we have

$$\sum_{ik} \lambda_i \lambda_k \frac{p_i'(x)^2}{p_i(x)} p_k(x) \geq \sum_{ik} \lambda_i \lambda_k p_i'(x) p_k'(x) \tag{B.8}$$

$$\left(\sum_i \lambda_i \frac{p_i'(x)^2}{p_i(x)} \right) \left(\sum_k \lambda_k p_k(x) \right) \geq \left(\sum_i \lambda_i p_i'(x) \right) \left(\sum_k \lambda_k p_k'(x) \right) \tag{B.9}$$

$$\sum_i \lambda_i \frac{p_i'(x)^2}{p_i(x)} \geq \frac{\left(\sum_i \lambda_i p_i'(x)\right) \left(\sum_k \lambda_k p_k'(x)\right)}{\left(\sum_k \lambda_k p_k(x)\right)} \tag{B.10}$$

$$\sum_i \lambda_i \frac{p_i'(x)^2}{p_i(x)} \geq \frac{p'(x)^2}{p(x)} \quad \square \tag{B.11}$$

With Eq. (B.4) proven, we have shown that the lower bound on the kinetic energy in Eq. (8.9) is also valid for mixed quantum states.

C Physical properties of $^{40}Ca^{+}$

speed of light	c	299 792 458 m/s (exact)
permeability of vacuum	μ_0	$4\ \pi \cdot 10^{7}$ (exact)
permittivity of vacuum	ϵ_0	$1/(\mu_0 c^2)$ (exact)
Planck's constant	$h = 2\pi\hbar$	$6.626\ 069\ 57(29)\ \cdot 10^{-34}$ J s
elementary charge	e	$1.602\ 176\ 565(35)\ \cdot 10^{-19}$ C
Bohr magneton	μ_B	$927.400\ 968(20)\ \cdot 10^{-26}$ J T^{-1}
atomic mass unit	u	$1.660\ 538\ 921(73) \cdot 10^{-27}$ kg

Tab. C.1: Fundamental physical constants relevant to the experiment (2010 CODATA recommended values).

transition	λ_{air}(nm)	reference
$4\ S_{1/2} \leftrightarrow 3D_{5/2}$	411 042 129 776 393.3(1.0) Hz	[77, 182, 183]
$4\ S_{1/2} \leftrightarrow 3D_{3/2}$	732.389	[184]
$4\ S_{1/2} \leftrightarrow 4P_{1/2}$	396.847	[184]
$4\ S_{1/2} \leftrightarrow 4P_{3/2}$	393.366	[184]
$3\ P_{1/2} \leftrightarrow 3D_{3/2}$	866.214	[185]
$3\ P_{3/2} \leftrightarrow 3D_{3/2}$	849.802	[185]
$3\ P_{3/2} \leftrightarrow 3D_{5/2}$	854.209	[185]

Tab. C.2: $^{40}Ca^{+}$ wavelength in air (λ_{air}). The transition frequency for $4\ S_{1/2} \leftrightarrow 3D_{5/2}$ is given in Hz.

quantity	value	reference
life time $3\ D_{3/2}$	1.20(1) s	[62]
life time $3\ D_{5/2}$	1.168(7) s	[62]
life time $4\ P_{1/2}$	7.098(20) ns	[63]
life time $4\ P_{3/2}$	6.924(19) ns	[63]
$g_j(4S_{1/2})$	2.00225664(9)	[186]
$g_j(3D_{5/2})$	1.200 334 0(3)	[182, 183]

Tab. C.3: Atomic properties of calcium.

m'	-3/2	-1/2	1/2	3/2	5/2
coefficient	$\sqrt{1/5}$	$\sqrt{2/5}$	$\sqrt{3/5}$	$\sqrt{4/5}$	1

Tab. C.4: Clebsch-Gordan Coefficients for the $^{40}Ca^{+}$ quadrupole transition $S_{1/2}, m = 1/2 \rightarrow D_{5/2}, m'$. The coupling strengths for $S_{1/2}, m = -1/2 \rightarrow D_{5/2}, m'$ can be derived by exchanging $m'_j \rightarrow -m'_j$.

D Journal publications

The experiments presented in this thesis gave rise to the following publications:

1. "Precision measurement of the branching fractions of the 4p $^2P_{3/2}$ decay of Ca II."
   R. Gerritsma, G. Kirchmair, **F. Zähringer**, J. Benhelm, R. Blatt & C. F. Roos
   Eur. Phys. J. D **50**, 13–19 (2008).

2. "Realization of a quantum walk with one and two trapped ions."
   F. Zähringer, G. Kirchmair, R. Gerritsma, E. Solano, R. Blatt & C. F. Roos
   Phys. Rev. Lett. **104**, 100503 (2010).

3. "Quantum simulation of the Klein paradox"
   R. Gerritsma, B. P. Lanyon, G. Kirchmair, **F. Zähringer**, C. Hempel, J. Casanova, J. J. Garcia-Ripoll, E. Solano, R. Blatt & C. F. Roos
   Phys. Rev. Lett. **106**, 060503 (2011).

Further articles have been published in the framework of this thesis:

4. "Deterministic entanglement of ions in thermal states of motion."
   G. Kirchmair, J. Benhelm, **F. Zähringer**, R. Gerritsma, C. F. Roos & R. Blatt
   New J. Phys., **11**, 023002 (2009).

5. "High-fidelity entanglement of $^{43}Ca^+$ hyperfine clock states."
   G. Kirchmair, J. Benhelm, **F. Zähringer**, R. Gerritsma, C. F. Roos & R. Blatt
   Phys. Rev. A, **79**, 020304 (2009).

6. "State-independent experimental test of quantum contextuality".
   G. Kirchmair, **F. Zähringer**, R. Gerritsma, M. Kleinmann, O. Gühne, A. Cabello, R. Blatt & C. F. Roos
   Nature **460**, 494-497 (2009).

7. "Deterministic reordering of $^{40}Ca^+$ ions in a linear segmented Paul trap"
   F. Splatt, M. Harlander, M. Brownnutt, **F. Zähringer**, R. Blatt & W. Hänsel
   New J. Phys., **11**, 103008 (2009).

8. "Quantum simulation of the Dirac equation."
   R. Gerritsma, G. Kirchmair, **F. Zähringer**, E. Solano, R. Blatt & C. F. Roos
   Nature **463,** 68-71 (2010).

9. "Compatibility and noncontextuality for sequential measurements."
   O. Gühne, M. Kleinmann, A. Cabello, J.-A. Larsson, G. Kirchmair, **F. Zähringer**, R. Gerritsma & C. F. Roos
   Phys. Rev. A **81**, 022121 (2010).

10. "Universal digital quantum simulation with trapped ions"
    B. P. Lanyon, C. Hempel, D. Nigg, M. Müller, R. Gerritsma, **F. Zähringer**, P. Schindler, J. T. Barreiro, M. Rambach, G. Kirchmair, M. Hennrich, P. Zoller, R. Blatt & C. F. Roos
    Science **334**, 57-61 (2011).

Bibliography

[1] R. Feynman. Simulating physics with computers. *Int. J. Theoret. Phys.* **21**, 467–488 (1982).

[2] P. W. Shor. Algorithms for quantum computation: discrete logarithms and factoring. In *Proceedings of the 35th Annual Symposium on Foundations of Computer Science*, 124–134 (IEEE Computer Society Press, Santa Fe, NM, 1994).

[3] L. K. Grover. A fast quantum mechanical algorithm for database search. *Proceedings of the 28th ACM STOC* , 212 (1996).

[4] A. Barenco, C. H. Bennett, R. Cleve, D. P. DiVincenzo, N. Margolus, P. Shor, T. Sleator, J. A. Smolin, and H. Weinfurter. Elementary gates for quantum computation. *Phys. Rev. A* **52**, 3457–3467 (1995).

[5] D. P. DiVincenzo. Two-bit gates are universal for quantum computation. *Phys. Rev. A* **51**, 1015–1022 (1995).

[6] S. Lloyd. Universal quantum simulators. *Science* **273**, 1073–1078 (1996).

[7] D. P. DiVincenzo. The physical implementation of quantum computation. *Fortschr. Phys.* **48**, 771–783 (2000).

[8] T. D. Ladd, F. Jelezko, R. Laflamme, Y. Nakamura, C. Monroe, and J. L. O'Brien. Quantum computers. *Nature* **464**, 45 – 53 (2010).

[9] N. A. Gershenfeld and I. L. Chuang. Bulk spin-resonance quantum computation. *Science* **275**, 350–356 (1997).

[10] Y. Makhlin, G. Schön, and A. Shnirman. Quantum-state engineering with Josephson-junction devices. *Rev. Mod. Phys.* **73**, 357–244 (2001).

[11] L. DiCarlo, J. M. Chow, J. M. Gambetta, L. S. Bishop, B. R. Johnson, D. I. Schuster, J. Majer, A. Blais, L. Frunzio, S. M. Girvinand, and R. J. Schoelkopf. Demonstration of two-qubit algorithms with a superconducting quantum processor. *Nature* **460**, 240–244 (2009).

[12] E. Knill, R. Laflamme, and G. J. Milburn. A scheme for efficient quantum computation with linear optics. *Nature* **409**, 46–52 (2001).

[13] A. Politi, J. C. F. Matthews, and J. L. O'Brien. Shor's quantum factoring algorithm on a photonic chip. *Science* **325**, 1221 (2009).

[14] J. R. Petta, A. C. Johnson, J. M. Taylor, E. A. Laird, A. Yacoby, M. D. Lukin, C. M. Marcus, M. P. Hanson, and A. C. Gossard. Coherent manipulation of coupled electron spins in semiconductor quantum dots. *Science* **309**, 2180–2184 (2005).

[15] I. Fushman, D. Englund, A. Faraon, N. Stoltz, P. Petroff, and J. Vuckovic. Controlled phase shifts with a single quantum dot. *Science* **320**, 769–772 (2008).

[16] H. J. Briegel, T. Calarco, D. Jaksch, J. Cirac, and P. Zoller. Quantum computing with neutral atoms. *J. Mod. Opt* **47**, 415–451 (2000).

[17] D. Schrader, I. Dotsenko, M. Khudaverdyan, Y. Miroshnychenko, A. Rauschenbeutel, and D. Meschede. Neutral atom quantum register. *Phys. Rev. Lett.* **92**, 150501 (2004).

[18] M. Anderlini, P. J. Lee, B. L. Brown, J. Sebby-Strabley, W. D. Phillips, and J. V. Porto. Controlled exchange interaction between pairs of neutral atoms in an optical lattice. *Nature* **448**, 452–456 (2007).

[19] D. Leibfried, R. Blatt, C. Monroe, and D. Wineland. Quantum dynamics of single trapped ions. *Rev. Mod. Phys.* **75**, 281–324 (2003).

[20] H. Häffner, C. Roos, and R. Blatt. Quantum computing with trapped ions. *Physics Reports* **469**, 155–203 (2008).

[21] D. J. Wineland and H. G. Dehmelt. Principles of the stored ion calorimeter. *J. App. Phys.* **46**, 919–930 (1975).

[22] D. J. Wineland, R. E. Drullinger, and F. L. Walls. Radiation-pressure cooling of bound resonant absorbers. *Phys. Rev. Lett.* **40**, 1639–1642 (1978).

[23] W. Neuhauser, M. Hohenstatt, P. E. Toschek, and H. Dehmelt. Localized visible Ba^+ mono-ion oscillator. *Phys. Rev. A* **22**, 1137–1140 (1980).

[24] D. Wineland, J. Bergquist, W. Itano, and R. Drullinger. Double-resonance and optical-pumping experiments on electromagnetically confined, laser-cooled ions. *Opt. Lett.* **5**, 245–247 (1980).

[25] W. Nagourney, J. Sandberg, and H. Dehmelt. Shelved optical electron amplifier: Observation of quantum jumps. *Phys. Rev. Lett.* **56**, 2797–2799 (1986).

[26] T. Sauter, W. Neuhauser, R. Blatt, and P. E. Toschek. Observation of quantum jumps. *Phys. Rev. Lett.* **57**, 1696–1698 (1986).

[27] J. C. Bergquist, R. G. Hulet, W. M. Itano, and D. J. Wineland. Observation of quantum jumps in a single atom. *Phys. Rev. Lett.* **57**, 1699–1702 (1986).

[28] J. J. Bollinger, D. J. Heinzen, W. M. Itano, S. L. Gilbert, and D. J. Wineland. A 303 MHz frequency standard based on trapped Be^+ ions. *IEEE Trans. Instr. Meas.* **40**, 126–128 (1991).

[29] J. I. Cirac and P. Zoller. Quantum computations with cold trapped ions. *Phys. Rev. Lett.* **74**, 4091–4094 (1995).

[30] C. Monroe, D. M. Meekhof, B. E. King, W. M. Itano, and D. J. Wineland. Demonstration of a fundamental quantum logic gate. *Phys. Rev. Lett.* **75**, 4714–4717 (1995).

[31] F. Schmidt-Kaler, H. Häffner, M. Riebe, S. Gulde, G. P. T. Lancaster, T. Deuschle, C. Becher, C. F. Roos, J. Eschner, and R. Blatt. Realization of the Cirac-Zoller controlled-NOT quantum gate. *Nature* **422**, 408–411 (2003).

[32] S. Gulde, M. Riebe, G. P. T. Lancaster, C. Becher, J. Eschner, H. Häffner, F. Schmidt-Kaler, I. L. Chuang, and R. Blatt. Implementation of the Deutsch-Jozsa algorithm on an ion-trap quantum computer. *Nature* **421**, 48–50 (2003).

[33] M. Riebe, H. Häffner, C. F. Roos, W. Hänsel, J. Benhelm, G. P. T. Lancaster, T. W. Körber, C. Becher, F. Schmidt-Kaler, D. F. V. James, and R. Blatt. Deterministic quantum teleportation with atoms. *Nature* **429**, 734–737 (2004).

[34] M. D. Barrett, J. Chiaverini, T. Schaetz, J. Britton, W. M. Itano, J. D. Jost, E. Knill, C. Langer, D. Leibfried, R. Ozeri, and D. J. Wineland. Deterministic quantum teleportation of atomic qubits. *Nature* **429**, 737–739 (2004).

[35] D. Hanneke, J. P. Home, J. D. Jost, J. M. Amini, D. Leibfried, and D. J. Wineland. Realization of a programmable two-qubit quantum processor. *Nat. Phys.* **6**, 13–16 (2009).

[36] J. P. Home, D. Hanneke, J. D. Jost, J. M. Amini, D. Leibfried, and D. J. Wineland. Complete methods set for scalable ion trap quantum information processing. *Science* **325**, 1227–1230 (2009).

[37] J. Benhelm, G. Kirchmair, C. F. Roos, and R. Blatt. Towards fault-tolerant quantum computing with trapped ions. *Nat. Phys.* **4**, 463–466 (2008).

[38] T. Monz, P. Schindler, J. T. Barreiro, M. Chwalla, D. Nigg, W. A. Coish, M. Harlander, W. Hänsel, M. Hennrich, and R. Blatt. 14-qubit entanglement: Creation and coherence. *Phys. Rev. Lett.* **106**, 130506 (2011).

[39] P. Schindler, J. T. Barreiro, T. Monz, D. Nigg, M. C. M. Hennrich, and R. Blatt. Experimental repetitive quantum error correction. *Science* **332**, 1059–1061 (2011).

[40] K. L. Brown, W. J. Munro, and V. M. Kendon. Using quantum computers for quantum simulation. *Entropy* **12**, 2268–2307 (2010).

[41] R. Jozsa, B. Kraus, A. Miyake, and J. Watrous. Matchgate and space-bounded quantum computations are equivalent. *Proceedings of the Royal Society A: Mathematical, Physical and Engineering Science* **466**, 809–830 (2010).

[42] H. Friedenauer, H. Schmitz, J. Glueckert, D. Porras, and T. Schaetz. Simulating a quantum magnet with trapped ions. *Nat. Phys.* **4**, 757–761 (2008).

[43] K. Kim, M.-S. Chang, S. Korenblit, R. Islam, E. E. Edwards, J. K. Freericks, G.-D. Lin, L.-M. Duan, and C. Monroe. Quantum simulation of frustrated Ising spins with trapped ions. *Nature* **465**, 590–593 (2010).

[44] R. Islam, E. E. Edwards, K. Kim, S. Korenblit, C. Noh, H. Carmichael, G.-D.Lin, L.-M. Duan, C.-C. J. Wang, J. K. Freericks, and C. Monroe. Onset of a quantum phase transition with a trapped ion quantum simulator. *Nature Communications* **2** (2011).

[45] R. Gerritsma, G. Kirchmair, F. Zähringer, E. Solano, R. Blatt, and C. F. Roos. Quantum simulation of the Dirac equation. *Nature* **463**, 68–71 (2010).

[46] J. T. Barreiro, M. Müller, P. S. D. Nigg, T. Monz, M. Chwalla, M. Hennrich, C. F. Roos, P. Zoller, and R. Blatt. An open-system quantum simulator with trapped ions. *Nature* **470**, 486–491 (2011).

[47] B. Lanyon, C. Hempel, D. Nigg, M. Müller, R. Gerritsma, F. Zähringer, P. Schindler, J. T. Barreiro, M. Rambach, G. Kirchmair, M. Hennrich, P. Zoller, R. Blatt, and C. F. Roos. Universal digital quantum simulation with trapped ions. *Science* **334**, 57–61 (2011).

[48] M. A. Nielsen and I. L. Chuang. *Quantum computation and quantum information.* Cambridge Univ. Press, Cambridge, (2000).

[49] R. J. Sension. Biophysics: Quantum path to photosynthesis. *Nature* **446**, 740–741 (2007).

[50] L. Lamata, J. Casanova, R. Gerritsma, C. F. Roos, J. J. García-Ripoll, and E. Solano. Relativistic quantum mechanics with trapped ions. *New Journal of Physics* **13**, 095003 (2011).

[51] J. Audretsch. *Entangled Systems: New Directions in Quantum Physics.* Wiley-VCH Verlag GmbH & Co. KGaA, Weinheim, Germany, (2007).

[52] J. F. Clauser, M. A. Horne, A. Shimony, and R. A. Holt. Proposed experiement to test local hidden-variable theories. *Phys. Rev. Lett.* **23**, 880–884 (1969).

[53] A. Sørensen and K. Mølmer. Entanglement and quantum computation with ions in thermal motion. *Phys. Rev. A* **62**, 022311 (2000).

[54] K. Mølmer and A. Sørensen. Multiparticle entanglement of hot trapped ions. *Phys. Rev. Lett.* **82**, 1835–1838 (1999).

[55] G. Kirchmair, J. Benhelm, F. Zähringer, R. Gerritsma, C. F. Roos, and R. Blatt. Deterministic entanglement of ions in thermal states of motion. *New J. Phys.* **11**, 023002 (2009).

[56] G. Kirchmair, J. Benhelm, F. Zähringer, R. Gerritsma, C. F. Roos, and R. Blatt. High-fidelity entanglement of $^{43}Ca^{+}$ hyperfine clock states. *Phys. Rev. A* **79**, 020304(R) (2009).

[57] F. L. Cohen-Tannoudji, Bernhard Diu. *Quantum mechanics I + II.* Wiley, (1977).

[58] R. Loudon. *The Quantum Theory of Light.* Oxford Univ. Press, (1973).

[59] J. J. Sakurai. *Modern Quantum Mechanics.* Addison-Wesley, revised edition, (1994).

[60] S. Haroche and J.-M. Raimond. *Exploring the quantum.* Oxford Univ. Press, Oxford, (2006).

[61] R. Gerritsma, G. Kirchmair, F. Zähringer, J. Benhelm, R. Blatt, and C. Roos. Precision measurement of the branching fractions of the 4p $^2P_{3/2}$ decay of Ca II. *Eur. Phys. J. D* **50**, 13–19 (2008).

[62] P. A. Barton, C. J. S. Donald, D. M. Lucas, D. A. Stevens, A. M. Steane, and D. N. Stacey. Measurement of the lifetime of the 3d $^2D_{5/2}$ state in $^{40}Ca^{+}$. *Phys. Rev. A* **62**, 032503 (2000).

[63] J. Jin and D. A. Church. Precision lifetimes for the Ca^{+} 4p ^2P levels: Experiment challenges theory at the 1% level. *Phys. Rev. Lett.* **70**, 3213–3216 (1993).

[64] D. F. V. James. Quantum dynamics of cold trapped ions with application to quantum computation. *Appl. Phys. B* **66**, 181–190 (1998).

[65] S. Gulde. *Experimental realization of quantum gates and the Deutsch-Josza algorithm with trapped $^{40}Ca^{+}$–ions.* PhD thesis, Universität Innsbruck, (2003).

[66] C. Roos. *Controlling the quantum state of trapped ions.* PhD thesis, Universität Innsbruck, (2000).

[67] K. E. Cahill and R. J. Glauber. Density operators and quasiprobability distributions. *Phys. Rev.* **177**, 1882–1902 (1969).

[68] D. M. Meekhof, C. Monroe, B. E. King, W. M. Itano, and D. J. Wineland. Generation of nonclassical motional states of a trapped atom. *Phys. Rev. Lett.* **76**, 1796–1799 (1996).

[69] B. E. King, C. S. Wood, C. J. Myatt, Q. A. Turchette, D. Leibfried, W. M. Itano, C. Monroe, and D. J. Wineland. Cooling the collective motion of trapped ions to initialize a quantum register. *Phys. Rev. Lett.* **81**, 1525–1528 (1998).

[70] D. J. Wineland, C. Monroe, W. M. Itano, D. Leibfried, B. E. King, and D. M. Meekhof. Experimental issues in coherent quantum-state manipulation of trapped atomic ions. *J. Res. Natl. Inst. Stand. Technol.* **103**, 259–328 (1998).

[71] H. Häffner, S. Gulde, M. Riebe, G. Lancaster, C. Becher, J. Eschner, F. Schmidt-Kaler, and R. Blatt. Precision measurement and compensation of optical Stark shifts for an ion-trap quantum processor. *Phys. Rev. Lett.* **90**, 143602 (2003).

[72] P. Schindler. *Frequency synthesis and pulse shaping for quantum information processing with trapped ions*. Master's thesis, Universität Innsbruck, (2007).

[73] A. Sørensen and K. Mølmer. Entanglement and quantum computation with ions in thermal motion. *Phys. Rev. A* **62**, 022311 (2000).

[74] S. Wallentowitz and W. Vogel. Reconstruction of the quantum mechanical state of a trapped ion. *Phys. Rev. Lett.* **75**, 2932–2935 (1995).

[75] C. Wunderlich, T. Hannemann, T. Körber, H. Häffner, C. Roos, W. Hänsel, R. Blatt, and F. Schmidt-Kaler. Robust state preparation of a single trapped ion by adiabatic passage. *J. Mod. Opt.* **54**, 1541–1549 (2007).

[76] M. Grant and S. Boyd. CVX: Matlab software for disciplined convex programming. http://stanford.edu/~boyd/cvx, (2009).

[77] J. Benhelm. *Precision spectroscopy and quantum information processsing with trapped calcium ions*. PhD thesis, Universität Innsbruck, (2008).

[78] G. Kirchmair. *Frequency stabilization of a Titanium-Sapphire laser for precision spectroscopy on Calcium ions*. Master's thesis, Universität Innsbruck, (2007).

[79] G. Kirchmair. *Quantum non-demolition measurements and quantum simulation*. PhD thesis, Universität Innsbruck, (2010).

[80] D. J. Berkeland, J. D. Miller, J. C. Bergquist, W. M. Itano, and D. J. Wineland. Minimization of ion micromotion in a paul trap. *J. App. Phys.* **83**, 5025–5033 (1998).

[81] R. W. P. Drever, J. L. Hall, F. V. Kowalski, J. Hough, G. M. Ford, A. J. Munley, and H. Ward. Laser phase and frequency stabilization using an optical resonator. *Appl. Phys. B* **31**, 97–105 (1983).

[82] L. Ma, P. Jungner, J. Ye, and J. L. Hall. Delivering the same optical frequency at two places: accurate cancellation of phase noise introduced by an optical fiber or other time-varying path. *Opt. Lett.* **19**, 1777–1779 (1994).

[83] J. Benhelm, G. Kirchmair, U. Rapol, T. Körber, C. F. Roos, and R. Blatt. Measurement of the hyperfine structure of the $S_{1/2}$-$D_{5/2}$ transition in $^{43}Ca^{+}$. *Phys. Rev. A* **75**, 032506 (2007).

[84] P. T. Pham. MIT-NIST-ARDA pulse sequencer. sourceforge.net/projects/pulse-sequencer, (2005).

[85] A. H. Myerson, D. J. Szwer, S. C. Webster, D. T. C. Allcock, M. J. Curtis, G. Imreh, J. A. Sherman, D. N. Stacey, A. M. Steane, and D. M. Lucas. High-fidelity readout of trapped-ion qubits. *Phys. Rev. Lett.* **100**, 200502 (2008).

[86] A. H. Burrell, D. J. Szwer, S. C. Webster, and D. M. Lucas. Scalable simultaneous multiqubit readout with 99.99% single-shot fidelity. *Phys. Rev. A* **81**, 040302 (2010).

[87] S. Lloyd. Least squares quantization in pcm. *IEEE Transactions on Information Theory* **28**, 129–137 (1982).

[88] T. Monz. *Quantum information processing beyond ten ion-qubits*. PhD thesis, Universität Innsbruck, (2011).

[89] A. Gallagher. Oscillator strengths of Ca II, Sr II, and Ba II. *Phys. Rev.* **157**, 24–30 (1967).

[90] M. J. Seaton and A. K. P. Y. Yan, D. Mihalas. Opacities for stellar envelopes. *Mon. Not. R. Astron. Soc.* **266**, 805–828 (1994).

[91] F. J. Rogers and C. A. Iglesias. Astrophysical opacity. *Science* **263**, 50–55 (1994).

[92] A. L. Wolf, S. A. van den Berg, C. Gohle, E. J. Salumbides, W. Ubachs, and K. S. E. Eikema. Frequency metrology on the 4s $^2S_{1/2}$–4p $^2P_{1/2}$ transition in $^{40}Ca^+$ for a comparison with quasar data. *Phys. Rev. A* **78**, 032511 (2008).

[93] E. Biémont and C. J. Zeippen. Lifetimes of the 3d ^{2}D levels in Ca II. *Comments At. Mol. Phys.* **33**, 29–39 (1996).

[94] S. E. Persson. Calcium infrared triplet emission in active galactic nuclei. *Astrophys. J.* **330**, 751–765 (1988).

[95] C. H. Nelson and M. Whittle. Stellar and gaseous kinematics of Seyfert galaxies. I. Spectroscopic data. *Astrophys. J. Suppl. Ser.* **99**, 67–106 (1995).

[96] D. E. Welty, D. C. Morton, and L. M. Hobbs. A high-resolution survey of interstellar Ca II absorption. *Astrophys. J. Suppl. Ser.* **106**, 533–562 (1996).

[97] R. Ferlet, L. M. Hobbs, and A. Vidal-Madjar. The Beta Pictoris circumstellar disk. 5. Time variation of the Ca II K line. *Astron. Astrophys.* **185**, 267–270 (1987).

[98] L. Hobbs, A. Lagrange-Henri, R. Ferlet, A. Vidal-Madjar, and D. Welty. The location of the Ca-II ions in the beta-pictoris disk. *Astrophys. J.* **334**, L41–L44 (1988).

[99] L. Mashonkina, A. J. Korn, and N. Przybilla. A non-LTE study of neutral and singly-ionized calcium in late-type stars. *Astron. Astrophys.* **461**, 261–275 (2007).

[100] C. Guet and W. R. Johnson. Relativistic many-body calculations of transition rates for Ca^+, Sr^+, and Ba^+. *Phys. Rev. A* **44**, 1531–1535 (1991).

[101] S.-S. Liaw. Ab initio calculation of the lifetimes of 4P and 3D levels of Ca^+. *Phys. Rev. A* **51**, R1723–R1726 (1995).

[102] J. Mitroy and J. Y. Zhang. Long range interactions of the Mg^+ and Ca^+ ions. *Eur. Phys. J. D* **46**, 415–424 (2007).

[103] B. Arora, M. S. Safronova, and C. W. Clark. Blackbody-radiation shift in a $^{43}Ca^+$ ion optical frequency standard. *Phys. Rev. A* **76**, 064501 (2007).

[104] B. K. Sahoo. An ab initio relativistic coupled-cluster theory of dipole and quadrupole polarizabilities: Applications to a few alkali atoms and alkaline earth ions. *Chem. Phys. Lett.* **448**, 144–149 (2007).

[105] N. Fortson. Possibility of measuring parity nonconservation with a single trapped atomic ion. *Phys. Rev. Lett.* **70**, 2383–2386 (1993).

[106] W. W. Smith and A. Gallagher. Radiative lifetime of the first $P_{3/2}$ state of ionized calcium and magnesium by the Hanle effect. *Phys. Rev.* **145**, 26–35 (1966).

[107] R. N. Gosselin, E. H. Pinnington, and W. Ansbacher. Measurement of the lifetimes of the 4p levels in Ca II using laser excitation of a fast beam. *Phys. Rev. A* **38**, 4887–4890 (1988).

[108] A. Kreuter, C. Becher, G. P. T. Lancaster, A. B. Mundt, C. Russo, H. Häffner, C. Roos, W. Hänsel, F. Schmidt-Kaler, R. Blatt, and M. S. Safronova. Experimental and theoretical study of the 3d ^2D–level lifetimes of $^{40}Ca^+$. *Phys. Rev. A* **71**, 032504 (2005).

[109] M. C. E. Huber and R. J. Sandeman. The measurement of oscillator strengths. *Rep. Prog. Phys.* **49**, 397–490 (1986).

[110] S. G. Cox, A. D. J. Critchley, I. R. McNab, and F. E. Smith. High-resolution spectroscopy of ion beams. *Meas. Sci. Technol.* **10**, R101–R128 (1999).

[111] N. Kurz, M. R. Dietrich, G. Shu, R. Bowler, J. Salacka, V. Mirgon, and B. B. Blinov. Measurement of the branching ratio in the $6P_{3/2}$ decay of Ba II with a single trapped ion. *Phys. Rev. A* **77**, 060501 (2008).

[112] B. Efron and R. Tibshirani. Bootstrap methods for standard errors, confidence intervals, and other measures of statistical accuracy. *Stat. Sci.* **1**, 54–75 (1986).

[113] D. L. Moehring, B. B. Blinov, D. W. Gidley, R. N. Kohn, M. J. Madsen, T. D. Sanderson, R. S. Vallery, and C. Monroe. Precision lifetime measurements of a single trapped ion with ultrafast laser pulses. *Phys. Rev. A* **73**, 023413 (2006).

[114] C. F. Roos. Ion trap quantum gates with amplitude-modulated laser beams. *New J. Phys.* **10**, 013002 (2008).

[115] K. Pearson. The problem of the random walk. *Nature* **72**, 294 (1905).

[116] J. S. Rayleigh. The problem of the random walk. *Nature* **72**, 318 (1905).

[117] A. Einstein. Über die von der molekularkinetischen Theorie der Wärme geforderte Bewegung von in ruhenden Flüssigkeiten suspendierten Teilchen. *Annalen der Physik* **220**, 549–560 (1905).

[118] H. C. Berg. *Random Walks in Biology.* Princeton Univ. Press, Princeton, NJ, revised ed., (1993).

[119] M. Barber. *Random and Restricted Walks: Theory and Applications.* Routledge, first edition, (1970).

[120] E. Fama. Random walks in stock market prices. *Financ. Anal. J.* **21**, 55–59 (1995).

[121] Y. Aharonov, L. Davidovich, and N. Zagury. Quantum random walks. *Phys. Rev. A* **48**, 1687–1690 (1993).

[122] J. Kempe. Quantum random walks: an introductory overview. *Cont. Phys.* **44**, 307–327 (2003).

[123] A. M. Childs. Universal computation by quantum walk. *Phys. Rev. Lett.* **102**, 180501 (2009).

[124] W. Dür, R. Raussendorf, V. M. Kendon, and H.-J. Briegel. Quantum walks in optical lattices. *Phys. Rev. A* **66**, 052319 (2002).

[125] B. C. Travaglione and G. J. Milburn. Implementing the quantum random walk. *Phys Rev A* **65**, 032310 (2002).

[126] B. C. Sanders, S. D. Bartlett, B. Tregenna, and P. L. Knight. Quantum quincunx in cavity quantum electrodynamics. *Phys. Rev. A* **67**, 042305 (2003).

[127] M. Karski, L. Förster, J.-M. Choi, A. Steffen, W. Alt, D. Meschede, and A. Widera. Quantum walk in position space with single optically trapped atoms. *Science* **325**, 174–177 (2009).

[128] H. Schmitz, R. Matjeschk, C. Schneider, J. Glueckert, M. Enderlein, T. Huber, and T. Schaetz. Quantum walk of a trapped ion in phase space. *Phys. Rev. Lett.* **103**, 090504 (2009).

[129] A. Schreiber, K. N. Cassemiro, V. Potocek, A. Gabris, P. Mosley, E. Andersson, I. Jex, and C. Silberhorn. Photons walking the line: A quantum walk with adjustable coin operations. *Phys. Rev. Lett.* **104**, 0505021 (2009).

[130] F. Zähringer, G. Kirchmair, R. Gerritsma, E. Solano, R. Blatt, and C. F. Roos. Realization of a quantum walk with one and two trapped ions. *Phys. Rev. Lett.* **104**, 100503 (2010).

[131] B. Tregenna, W. Flanagan, R. Maile, and V. Kendon. Controlling discrete quantum walks: coins and initial states. *New J. Phys.* **5**, 83.1–83.19 (2003).

[132] P. Xue, B. C. Sanders, and D. Leibfried. Quantum walk on a line for a trapped ion. *Phys. Rev. Lett.* **103**, 183602 (2009).

[133] A. Schreiber, A. Gábris, P. P. Rohde, K. Laiho, M. Štefaňák, V. Potoček, C. Hamilton, I. Jex, and C. Silberhorn. A 2d quantum walk simulation of two-particle dynamics. *Science* **336**, 55–58 (2012).

[134] V. Kendon and B. Tregenna. Decoherence can be useful in quantum walks. *Phys. Rev. A* **67**, 042315 (2003).

[135] M. Gönülol, E. Aydıner, Y. Shikano, and Özgür E Müstecaplıoğlu. Survival probability in a one-dimensional quantum walk on a trapped lattice. *New Journal of Physics* **13**, 033037 (2011).

[136] M. A. Broome, A. Fedrizzi, B. P. Lanyon, I. Kassal, A. Aspuru-Guzik, and A. G. White. Discrete single-photon quantum walks with tunable decoherence. *Phys. Rev. Lett.* **104**, 153602 (2010).

[137] F. Mintert and C. Wunderlich. Ion-trap quantum logic using long-wavelength radiation. *Phys. Rev. Lett.* **87**, 257904 (2001).

[138] R. G. B. Lanyon, G. Kirchmair, F. Zähringer, C. Hempel, J. Casanova, J. García-Ripoll, E. Solano, R. Blatt, and C. F. Roos. Quantum simulation of the Klein Paradox with trapped ions. *Phys. Rev. Lett.* **106**, 060503 (2011).

[139] C. D. Anderson. The positive electron. *Phys. Rev.* **43**, 491–494 (1933).

[140] L. Lamata, J. León, T. Schätz, and E. Solano. Dirac equation and quantum relativistic effects in a single trapped ion. *Phys. Rev. Lett.* **98**, 253005 (2007).

[141] L. J. Garay, J. R. Anglin, J. I. Cirac, and P. Zoller. Sonic analog of gravitational black holes in Bose-Einstein condensates. *Phys. Rev. Lett.* **85**, 4643–4647 (2000).

[142] J. Schliemann, D. Loss, and R. M. Westervelt. Zitterbewegung of electronic wave packets in III-V zinc-blende semiconductor quantum wells. *Phys. Rev. Lett.* **94**, 206801 (2005).

[143] A. Bermudez, M. A. Martin-Delgado, and E. Solano. Exact mapping of the 2+1 Dirac oscillator onto the Jaynes-Cummings model: ion-trap experimental proposal. *Phys. Rev. A* **76**, 041801(R) (2007).

[144] X. Zhang. Observing *Zitterbewegung* for photons near the Dirac point of a two-dimensional photonic crystal. *Phys. Rev. Lett.* **100**, 113903 (2008).

[145] J. Y. Vaishnav and C. W. Clark. Observing *Zitterbewegung* with ultracold atoms. *Phys. Rev. Lett.* **100**, 153002 (2008).

[146] J. Otterbach, R. G. Unanyan, and M. Fleischhauer. Confining stationary light: Dirac dynamics and Klein tunneling. *Phys. Rev. Lett.* **102**, 063602 (2009).

[147] F. Dreisow, M. Heinrich, R. Keil, A. Tünnermann, S. Nolte, S. Longhi, and A. Szameit. Classical simulation of relativistic *Zitterbewegung* in photonic lattices. *Phys. Rev. Lett.* **105**, 143902 (2010).

[148] B. Thaller. Visualizing the kinematics of relativistic wave packets. *arXiv:quant-ph/0409079* (2004).

[149] E. Schrödinger. Über die kräftefreie Bewegung in der relativistischen Quantenmechanik. *Sitz. Preuss. Akad. Wiss. Phys.-Math. Kl.* **24**, 418–428 (1930).

[150] O. Klein. Die Reflexion von Elektronen an einem Potentialsprung nach der relativistischen Dynamik von Dirac. *Z. Phys.* **53**, 157–165 (1929).

[151] F. Sauter. Über das Verhalten eines Elektrons im homogenen elektrischen Feld nach der relativistischen Theorie Diracs. *Z. Phys.* **69**, 742–764 (1931).

[152] H. Galic. Fun and frustration with hydrogen in a 1+1 dimension. *Am. J. of Phys.* **56**, 312 (1988).

[153] R. Giachetti and E. Sorace. States of the Dirac equation in confining potentials. *Phys. Rev. Lett.* **101**, 190401 (2008).

[154] M. I. Katsnelson, K. S. Novoselov, and A. K. Geim. Chiral tunnelling and the Klein paradox in graphene. *Nat. Phys.* **2**, 620–625 (2006).

[155] A. H. C. Neto, F. Guinea, N. M. R. Peres, K. S. Novoselov, and A. K. Geim. The electronic properties of graphene. *Rev. Mod. Phys.* **81**, 109–162 (2009).

[156] A. F. Young and P. Kim. Quantum interference and Klein tunneling in graphene heterojunctions. *Nat. Phys.* **5**, 222–226 (2009).

[157] F. Hund. Materieerzeugung im anschaulichen und im gequantelten Wellenbild der Materie. *Z. Phys.* **117**, 1–17 (1941).

[158] J. Schwinger. On gauge invariance and vacuum polarization. *Phys. Rev.* **82**, 664–679 (1951).

[159] J. Casanova, J. J. Garcia-Ripoll, R. Gerritsma, C. F. Roos, and E. Solano. Klein tunneling and dirac potentials in trapped ions. *Phys. Rev. A* **82**, 020101(R) (2010).

[160] C. Wittig. The Landau-Zener formula. *J. Phys. Chem. B* **109**, 8428–8430 (2005).

[161] F. Toscano, D. A. R. Dalvit, L. Davidovich, and W. H. Zurek. Sub-Planck phase-space structures and Heisenberg-limited measurements. *Phys. Rev. A* **73**, 023803 (2006).

[162] J. Casanova, C. Sabin, J. Leon, I. L. Egusquiza, R. Gerritsma, C. F. Roos, J. J. Garcia-Ripoll, and E. Solano. Quantum simulation of the Majorana equation and unphysical operations. *Phys. Rev. X* **1**, 021018 (2011).

[163] J. Casanova, L. Lamata, I. L. Egusquiza, R. Gerritsma, C. F. Roos, J. J. Garcia-Ripoll, and E. Solano. Quantum simulation of quantum field theories in trapped ions. *Phys. Rev. Lett.* **107**, 260501 (2011).

[164] M. Johanning, A. F. Varón, and C. Wunderlich. Quantum simulations with cold trapped ions. *J. Phys. B* **42**, 154009 (2009).

[165] D. Porras and J. I. Cirac. Effective quantum spin systems with trapped ions. *Phys. Rev. Lett.* **92**, 207901 (2004).

[166] D. Porras, F. Marquardt, J. von Delft, and J. I. Cirac. Mesoscopic spin-boson models of trapped ions. *Phys. Rev. A* **78**, 010101 (2008).

[167] N. C. Menicucci and G. J. Milburn. Single trapped ion as a time-dependent harmonic oscillator. *Phys. Rev. A* **76**, 052105 (2007).

[168] P. M. Alsing, J. P. Dowling, and G. J. Milburn. Ion trap simulations of quantum fields in an expanding universe. *Phys. Rev. Lett.* **94**, 220401 (2005).

[169] R. Schützhold, M. Uhlmann, L. Petersen, H. Schmitz, A. Friedenauer, and T. Schätz. Analogue of cosmological particle creation in an ion trap. *Phys. Rev. Lett.* **99**, 201301 (2007).

[170] I. García-Mata, O. V. Zhirov, and D. L. Shepelyansky. Frenkel-Kontorova model with cold trapped ions. *Eur. Phys. J. D* **41**, 325–330 (2007).

[171] D. Kielpinski, C. Monroe, and D. J. Wineland. Architecture for a large-scale ion-trap quantum computer. *Nature* **417**, 709–711 (2002).

[172] W. K. Hensinger, S. Olmschenk, D. Stick, D. Hucul, M. Yeo, M. Acton, L. Deslauriers, and C. Monroe. T-junction ion trap array for two-dimensional ion shuttling storage, and manipulation. *Appl. Phys. Lett.* **88**, 034101 (2006).

[173] F. Splatt, M. Harlander, M. Brownnutt, F. Zähringer, R. Blatt, and W. Hänsel. Deterministic reordering of $^{40}Ca^{+}$ ions in a linear segmented Paul trap. *New J. Phys.* **11**, 103008 (2009).

[174] G.-D. Lin, S.-L. Zhu, R. Islam, K. Kim, M.-S. Chang, S. Korenblit, C. Monroe, and L.-M. Duan. Large-scale quantum computation in an anharmonic linear ion trap. *Europhys. Lett.* **86**, 60004 (2009).

[175] K. R. Brown, C. Ospelkaus, Y. Colombe, A. C. Wilson, D. Leibfried, and D. J. Wineland. Coupled quantized mechanical oscillators. *Nature* **471**, 196–199 (2011).

[176] M. Harlander, R. Lechner, M. Brownnutt, R. Blatt, and W. Hänsel. Trapped-ion antennae for the transmission of quantum information. *Nature* **471**, 200 – 203 (2011).

[177] H. J. Kimble. The quantum internet. *Nature* **453**, 1023–1030 (2008).

[178] L.-M. Duan and C. Monroe. *Colloquium* : Quantum networks with trapped ions. *Rev. Mod. Phys.* **82**, 1209–1224 (2010).

[179] L. Deslauriers, S. Olmschenk, D. Stick, W. K. Hensinger, J. Sterk, and C. Monroe. Scaling and suppression of anomalous heating in ion traps. *Phys. Rev. Lett.* **97**, 103007 (2006).

[180] K. Okada, M. Wada, L. Boesten, T. Nakamura, I. Katayama, and S. Ohtani. Acceleration of the chemical reaction of trapped Ca^+ ions with H_2O molecules by laser excitation. *J. Phys. B: At. Mol. Opt. Phys.* **36**, 33–46 (2003).

[181] D. Enzer, M. Schauer, J. Gomez, M. Gulley, M. Holzscheiter, P. Kwiat, S. Lamoreaux, C. Peterson, V. Sandberg, D. Tupa, A. White, and R. Hughes. Observation of power-law scaling for phase transitions in linear trapped ion crystals. *Phys. Rev. Lett.* **85**, 2466–2469 (2000).

[182] M. Chwalla. *Precision spectroscopy with $^{40}Ca^+$ ions in a Paul trap.* PhD thesis, Institute for Experimental Physics, Innsbruck, (2009).

[183] M. Chwalla, J. Benhelm, K. Kim, G. Kirchmair, T. Monz, M. Riebe, P. Schindler, A. S. Villar, W. Hänsel, C. F. Roos, R. Blatt, M. Abgrall, G. Santarelli, G. D. Rovera, and P. Laurent. Absolute frequency measurement of the $^{40}Ca^+$ 4s $S_{1/2}$-3d $D_{5/2}$ clock transition. *Phys. Rev. Lett.* **102**, 023002 (2009).

[184] F. Kurth, T. Gudjons, B. Hilbert, T. Reisinger, G. Werth, and A. M. Martensson-Pendrill. Dopper free "dark resonances" for hyperfine measurements and isotope shifts in Ca^+ isotopes in a Paul trap. *Z. Phys. D* **34**, 227–232 (1995).

[185] W. Nörtershauser, K. Blaum, K. Icker, P. Muller, A. Schmitt, K. Wendt, and B. Wiche. Isotope shifts and hyperfine structure in the 3d ^2D_j– 4p ^2P_j transitions in calcium II. *Eur. Phys. J. D* , 33–39 (1998).

[186] G. Tommaseo, T. Pfeil, G. Revalde, G. Werth, P. Indelicato, and J. Desclaux. The g_J-factor in the ground state of Ca^+. *Eur. Phys. J. D* **25**, 113–121 (2003).

Danksagung

Eine Doktorarbeit in Experimentalphysik ohne die Unterstützung von zahlreichen Seiten ist heutzutage praktisch unmöglich und die vorliegende Arbeit bildet hierbei keine Ausnahme. All jenen, die zum Entstehen der vorliegenden Arbeit beigetragen haben, möchte ich hiermit herzlich danken.

An erster Stelle möchte ich mich bei Rainer Blatt bedanken, der mir nach der Diplomarbeit auch die Doktorarbeit in seiner Arbeitsgruppe ermöglicht hat. Bei einem spannenden Forschungsthema „ganz vorne mit dabei" sein zu können, hat mir viel Freude bereitet und mich stets motiviert.

Auch gilt mein Dank Christian Roos, auf den ein Großteil der Konzeption der hier vorgestellten Experimente zurückgeht.

Im Labor habe ich viel von Gerhard Kirchmair und Rene Gerritsma lernen können. Bei beiden möchte ich mich für die interessante und erfolgreiche Zeit bedanken. Wir waren einfach ein gutes Team!

Des weiteren möchte ich mich bei Cornelius Hempel und Benjamin Lanyon bedanken. Ebenso bei Markus Rambach, der so oft eine helfende Hand für mich hatte.

Unzählig, und daher fast unmöglich aufzulisten, sind die vielen kleinen Unterstützungen und hilfreichen Gespräche innerhalb der Arbeitsgruppe. Dafür möchte ich mich herzlich bei allen bedanken. Im Speziellen bei den Mitgliedern der Kochgruppe, die so viele Jahre für eine gute Verpflegung und interessante Unterhaltungen gesorgt haben.

Ebenso gilt mein Dank auch den nicht-wissenschaftlichen Mitarbeitern in den Werkstätten und Sekretariaten. Im Besonderen Stefan Haslwanter, der nicht nur maßgeblich an der Konstruktion der neuen Falle beteiligt, sondern auch beim Aufbau der neuen Vakuumkammer eine große Hilfe war.

Auch möchte ich mich bei all jenen bedanken, die außerhalb des Labors, sei es in den Bergen, in der Halle oder in der WG, für die nötige Erholung und Ablenkung gesorgt haben.

Ein ganz besonderer Dank gebührt meinen Eltern, die mich all die Jahre während meines Studiums und der Doktorarbeit unterstützt haben.

Selbstverständlich ist der letzte Absatz meiner Danksagung einem für mich besonders wichtigen Menschen gewidmet: Meiner Freundin Regina möchte ich von ganzem Herzen danken, dass sie in den letzten Jahren die vielen Facetten eines Doktorandenlebens mit mir geteilt hat.